Controlling the Surface Band Gap in Topological States of Matter

Partha Sarathi Mandal

Dissertation

**zur Erlangung des akademischen Grades
"doctor rerum naturalium"
(Dr. rer. nat.)
in der Wissenschaftsdisziplin
Physik kondensierter Materie**

**eingereicht an der
Mathematisch-Naturwissenschaftlichen Fakultät
Institut für Physik und Astronomie
der Universität Potsdam
und
Helmholtz Zentrum Berlin**

Potsdam, 29.10.2020

Hauptbetreuer: apl. Prof. Dr. Oliver Rader
Gutachter: Prof. Dr. Hans-Joachim Elmers
                   Prof. Dr. Martin Weinelt

Contents

To my parents who taught me the value of education

Abstract

In the present study, we employ the angle-resolved photoemission spectroscopy (ARPES) technique to study the electronic structure of topological states of matter. In particular, the so-called topological crystalline insulators (TCIs) $Pb_{1-x}Sn_xSe$ and $Pb_{1-x}Sn_xTe$, and the Mn-doped $\mathbb{Z}_2$ topological insulators (TIs) Bi_2Te_3 and Bi_2Se_3. The $\mathbb{Z}_2$ class of strong topological insulators is protected by time-reversal symmetry and is characterized by an odd number of metallic Dirac type surface states in the surface Brillouin zone. The topological crystalline insulators on the other hand are protected by the individual crystal symmetries and exhibit an even number of Dirac cones.

The topological properties of the lead tin chalcogenides topological crystalline insulators can be tuned by temperature and composition. Here, we demonstrate that Bi-doping of the $Pb_{1-x}Sn_xSe(111)$ epilayers induces a quantum phase transition from a topological crystalline insulator to a $\mathbb{Z}_2$ topological insulator. This occurs because Bi-doping lifts the fourfold valley degeneracy in the bulk. As a consequence a gap appears at $\overline{\Gamma}$, while the three Dirac cones at the $\overline{M}$ points of the surface Brillouin zone remain intact. We interpret this new phase transition is caused by lattice distortion. Our findings extend the topological phase diagram enormously and make strong topological insulators switchable by distortions or electric field. In contrast, the bulk Bi doping of epitaxial $Pb_{1-x}Sn_xTe(111)$ films induces a giant Rashba splitting at the surface that can be tuned by the doping level. Tight binding calculations identify their origin as Fermi level pinning by trap states at the surface.

Magnetically doped topological insulators enable the quantum anomalous Hall effect (QAHE) which provide quantized edge states for lossless charge transport applications. The edge states are hosted by a magnetic energy gap at the Dirac point which has not been experimentally observed to date. Our low temperature ARPES studies unambiguously reveal the magnetic gap of Mn-doped Bi_2Te_3. Our analysis shows a five times larger gap size below the T_c than theoretically predicted. We assign this enhancement to a remarkable structure modification induced by Mn doping. Instead of a disordered impurity system, a self-organized alternating sequence of $MnBi_2Te_4$ septuple and Bi_2Te_3 quintuple layers is formed. This enhances the wave-function overlap and gives rise to a large magnetic gap. Mn-doped Bi_2Se_3 forms similar heterostructure, but only a nonmagnetic gap is observed in this system. This

correlates with the difference in magnetic anisotropy due to the much larger spin-orbit interaction in Bi_2Te_3 compared to Bi_2Se_3. These findings provide crucial insights for pushing lossless transport in topological insulators towards room-temperature applications.

Chapter 1

Motivation

"If you shut the door to all errors, truth will be shut out."

— Rabindranath Tagore; Nobel laureate in Literature (1913)

The topological classification of materials is one of the most critical developments in condensed-matter physics in the last decades. Recently a new type of topological phase termed topological crystalline insulator (TCI) has been theoretically predicted and experimentally observed in three dimensional materials such as SnTe, $Pb_{1-x}Sn_xSe$, and $Pb_{1-x}Sn_xTe$ class of narrow gap IV-VI semiconductors. These newly discovered TCIs have a complex surface band structure involving an even number of Dirac cones in contrast to the established $\mathbb{Z}_2$ topological insulators. In TCIs, the metallic surface states are protected by point group symmetry of the crystalline lattice rather than time reversal symmetry. In comparison to $\mathbb{Z}_2$ topological insulators, TCIs feature enhanced tunability of topological surface states (TSSs) by external perturbations such as temperature, composition, strain as well as electric and magnetic fields. Opening a gap in the surface state can be used for a wide range of technological applications and is of fundamental interest in condensed matter physics. In the majority of previous works, bulk TCI crystals cleaved along the (001) natural cleavage planes of the lead tin chalcogenides were studied, while TSSs of other planes such as (110) or (111) have remained relatively unexplored. Due to the polar nature of (111) plane, one would expect different properties of the TSSs in comparison to the non-polar (001) plane which contains both cations and anions. We concentrate on the (111) surface where the surface state at $\overline{\Gamma}$ is additionally protected by time-reversal symmetry. The temperature is well known to tune the lattice constant and drive the bulk band inversion in a simple way.

Chapter 4 of this thesis focuses on temperature and Sn concentration dependence of the TCI phase transition in $Pb_{1-x}Sn_xSe$. The $Pb_{1-x}Sn_xSe$ epilayers were grown by molecular beam epitaxy and studied using angle resolved photoemission spectroscopy (ARPES). Interestingly, the $Pb_{1-x}Sn_xSe$ samples doped with 1–2% of Bi shows a gapped surface state at the $\overline{\Gamma}$ in the TCI phase. We demonstrate that Bi-doping in this system induces a quantum phase

transition from a topological crystalline insulator to a $\mathbb{Z}_2$ topological insulator. This occurs because Bi-doping lifts the fourfold valley degeneracy and induces a gap at $\overline{\Gamma}$, while the three Dirac cones at the $\overline{M}$ points of the surface Brillouin zone remain intact. Our interpretation of this new phase transition is due to rhombohedral lattice distortion. These findings extend the topological phase diagram enormously, and the potential applications could arise through ferroelectric phases - ones that have not been thought of before in this system. Lossless conduction of electricity in topological materials can be switched on and off at will, by electrical pulses or by mechanical strain.

In chapter 5, we have systematically studied the (111) TSSs of $Pb_{1-x}Sn_xTe$:Bi epilayers grown by molecular beam epitaxy and using temperature dependent ARPES measurements with different Sn concentration. The high intrinsic p-type carrier concentration due to Pb/Sn vacancies in $Pb_{1-x}Sn_xTe$ were compensated by Bi doping that allowed us to obtain n-type samples and thus, to observe the conduction and the valence bands. We find a gap closing for Sn concentration larger than 40% at low temperature. Moreover, a giant Rashba splitting was observed for the valence band while conduction band did not show such behavior. In particular, we found that the Rashba splitting increases with increasing Bi concentration, and it was absent for undoped epilayers. The value of k_R-splitting and Rashba parameter for the samples doped with Bi were as large as $k_R = 0.017 Å^{-1}$ and $\alpha_R = 3.5$ eVÅ, comparable to the values reported for other giant Rashba split systems.

Bismuth Telluride (Bi_2Te_3) is a prototypical example for a three-dimensional (3D) $\mathbb{Z}_2$ topological insulator with a gapped bulk band structure and a two-dimensional (2D) topological surface state with Dirac-like energy-momentum dispersion and spin-momentum locking. The surface state is protected by time-reversal symmetry and is immune to surface impurities and backscattering. When 3d transition metals such as Mn, Fe, Cr or V are incorporated as magnetic dopants, their local exchange fields can break time reversal symmetry and thus may lift the degeneracy of the Dirac points with a gap opening of the topological surface state. This is the main topic of chapter 6.

Band gap opening in the surface state of $\mathbb{Z}_2$ topological insulator by breaking time reversal symmetry in the presence of magnetic moment has a long standing controversy in the community. There is no concrete experimental evidence of the opening a surface gap by magnetic moment or ferromagnetism via breaking of time-reversal symmetry so far. Recent studies have shown two very distinct electronic properties depending on the doping of the magnetic material on the surface or in the bulk of the topological Insulators. The deposition of the ferromagnetic material in the surface produces an important change of the surface chemistry in the near surface region, while the bulk doping results in a homogeneous bulk phase corresponds to a conventional diluted magnetic semiconductor. Whereas, in the other study shows the Mn atoms are incorporated predominantly as interstitial in the van

der Waals gap between the quintuple layers, showing the ferromagnetic nature, although the ARPES study does not show any signs of the gap opening. We have found that there exists a gapped surface state for Mn doped Bi_2Te_3 when cooled down below Curie temperature. The shift of the Dirac point on the energy distribution curve (EDC) towards lower kinetic energy from room temperature to low temperature could be the signature of the temperature effect in this semi-metal like system. Comparing the data of above and below T_c, we noticed a redistribution of spectral weight at the low temperature measurement which creates a small plateau at the Dirac point signifies the gap opening of the topological surface state.

Chapter 2

Topological Phases of Matter

"Not only is the Universe stranger than we think, it is stranger than we can think."

— Werner Heisenberg; Nobel laureate in Physics (1932)

Werner Heisenberg could not be more exact in the present context of condensed matter physics. In the advent of quantum physics in 1920, physics' world has seen some extraordinary discoveries. Distinguishing between the different phases of matter is one of them. In the early 20s, band structure theory of solids could explain the difference between a conductor and an insulator. However, in the last 30 years, the difference reappeared as a surprise in the form of the quantum Hall effect. As this goes, in 2016, the Noble Prize in Physics was awarded for "theoretical discoveries of topological phase transitions and topological phases of matter." The Nobel Prize press release states that the discovery has opened an unknown world where matter can assume strange states [1]. The discovery of the topological phases is not just crucial for fundamental understanding of solid state physics, but it has the potential to revolutionize the technological world in terms of dissipationless current and realization of a quantum computer with 100% accuracy. In this chapter, we will describe few fundamental concepts which underline the new states of matter called *topological states of matter* and discuss the implications in the context of the present thesis through the following questions:

- **What are topological phases of matter?**

- **Why is it interesting?**

- **How does it work?**

- **Which materials are topological?**

2.1   Distinction of Topological Phases of Matter

We will start by describing a little bit of what we know about the electronic states of matter at a basic level. A free-electron has an energy which is given by $\hbar^2 k^2/2m$. Hence, the dispersion relation, energy as a function of wave vector or momentum has a parabolic shape as shown in figure 2.1(a). Now if we take this electron and put it in a crystal lattice with periodic potential, it has to be described by the wave vector using the Bloch wave function [2]. The solution of the Schrödinger equation in a periodic potential must be of a special form

$$\psi_k(\vec{r}) = u_k(\vec{r}) \exp(i\vec{k}.\vec{r}) \tag{2.1}$$

where $u_k(\vec{r})$ has the period of the crystal lattice with $u_k(\vec{r}) = u_k(\vec{r} + \vec{T})$. Due to Bragg scattering at the edge of the Brillouin zone, an energy gap opens up as shown in figure 2.1(b). This gap opening already allows us to describe two different phases or two different electronic states of matter: metal, and insulator. As we know, two electrons (spin up and spin down) are needed to fill an energy band completely. If we consider for instance one electron per atom that only half fills the lower band as in Fig. 2.1(b), this corresponds to metal. If we have two electrons per atom, we get an insulator. More precisely we get something that has a full band and an energy gap for excitation. If we apply an electric field in a metal, we can adiabatically move the right going states to higher momenta and left going states to the lower momenta. This creates a net current in the system taking into account the group velocity of the right going states and of the left going state. In the case of an insulator, we have the full band, and applying an electric field does not create any net current, and the system does not conduct electricity. This is the difference between a metal and an insulator.
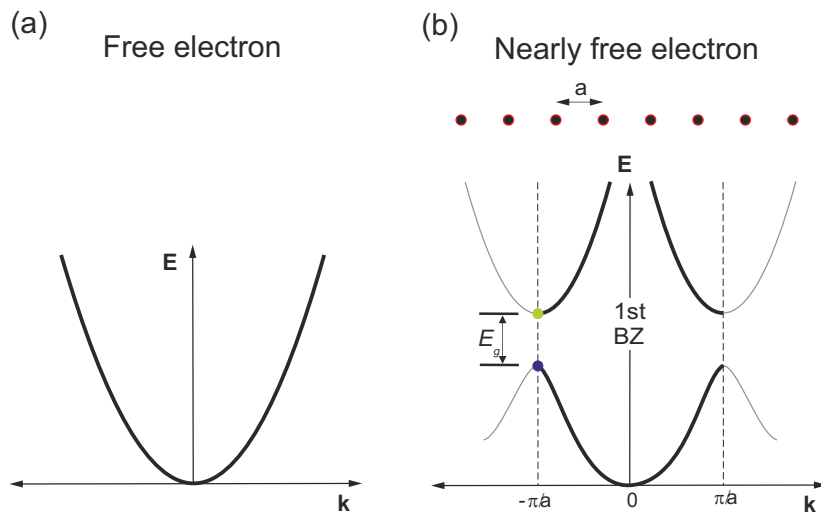

Figure 2.1: *(a) Free electron model, dispersion relation is parabolic. (b) Electron in periodic potential described by Bloch wave function. Energy gap (E_g) appears at the edge of the Brillouin zone due to Bragg scattering.*

2.2 Integer Quantum Hall State

Now, let's take a look at a slightly different system. Let's take the free electron in two dimensions and put it in a magnetic field perpendicular to the surface. So classically what happens to an electron in a strong magnetic field is that it would orbit in cyclotron orbits. However, the quantum mechanical version is even more interesting. We can easily derive the energy eigenvalues as following. We start with the Schrodinger equation for a free electron, and then add a vector potential, and in a few steps, we can come up with a solution presented in Eq. 2.6. The solutions are harmonic oscillators, and they are localized in space. They have the ladder of energies where the frequency is described by the cyclotron frequency [3]. The energy levels are called *Landau levels*, which determines the electrons now appear only in discrete energies, shown in figure 2.2(c,d). The dispersion relation is totally modified in this scenario. The energy levels are fully degenerate levels where all the electrons sit and nothing in the energy between them. These Landau levels are effectively localized, and they have no group velocity.

$$\left[\frac{(p + eA)^2}{2m} \right] \bar{\Psi} = E\bar{\Psi} \tag{2.2}$$

Considering Landau gauge: $\hat{A} = B_y \hat{x}$

$$\left[\frac{(p_x + eB_y)^2}{2m} + \frac{p_y^2}{2m} \right] \bar{\Psi} = E\bar{\Psi} \tag{2.3}$$

$$\bar{\Psi} = e^{ik_x x} \chi(y) \tag{2.4}$$

$$\left[\frac{p_y^2}{2m} - \frac{1}{2} m\omega_c^2 (y + y_k)^2 \right] \chi(y) = E\chi(y) \tag{2.5}$$

$$E = (n + \frac{1}{2})\hbar\omega_c \tag{2.6}$$

The question that one might immediately ask is whether this 2D electron system with filled Landau levels is an insulator. It certainly looks like an insulator, if we take the Fermi energy and put it in between the Landau levels, then it is inside of an energy gap (Fig. 2.2(d)). The Fermi level lies between a filled band and an empty band, and there is an excitation gap. So it looks like something that should not conduct, but we can do the experiment, which was first done in the 1980s [5]. It requires a very clean two-dimensional electron system with high mobility for various reasons. The gap has to be well-defined, and another condition is that the mobility times the magnetic field has to be large. The corresponding measurement results at low temperatures (T << 10 K) and in high magnetic fields (B > 10 T) have been shown in Figure 2.2(a), and (b). The longitudinal magnetoresistance of the sample starts
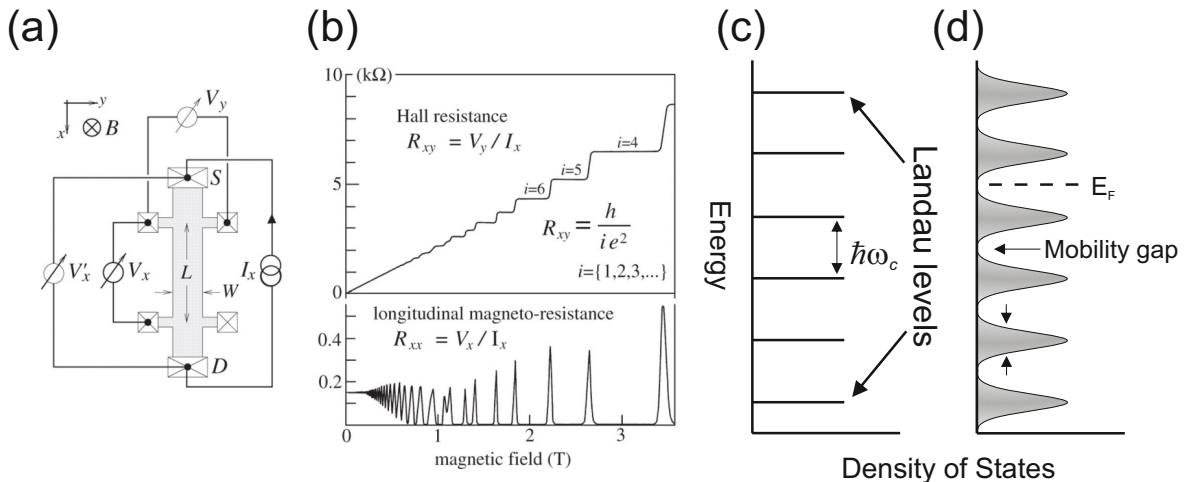
Figure 2.2: Integer Quantum Hall Effect *(a) The Hall bar geometry and the respective electrical set-up. (b) Hall resistance curve and longitudinal magneto-resistance curve measured on a two-dimensional electron system.(adapted from ref. [4] © 2011, The Royal Society (U.K.)) (c),(d) Landau quantization of the density of states and subsequent broadening in real systems respectively.*

with finite value as a function of magnetic field, and then it begins to oscillate. As we increase the magnetic field strength, the Landau levels continue moving through the Fermi energy, and at some point the longitudinal magnetoresistance goes to zero with some oscillations in between. On the other hand, the Hall resistance increases and forms plateaus where it is quantized over some range of magnetic field. The important point here is that the longitudinal magnetoresistance (R_{xx}) does not become infinite; in fact, it becomes zero, which is rather odd. It is still the same system even in this state where we have the well-defined Landau levels conduct. The corresponding Hall resistivity ρ_{xy} and conductivity σ_{xy} tensor is given by the equation 2.7.

$$\rho_{xy} = \begin{pmatrix} 0 & \frac{h}{\nu e^2} \\ -\frac{h}{\nu e^2} & 0 \end{pmatrix} ; \sigma_{xy} = \begin{pmatrix} 0 & -\frac{\nu e^2}{h} \\ \frac{\nu e^2}{h} & 0 \end{pmatrix} \tag{2.7}$$

The diagonal resistivity is reflected zero, but the diagonal conductivity is also zero. This observation shows an insulating behavior, however it is a nontrivial insulator. It has the off-diagonal conductivity known as the *Hall conductivity* which is quantized [5]. The quantization given by e^2/h, is incredibly exact to about a part in a billion which was one of the reasons why this quantum Hall effect (QHE) was awarded with the Nobel Prize in 1985 to Klaus von Klitzing. The quantum Hall (QH) phase is an insulating phase in the sense that it has zero conductivity. It has an energy gap between the two excitations, but it differs from the trivial band insulator which was described earlier with a full band picture in the nearly free electron model. Figure 2.3 shows the difference between these two states. The ordinary insulating

state is characterized by an energy gap separating the occupied and empty electronic states which are known as valence band and conduction band respectively. In the QH effect, the circular motion of electrons in a magnetic field, **B**, is interrupted by the sample boundary. At the edge, electrons execute "skipping orbits" as shown in Figure 2.3(b), ultimately leading to perfect conduction in one direction along the edge [6].
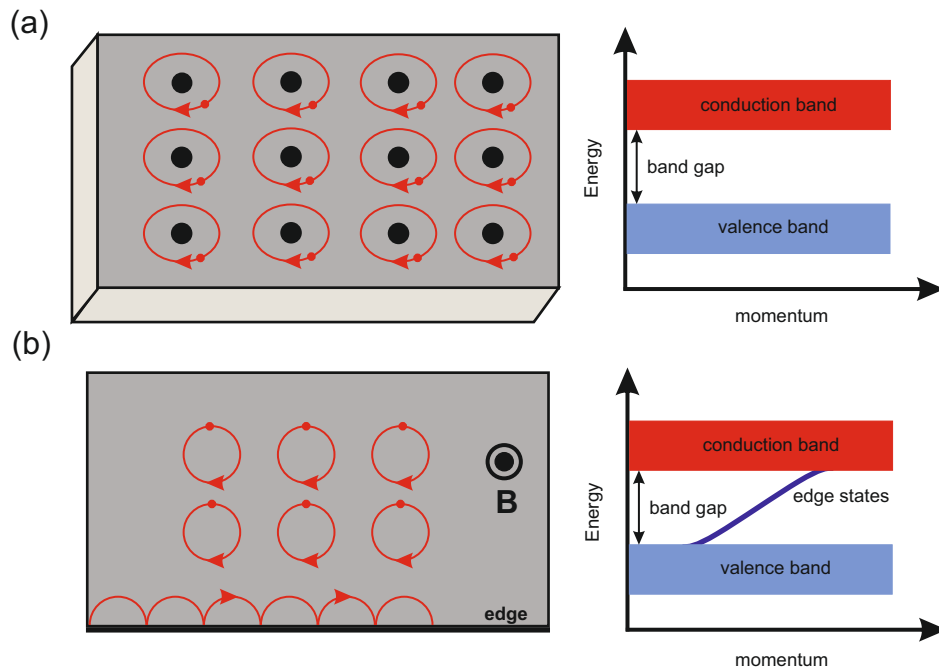
Figure 2.3: Insulator with a twist: *(a) The ordinary insulating state is characterized by an energy gap separating the occupied and empty electronic states. **(b)** In the quantum Hall effect, the circular motion of electrons in a magnetic field leads to perfect conduction along the edge of the sample. Adapted from ref. [7].*

To understand this we can start to think whether this is a transition to a different phase of matter. Phase transitions have been understood within the Landau picture of establishing an order parameter by spontaneous symmetry breaking. For instance, a ferromagnet breaks rotational symmetry by establishing a particular magnetization direction, which is an order parameter and a broken symmetry. Symmetry breaking explains several phase transitions, for instance, liquid to solid or magnetism, and superconductivity. In the case of the QH phase, in one hand no symmetry is apparently broken and on the other hand we have the quantized Hall resistance with incredibly precise quantization value. So there is something very special about these phases, and the possible explanation comes from topology. So to understand it, we will first look at what topology is. Topology is a branch of mathematics focusing on fundamental properties of objects that are preserved under continuous deformation. Topological properties do not change when an object is gradually stretched or bent, it has instead to be torn or attached to new places. For example a topologist would see a doughnut and a coffee cup in

the same way because they both have only one hole. But in the case of a pretzel, it belongs to a different topological class since it has three holes. We can't readily turn a doughnut into a pretzel without creating two extra holes. There are some rigorous mathematical way to tell the difference between a muffin and a doughnut. We can calculate the Gaussian curvature of the surface of the object and integrate it over the entire surface of the object using the Gauss-Bonnet theorem in equation 2.8.

$$\frac{1}{2\pi} \oint K \, \mathrm{d}A = 2 - 2g \tag{2.8}$$

where, K is the Gaussian curvature. As we do the integration, we come up with a number g known as *genus*. It tells us which of these surfaces we have. If we do the integral over a muffin we get $g = 0$, on the other hand for a doughnut, we get $g = 1$, and if we deform that doughnut into a coffee cup, g remains 1 the whole time. Similarly we have the genus $g = 2$, and 3 for a double torus and a three-hole pretzel, respectively. From these examples, it is quite apparent that the genus is related to the number of holes present in a Gaussian geometry. It is not sensitive to the details of the surface, and it is a *topological invariant*. Another important observation that we can make here is that the number of distinct surface states is determined by the number of holes or the genus. For a very long time it was not clear whether the purely mathematical concept of topology could be useful to explain physical phenomena. It turns out that there is a topological invariant associated with the quantum Hall phase. By using the Kubo formula for the Hall conductivity which essentially gives the linear response of a system to an applied electric field in standard perturbation theory. we can determine the Hall conductance as following

$$\sigma_{xy} = \frac{-2e^2}{2\pi h} \sum_\alpha \int_{BZ} d^2k \left(\left\langle \frac{\partial u}{\partial k_1} \bigg| \frac{\partial u}{\partial k_2} \right\rangle - \left\langle \frac{\partial u}{\partial k_2} \bigg| \frac{\partial u}{\partial k_1} \right\rangle \right) \tag{2.9}$$

where the sum is only over the filled bands α. The topology arises from the way the phase of the states winds as we move around the Brillouin zone. This is captured by a *Berry connection* over the Brillouin zone, defined by

$$\mathcal{A}_i(\mathbf{k}) = -i \left\langle u_\mathbf{k} \left| \nabla_{k^i} \right| u_\mathbf{k} \right\rangle \tag{2.10}$$

Here $|u_\mathbf{k}\rangle$ denotes an eigenfunction of the Hamiltonian which satisfies the periodic boundary condition. Now we can as well calculate the field strength or the *Berry curvature* associated with $\mathcal{A}_i$ given by

$$\mathcal{F}_{xy} = \nabla_{k^i} \times \mathcal{A}_i \tag{2.11}$$

We can compute the first Chern number by integrating $\mathcal{F}$ over the Brillouin zone

$$\mathcal{C} = -\frac{1}{2\pi} \int_{BZ} d^2k \mathcal{F}_{xy} \tag{2.12}$$

This is usually known as TKNN invariant, named after Thouless, Kohmoto, Nightingale, and den Nijs (TKNN) [8], and is always an integer. This is one of the major contributions from Thouless, which led him to win the 2016 Nobel prize in physics. The TKNN invariant has a beautiful physical manifestation in terms of the Hall conductance given by

$$\sigma_{xy} = \frac{e^2}{2\pi\hbar} \sum_{\alpha} \mathcal{C}_{\alpha} \tag{2.13}$$

$$\sigma_{xy} = \nu \frac{e^2}{h} \tag{2.14}$$

where the sum is over all filled bands α and $\mathcal{C}_{\alpha}$ is the Chern class associated to the band and ν is known as the Chern number. This is the famous TKNN formula. The TKNN formula states that the Hall conductivity is a topological invariant of the system. It is essential because it goes some way explaining the robustness of the integer quantum Hall effect. An integer, such as the chern number $\mathcal{C}$ can not change continuously. This means that if we deform our system in some way, as long as we retain the assumptions that went into the derivation above, the Hall conductivity can not change: it is pinned at the integer value. The Brillouin zone of a crystal lattice is a torus, because effectively each of its sides meets the other one in a sort of periodic boundary condition. If we integrate the Berry phase that is defined for every state in the Brillouin zone over the torus, it gives an integer. It turns out that this integer is the actual integer which describes the quantized Hall conductance [9] . This means that filled bands are not all alike, they all have zero longitudinal conductivity, but they can have different Hall conductivity depending on their topological property. The generalization unravels an important insight that as the Hamiltonian is adiabatically varied in any closed parameter space, it gives the same topological invariant. It implies that as the electron returns to its starting point, the expectation value of the velocity operator remains the same, but the electron wave function acquires an additional phase. This phase turns out be the "Berry phase", which was proposed by Michael Berry in 1983 [10]. In QHE, current flows along the edges of the 2D sample. Something interesting happens at the edges, and it is worth reviewing the picture which explains how the quantum Hall effect comes about. Any real sample is finite, there must be some confining potential at the edges of the sample which keeps the electrons within the sample. That confining potential causes the Landau levels of the system which we have seen earlier to bend up at the edges shown in fig. 2.2(c). When we put the Fermi energy in between two Landau levels, it must cross the levels at the edges as they become dispersive. These states carry current around the edges of the sample, we can think of them as little skipping orbits of the electrons going around the edge. Notably,

they only carry current in one direction around the edge so that current can't backscatter, it flows without resistance around the edge of the sample. There is a correspondence between what is going on in the bulk and what is going on at the edge. It is guaranteed that the gapless states always show up at the interface between two different topological phases. In the case of QHE, when we have an edge between the quantum Hall system with TKNN = 1 and, vacuum which is topologically a regular insulator with TKNN = 0, there is always a state at the edge which is gapless and metallic. Hence the quantized Hall conductivity is a bulk property as well as an edge property, they are essentially like the two sides of a same coin.

In the integer quantum Hall effect (IQHE), the applied magnetic field provides the 'chirality' for the electrons forming a cyclotron orbit. Without magnetic field, the QH phenomena can be thought of as occurring in a reverse fashion. Here a self-generated chirality of electrons creates a pseudo-magnetic field (*Berry curvature*) in the process of forming 'chiral orbits'. So the next interesting question one might ask is whether *Landau levels are the only system with TKNN invariant $\nu \neq 0$*, the answer is no. There are other systems exist with non-zero TKNN value. Haldane published in 1988 a model for a quantum Hall effect without Landau levels [11]. He suggested that a QHE may also result from breaking of the time-reversal symmetry (i.e., magnetic ordering) without any net magnetic flux through the unit cell of a periodic 2D system. The model is what he called "2d graphite", what we know today as graphene. In the absence of any magnetic field or time reversal symmetry breaking perturbation, the intrinsic chirality of the electron in solid state systems can arise from multiple origins, including Su-Schrieffer-Heeger(SSH) type staggered electron hopping [12], sublattice (often referred to as pseudospin) symmetry in the hexagonal 2D lattice [13], spin-orbit coupling [11], or certain type of even-odd orbital texture mixing [14] as we will discuss in the next section. In a simpler terms, the chirality arises if the electron hopping is complex, because it associated with the electron's hopping. As the Berry curvature pass through a periodic lattice, the Euler characteristic (Gaussian curvature) ensures a quantization of the flux [Eq. (2.8)], this gives rise to a bulk topological invariant. The intrinsic formation of a 'chiral orbit' in a periodic lattice is the foundation of a new quantum states without breaking the time reversal symmetry.

2.3   Quantum Spin Hall State and Topological Insulators

After the breakthrough discovery of graphene [13] which is a two dimensional hexagonal lattice of carbon atoms with two identical atoms in the unit cell, physicists started thinking about what possible perturbations could be applied to the system. The following idea came from Kane and Mele in 2005 [15,16]: We can apply a σ_z term to the Hamiltonian which tries

to rotate the pseudo spin out of the plane, and it corresponds to making the two atoms in the unit cell distinct, and that would open a gap. This is known as staggered sub-lattice potential, the second term in Eq. (2.14) [12]. We can also add a spin-orbit (SO) coupling term, which corresponds to the case when a spin-up electron scatters to a next nearest neighbor and might have a higher probability of going to the left than to the right, and the opposite for spin down. The SO coupling term which is the last term in Eq. (2.14) also opens an energy gap. However, these two energy gaps are not the same. The $4{\times}4$ Hamiltonian including K and $K^{'}$ points reads

$$H = \nu_F(\sigma_x\tau_{\pm}p_x + \sigma_yp_y) + \lambda_{CDW}\sigma_z + \lambda_{SO}\sigma_z\tau_zs_z \tag{2.15}$$

where, $\tau = \pm1$ corresponds to $K(K^{'})$. They both have a gap in the bulk states, but if we look at the states in a ribbon of graphene of finite width and find out that the edge states appear differently. In the case of spin-orbit coupling, we observe edge states that are crossing the bulk gap, which happens without any magnetic field, and this is called the *quantum spin Hall effect* as shown in figure 2.4(a). These edge states which are drawn in red and green "live" on the edges of the sample, and they carry spin-up electrons to the right and spin-down electrons to the left on the top edge, and this reverses on the bottom edge as shown in the fig. 2.4(b). This system does not require a magnetic field, and the effect is only due to spin-orbit coupling, which practically corresponds to two copies of the Haldane model as we have seen above. Here we can view it as the spin-orbit coupling taking over, spin-up electrons follow the Haldane model with a positive magnetic field and spin-down with a negative magnetic field. Kane and Mele [16] also showed that the state is associated with a topological invariant, known as $\mathbb{Z}_2$ invariant which is either 0 or 1. So only two kinds of time-reversal symmetric insulators exist in two dimensions, they are the trivial insulator and the quantum spin Hall insulator. Unfortunately, we did not observe the topological states in graphene due to its weak spin-orbit coupling which requires really low temperature to reach its ground state. In 2006, Bernevig, Hughes, and Zhang have predicted CdTe/HgTe quantum wells as a system which undergoes the topological quantum phase transition above a critical thickness 6.5 μm of a HgTe layer sandwiched between two CdTe layers shown in figure 2.4(c) [17]. This was indeed experimentally observed by König et al. in 2007 by transport measurements [18]. The band structure in fig. 2.4(a) shows the predicted band inversion of s and p derived bands which occurs due to the strong spin-orbit coupling in this system. Though the method applied in ref. [17] for identifying the quantum spin Hall state in HgTe quantum wells was a different one, furthermore, HgTe is of zinc-blende structure and therefore not inversion symmetric. We can apply the method of Fu and Kane [19] just by assuming a model Hamiltonian for HgTe which is inversion symmetric. The $\mathbb{Z}_2$ invariant is then found to be odd, which can be viewed as a proof of concept.
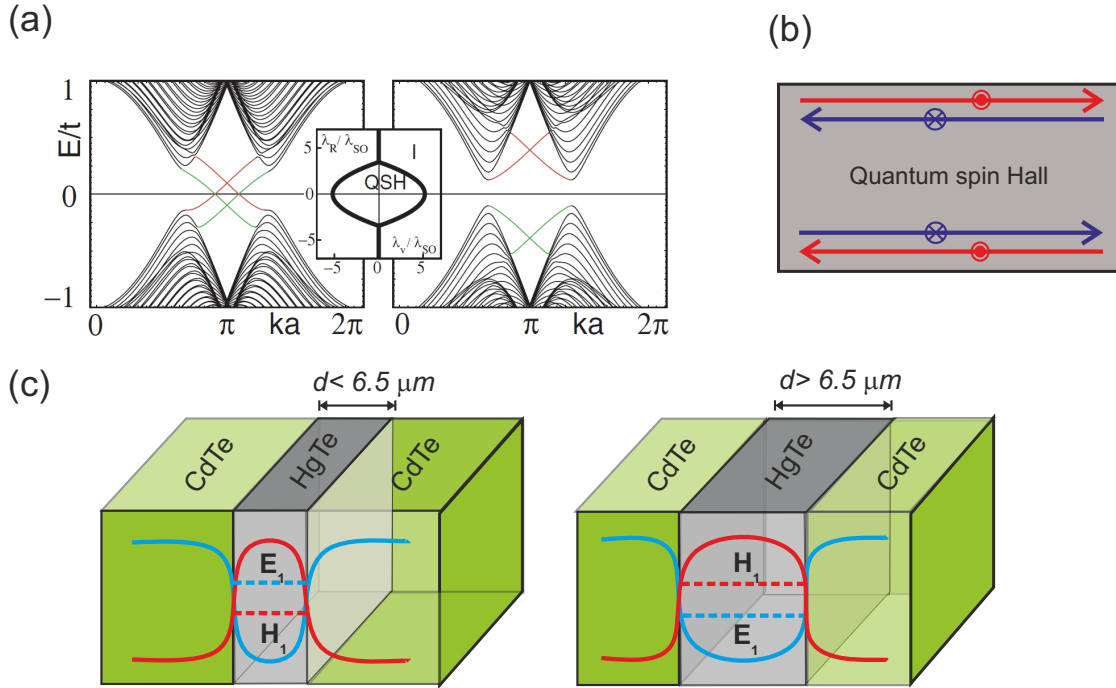
(a)

(b)

Quantum spin Hall

(c)

$d< 6.5 \ \mu m$

$d> 6.5 \ \mu m$

Figure 2.4: Quantun Spin Hall State: *(a) Energy bands of a one-dimensional strip of graphene. Closely spaced lines show the discrete 2D bulk energy levels projected onto the edge Brillouin zone. The green and red lines show the spin-fltered bands localized on either edge of the strip. Left and right side show the spectrum with $\mathbb{Z}_2$ invariant 1 and, 0, where $\mathbb{Z}_2=1$ represents a non trivial topology. Adapted from ref. [15] © 2019, APS. **(b) Quantun Spin Hall bar**: The upper edge contains a forward mover with up spin and a backward mover with down spin, and conversely for the lower edge. **(c)** HgTe quantum wells are two-dimensional quantum spin Hall insulators depending on the thickness (d) of the HgTe layer. Here the blue curve shows the potential-energy well experienced by electrons in the conduction band; the red curve is the barrier for holes in the valence band. Electrons and holes are trapped laterally by those potentials but are free in the other two dimensions.*

It is more complicated to compute the $\mathbb{Z}_2$ invariant than the Chern number in QHE. The $\mathbb{Z}_2$ invariant is not a directly measurable quantity and is often diagnosed by the observation of a topological surface state. The key here is to understand the role of time reversal symmetry $\mathcal{T}$, which is represented by an anti-unitary operator $\Theta = \exp(i\pi S_y/\hbar)K$, where S_y and K are the spin operator and complex conjugation, respectively. For a spin $1/2$ particle the operator has the property $\Theta^2 = -1$. The anti-unitary operator Θ imposes the symmetry in the Bloch Hamiltonian as

$$\Theta\mathcal{H}(\mathbf{k})\Theta^{-1} = \mathcal{H}(-\mathbf{k}) \tag{2.16}$$

It represents the energy bands in a time-reversal symmetric system which have the same energy in $\pm\mathbf{k}$ points, referred as Kramers pairs. In the case of a system with spin-orbit coupling where spin-rotational symmetry is broken but in the presence of the time reversal symmetry $\Theta\,|\mathbf{k},\uparrow\rangle = |-\mathbf{k},\downarrow\rangle$ Kramers pairs are spin degenerate at the time reversal invariant momentum (TRIM) due to the periodicity of the Brillouin Zone. This is known as Kramers' degeneracy. There are many different ways to evaluate the $\mathbb{Z}_2$ invariant. Here we consider Fu-Kane-Mele method as it is often easier to implement especially for a system in the presence of both time reversal symmetry and inversion symmetry [19]. Fu and Kane introduced a concept called *time-reversal polarization* [20] which is a $\mathbb{Z}_2$ quantity characterizes the presence or absence of a Kramers degeneracy associated with a surface. It is similar to the charge polarization in the IQHE based on Laughlin-type gedanken experiment argument [9] which explain the appearance of finite plateaus in real system, Laughlin considered a two dimensional metal loop instead of the plane subjected by a uniform magnetic field B perpendicularly pointing outward everywhere on the surface, and there is fictitious flux Φ inside the loop which can be varied adiabatically. In the quantum spin Hall effect, electron in a Bloch state $u_n(\mathbf{k})$ with its time reversal (TR) conjugate $u_m^*(-\mathbf{k})$ construct an antisymmetric, unitary matrix of the time-invariant operator:

$$w_{mn}(\mathbf{k}) = \langle u_m(-\mathbf{k})\,|\Theta|\,u_n(\mathbf{k})\rangle \tag{2.17}$$

The determinant of the antisymmetric matrix w is represented by the Pfaffian as $[\mathrm{Pf}(w)]^2 = \det(w)$. The sign of the Pfaffian can be defined as

$$\delta_i = \frac{\sqrt{\det[w(\mathbf{k}_i^*)]}}{\mathrm{Pf}[\mathbf{k}_i^*]} = \pm 1 \tag{2.18}$$

The general expression of the $\mathbb{Z}_2$ topological invariant is given by [20]:

$$(-1)^\nu = \prod_{i=1}^{N_i} \delta_i \tag{2.19}$$

where N_i is the total number of the time reversal invariant momenta in the Brillouin zone. In a 2D square lattice, $N_i = 4$, and in a 3D C_4 symmetric lattice $N_i = 8$. For any arbitrary odd number of $\delta_i = -1$ in k space, the $\mathbb{Z}_2$ invariant is always remain $\nu = 1$ otherwise 0. So here we can have only two values of $\nu = 1$ or 0, unlike the integer quantum Hall insulator where any arbitrary Chern number is possible, this is the significance of the $\mathbb{Z}_2$ topological invariant.

2.3.1   3D $\mathbb{Z}_2$ Topological Insulator

One of the exciting things is that, once we remove the need for a magnetic field which has a particular direction, we are no longer required to have topological insulators which are only two-dimensional. Kane and Mele and also Moore and Balents and Rahul Roy proposed independently that there exists a three-dimensional version of the quantum spin Hall insulator [21–23]. In this case, the three-dimensional bulk is insulating, and the two-dimensional surfaces are metallic. On every surface, there are conducting states where the direction of the conduction is tied to the direction of spin. So the spin is helical and wraps around on the k-space, e.g at the Fermi energy, but the spin is perpendicular to the momentum and conduction direction everywhere. This has been schematically shown in Fig. 2.5. Topological invariants for 3D $\mathbb{Z}_2$ topological insulator take four values given by $(\nu_0 : \nu_1\nu_2\nu_3)$, and there is one crucial invariant ν_0 which can either be 1 or 0. The ν_0 invariant describes whether the material is called strong topological insulator when it is 1 or weak topological insulator when it is 0. However, in the case of a weak topological insulator the $\nu_1\nu_2\nu_3$ invariants are non-trivial, and not 0. This necessarily represents a stack of two-dimensional quantum spin Hall insulators in three dimension. A weak topological insulator exhibits even number of Dirac cone surface states which are not robust against disorder. One of the main characteristics of a strong topological insulator is that it has the guaranteed metallic state on every surface, and the energy-momentum dispersion form a odd number of Dirac-cone.

Soon after the theoretical prediction was made for some materials classes Bi_2Se_3, Bi_2Te_3 to be potential candidates for 3D topological insulators, many experimental observations followed [24–28]. It was also possible to find out that the surface states are spin polarized, and the left and right moving surface states have been shown to have different spin polarizations [29–33]. Many groups have studied these materials since then, and it is evident that these are indeed different from a trivial insulators. They are topological, and they posses metallic surface states.

Here we mention the first experimental observation of 3D topological insulator surface states in $Bi_{1-x}Sb_x$ using angle-resolved photoemission spectroscopy, which is an excellent technique to directly map out the electronic band structure of a material [34]. Fig 2.6(a) shows a schematic of the bulk band inversion as a function of x in $Bi_{1-x}Sb_x$. The bulk band
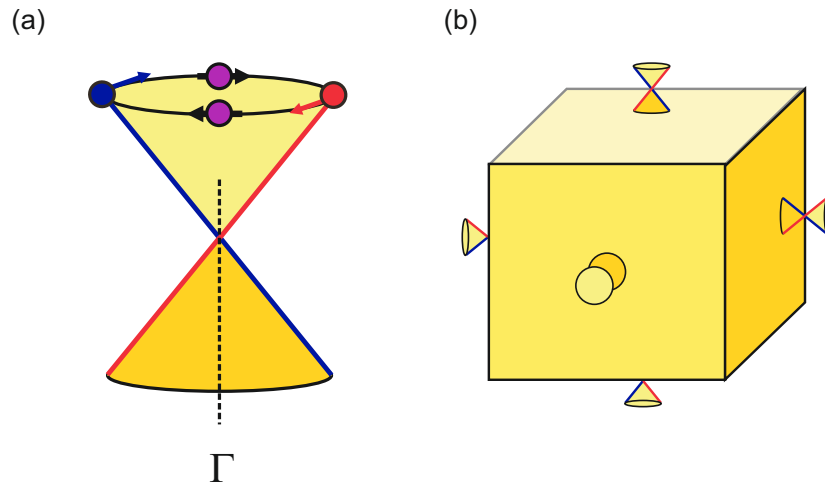
Figure 2.5: 3D topological insulator: *(a) Schematic of 2D surface state with Dirac like linear dispersion at $\overline{\Gamma}$ with spin-momentum locking in 3D topological insulator. (b) Schematic of metallic surface state protected by time reversal-symmetry and characterized by $\mathbb{Z}_2$ invariant, where the material is insulating in the bulk.*
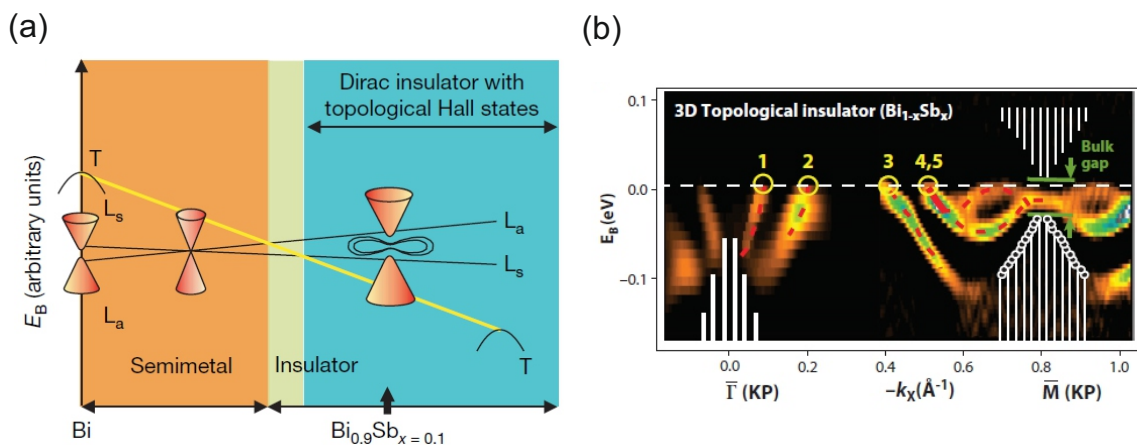
Figure 2.6: *(a) Schematic variation of bulk band energies of $Bi_{1-x}Sb_x$ as a function of x. $Bi_{0.9}Sb_{0.1}$ is a direct-gap bulk insulator well inside the inverted-band regime, and its surface forms a 'topological metal'; the 2D analogue of the 1D edge states in quantum spin Hall systems. (b) Topological insulator Bi-Sb alloy exhibits an odd number of surface state crossings between any pair of Kramers points. Adapted from ref. [34]. © 2008, Springer Nature.*

inversion and corresponding appearance of the surface state is triggered by some particular amount of Sb concentration. In the given example $Bi_{0.9}Sb_{0.1}$ is a direct-gap bulk insulator where the Dirac point is well inside the inverted-band regime, its surface forms a 'topological metal' which is the 2D analogue of the 1D edge states in quantum spin Hall systems. The topological insulator Bi-Sb alloy exhibits an odd number of surface state crossings between any pair of Kramers points shown in figure 2.6(b).

2.3.2   Symmetry-Protected Topological Phases

So far we have discussed the topological classification of the electronic band structure in the presence of spin-orbit coupling and the time reversal symmetry. Subsequent theoretical development of topological band theory and associated experimental evidence have extended the search for topological insulators with other discrete symmetries beyond the time reversal symmetry as well. There have been prediction of observing the topological insulator states with particle-hole symmetry which leads to a rich family of topological superconductors [35,36], mirror symmetry which defines a distinct class of topological insulator called topological crystalline insulator (TCI) [37], and the spontaneous time reversal symmetry breaking topological insulators without external magnetic field, known as quantum anomalous Hall (QAH) insulators [38, 39]. Additionally, insulating state such as disorder, Kondo effect or Hubbard interaction are proposed to give rise to the topological Anderson insulator [40, 41], topological Kondo insulator [42], and topological Mott insulator [43], respectively. They are all associated with odd number of band inversions in the Brillouin zone. In the following sections we will discuss the topological crystalline insulator protected by crystal symmetry, and the quantum anomalous Hall effect by spontaneous breaking of the time reversal symmetry in a magnetic topological insulator which are the main topics of this current thesis.

2.4   Topological Crystalline Insulators

In 2011, Liang Fu extended the band structure classification in a different direction which includes point group symmetries of the crystal, hence proposed a new type of topological insulator known as *"topological crystalline insulators"* [37]. Topological crystalline insulator (TCI) is the counterpart of a topological insulator in materials without (or with) spin-orbit coupling, which cannot be smoothly connected to a trivial band insulator when time-reversal ($\mathcal{T}$) symmetry and a certain point group symmetry are respected. This is one of the main topics of interest of the current thesis. In this section, we will start with the very first hypothetical model which predicted the existence of such exotic TCI phase protected by a fourfold rotational symmetry, featuring quadratic surface states and characterized by two $\mathbb{Z}_2$ topolog-

ical invariants. We will then mention the theoretical prediction and subsequent experimental verification of a TCI phase in the SnTe class of materials with reflection symmetry, and non zero mirror Chern number in the following section.

2.4.1 Topological State with Rotational Symmetry

We consider a most symmetric crystal with fourfold (C_4) or sixfold (C_6) rotational symmetry. This will eliminate the risk of having broken crystal symmetry due to the sample surface which happens in the case of a low-symmetry surface of a topological crystalline insulator which does not have robust surface states. However, it is also not necessary for TCI system to have high spin-orbit coupling, instead, this role can be replaced by the electron's orbital degrees of freedom. The (001) surface of topological crystalline insulators can have *quadratic* band degeneracy protected by time-reversal and discrete rotational symmetry, unlike the Dirac type dispersing surface states in $\mathbb{Z}_2$ topological insulator.
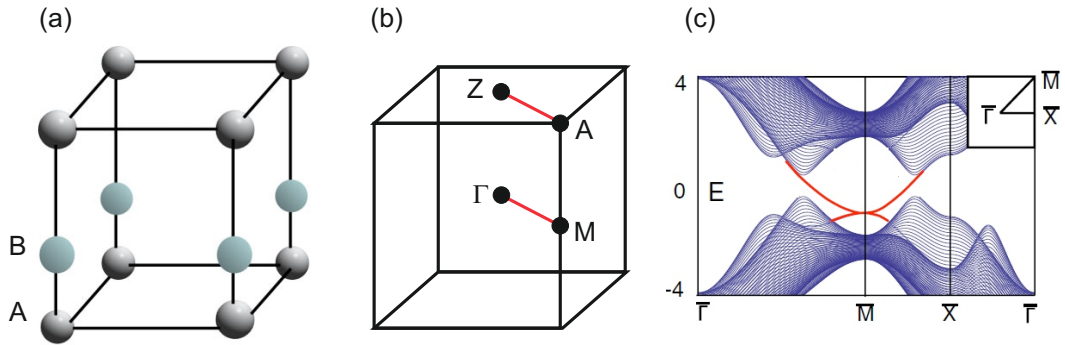

Figure 2.7: *(a) Tetragonal lattice with two atoms A and B along the c axis in the unit cell. (b) The Brillouin zone and four high symmetry points.(c) Band structure along high-symmetry lines in the (001) surface Brillouin zone. A quadratic surface band is highlighted in red. Adapted from Ref. [37]. © 2011, APS.*

To prove the existence of gapless surface states on the (001) surface of a hypothetical crystal with C_4 symmetry, consider a tetragonal lattice with two nonequivalent atoms A and B along the c axis in its unit cell, as depicted in Fig. 2.7(a). Stacking such bi-layer square lattices in *ab*-plane creates the 3D crystal. To describe the band structure of an electron's *p*-orbitals (particularly the energy bands derived from p_x and p_y orbitals) one can introduce a tight binding model [37]. It is assumed that the bands do not overlap with the p_z bands, and construct a tight binding Hamiltonian from the Wannier functions with the same symmetry as p_x and p_y orbitals. The Hamiltonian H consists of an intralayer hopping H^A and H^B, as well as interlayer hopping H^{AB}

$$H = \sum_n H_n^A + H_n^B + H_n^{AB} \tag{2.20}$$

The tight-binding Hamiltonian essentially manifests the perseverance of crystal symmetries. We can also determine the corresponding Bloch Hamiltonian ($H_{\mathbf{k}}$) by Fourier transform of the total Hamiltonian.

$$H(\mathbf{k}) = \begin{pmatrix} H^A(\mathbf{k}) & H^{AB}(\mathbf{k}) \\ H^{AB\dagger}(\mathbf{k}) & H^B(\mathbf{k}) \end{pmatrix} \tag{2.21}$$

This leads to a gapped phase in a finite parameter range everywhere in the Brillouin zone, and the system remains in the same topological class.

Formation of the gapless surface state in such system entirely depends on the surface orientation, which is preserved by the C_4 rotational symmetry. Most remarkably, the (001) surface exhibits metallic surface states which transverse the whole energy gap also preserves the C_4 symmetry. The surface state at the $\overline{M}$ point (π, π) in the surface Brillouin zone is doubly degenerate due to its fourfold rotation. Fig. 2.7(c) shows the two degenerates states form the two dimensional (2D) irreducible real representation of C_4 as a result of time-reversal symmetry for electrons without spin-orbit coupling.

Two bands of the surface states near $\overline{M}$ point are represented by the p_x and p_y orbital, and henceforth the C_4 rotation can be represented by $e^{i\sigma_y\pi/4}$, where σ_y is Pauli matrix. We can determine the surface Hamiltonian in presence of C_4 and time reversal symmetry as following:

$$\mathcal{H}(k_x, k_y) = \frac{k^2}{2m_0} + \frac{k_x^2 - k_y^2}{2m_1}\sigma_z + \frac{k_x k_y}{2m_2}\sigma_x \tag{2.22}$$

Equation 2.21 shows that the preserved symmetry lead to a *'quadratic'* dispersion rather than linear Dirac dispersion as we have seen in the case of a $\mathbb{Z}_2$ topological insulator. It should be noted that the surface state is topologically protected due to $\mathcal{T}$ and C_4 symmetry, and it is doubly degenerate at $\overline{\Gamma}$ and $\overline{M}$ points. There are two distinct ways to connect the doublets along $\overline{\Gamma}\,\overline{M}$ in analogy to the quantum spin Hall insulator. Surface states which cross the Fermi energy an even number of times are not robust and can be destroyed simply by changing the surface potential, they are known as weak topological insulator. On the other hand, the surface states which crosses the Fermi energy an odd number of times along $\overline{\Gamma}\,\overline{M}$ are topologically non-trivial and they are call strong topological insulator as we have seen in the previous section. This gives rise to the $\mathbb{Z}_2$ classification of two topologically distinct phases of the time-reversal-invariant band insulators with fourfold symmetry.

It is also possible to determine the $\mathbb{Z}_2$ topological invariant ν_0 which characterizes the band-structure of a 3D time-reversal invariant insulator without spin-orbit coupling and with C_4 rotational symmetry. It is worth mentioning that the time-reversal symmetry itself is not enough to obtain the protected two-fold degenerate surface state, but with the combination of C_4 rotational symmetry we can achieve the protected degeneracies at four unique momenta

in the 3D Brillouin zone namely, $\Gamma = (0,0,0)$, $M = (\pi,\pi,0)$, $A = (\pi,\pi,\pi)$, $Z = (0,0,\pi)$ which are shown in fig. 2.7(b). The Bloch Hamiltonian for the Bloch wave function $|\psi_n(\mathbf{k})\rangle = e^{i\mathbf{k}\cdot\mathbf{r}}|u_n(\mathbf{k})\rangle$ of the occupied bands is defined by:

$$\mathcal{H}(\mathbf{k}) = e^{-i\mathbf{k}\cdot\mathbf{r}}He^{i\mathbf{k}\cdot\mathbf{r}} \tag{2.23}$$

$\mathcal{H}(\mathbf{k})$ of the system commutes with the unitary operator $U = e^{i\hat{L}_z\pi/2}$ and represents the C_4 rotation given as

$$\mathcal{H}(k_x, k_y, k_z) = U\mathcal{H}(-k_x, k_y, k_z)U^{-1} \tag{2.24}$$

The time-reversal invariant anti-unitary operator T without spin orbit coupling ($T^2 = 1$) given as

$$\mathcal{H}(k_x, k_y, k_z) = \mathrm{T}\mathcal{H}(-k_x, -k_y, -k_z)\mathrm{T}^{-1} \tag{2.25}$$

The Bloch Hamiltonian $\mathcal{H}(\mathbf{k}_i)$ of the system at the high symmetry point $\mathbf{k}_i$ commutes with the unitary operator U, and it determines the energy states as eigenstates of fourfold rotation with possible rotation eigenvalues 1, -1, i, and $-i$. As $\mathcal{H}(\mathbf{k}_i)$ is real, the eigenstate with eigenvalues $\pm$ at the high symmetric points are guaranteed to have degeneracy. It can also be shown that the doubly degenerate bands at Γ, M, A and Z only be classified by $\mathbb{Z}_2$ invariants.

By following the steps to determine the topological invariant for the $\mathbb{Z}_2$ topological insulator as seen in the previous section, we can now determine the invariant for the TCI:

$$(-1)^{\nu_0} = (-1)^{\nu_{\Gamma M}}(-1)^{\nu_{AZ}} \tag{2.26}$$

$$(-1)^{\nu_{k_1 k_2}} = \exp\left(i\int_{k_1}^{k_2} d\mathbf{k} \cdot \mathcal{A}_\mathbf{k}\right)\frac{\mathrm{Pf}[w(\mathbf{k}_2)]}{\mathrm{Pf}[w(\mathbf{k}_1)]} \tag{2.27}$$

where, $\mathcal{A}_\mathbf{k}$ is defined as $U(1)$ Berry connection and $w(\mathbf{k}_i)$ is an antisymmetric $U(2N)$ matrix. $\nu_{\Gamma M}$ and ν_{AZ} represent the line integral along any arbitrary line connecting Γ and M in the $k_z = 0$ plane, and A and Z in the $k_z = \pi$ respectively as shown in the figure 2.7 (b). We can determine $(-1)^{\nu_{k_1 k_2}} = \pm 1$ as a gauge invariant $\mathbb{Z}_2$ quantity, and $\nu_{\Gamma M}$, ν_{AZ} as $\mathbb{Z}_2$ topological invariants for 2D momentum space $k_z = 0$ and $k_z = \pi$, respectively. ν_0 is the topological invariant for 3D with time-reversal symmetry and C_4 rotational symmetry. Only $\nu_0 = 1$ determines the appearance of the surface state at the (001) surface, whereas $\nu_{\Gamma M}$, ν_{AZ} are weak indices $\mathbb{Z}_2$ analogous to the 3D topological insulators. The crucial fundamental difference between 3D topological insulator and TCI is that the non-trivial topology arises only from the doublet bands for the latter.

2.4.2 Topological State with Mirror Symmetry

In this section we will discuss the existence of a topological state with respect to the mirror symmetry of the crystal. The recent theoretical prediction and subsequent experimental evidence has attracted much interest to explore this novel state in more detail. In the review article by Ando and Fu the reader can find more detailed theoretical descriptions of TCI phase protected by mirror symmetry [44].

In the previous section we have discussed the topological surface state protected by time reversal symmetry together with C_4 rotational symmetry. This ensures topological protection of the doubly degenerate band at the (001) surface unique to topological crystalline insulators with rotation symmetry, and without spin-orbit coupling. Here we will discuss the topological surface state protected by the mirror or reflection symmetry with respect to a crystal plane.
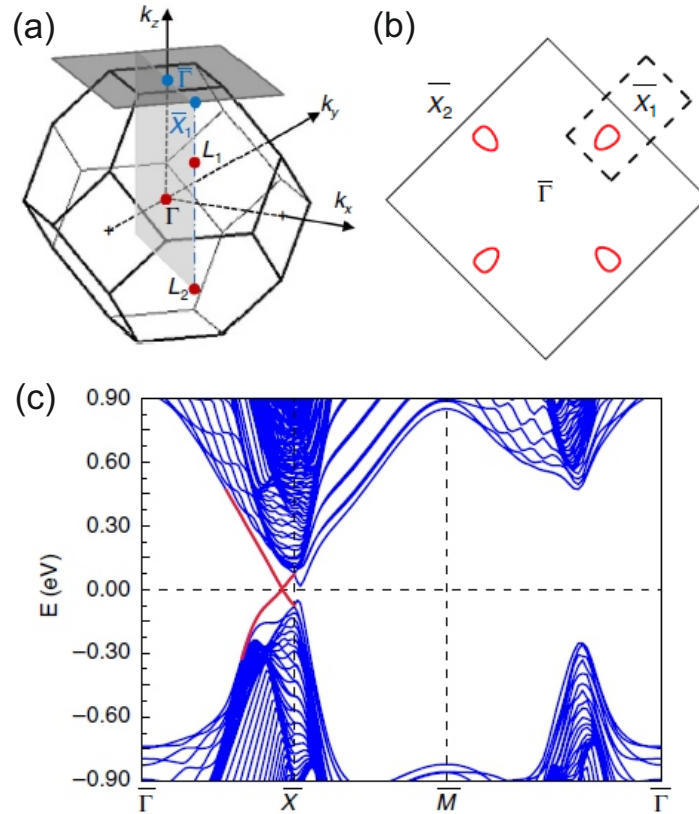

Figure 2.8: Observation of topological crystalline insulator in SnTe: *(a) The face centered cubic (FCC) Brillouin zone showing the plane $\Gamma L_1 L_2$, which is invariant under reflection about the (110) axis and projects onto the ΓX_1 line in the [001] surface. (b) Fermi surface of the (001) surface with four topologically protected Dirac-cone pockets. Note that in between $\overline{\Gamma}$ and $\overline{X}$ two surface bands with opposite mirror eigenvalues cross the Fermi energy with $n_M = -2$. (c) Corresponding band dispersion and existence of surface state marked with red line. Adapted from Ref. [45]. © 2012, Springer Nature.*

Let's assume a three dimensional cubic system which possess reflection symmetry with

respect to a plane and also holds time reversal symmetry. We can define a unitary operator M, which represents the mirror symmetry operation. If the mirror plane for example is along the xy plane, the mirror operation takes $z \mapsto -z$. It is now possible to define the Bloch Hamiltonian as

$$\mathcal{H}(k_x, k_y, k_z) = M\mathcal{H}(k_x, k_y, -k_z) \qquad (2.28)$$

This shows us that the Bloch Hamiltonian commutes with the mirror operator M in the planes $k_z = 0$ and $k_z = \pi$, which are mirror-invariant. The operator M has the property $M^2 = -1$, therefore, the Bloch eigenfunction in $k_z = 0$ and $k_z = \pi$ planes can have two eigenvalues $+i$ or $-i$ respectively. For each class of Bloch eigenstates with eigenvalues $\eta = \pm i$, we can define corresponding Chern numbers N_η. We can then define two independent topological invariants as follows. *total Chern number* $N = N_{+i} + N_{-i}$; *mirror Chern number* $N_M = (N_{+i} - N_{-i})/2$. This allow us to define a TCI phase protected by mirror symmetry, even when the total Chern number is 0. It is worth to mention that due to the lower symmetry at the boundary compared to the bulk, only those surfaces which have the corresponding mirror symmetry can have topologically protected surface states.

In 2012, Hsieh et al. has shown that SnTe which is a IV-VI semiconductor can have non-trivial surface states protected by mirror symmetry [46]. SnTe has rock-salt crystal structure with three different mirror symmetry planes namely (001), (110) and (111). Figure 2.8(a) shows the face-centered-cubic (FCC) Brillouin zone with the plane $\Gamma L_1 L_2$ which is invariant under reflection about the (110) plane onto the $\overline{\Gamma X_1}$ line in the (001) surface. The plane gives rise to a mirror Chern number $N_M = -2$. The corresponding band dispersion and the existence of a surface state marked in red is shown in fig. 2.7(c). Our experimental observation of the TCI phase in $Pb_{1-x}Sn_xSe$ and $Pb_{1-x}Sn_xTe$ system are presented in the chapter 4 and chapter 5 of this thesis, respectively.

2.5 Quantum Anomalous Hall State

The predecessor of the anomalous quantum Hall effect dates back to the year 1881 when Edwin Hall observed that the Hall voltage is 10 times larger in ferromagnetic material than in a non-magnetic conductor [47]. This effect became later known as anomalous Hall effect. Since then numerous studies have been performed to understand the origin of the anomalous Hall effect. The key factors which lead to the observation of this effect are mainly magnetism, spin-orbit coupling and disorder effects. As we have already seen in the earlier section, the discovery of the quantum Hall effect has raised many intriguing questions. We mentioned that the Haldane model opened up the idea of existence of such exotic quantum anomalous Hall (QAH) phase theoretically, which was nevertheless experimentally unsuccessful to observe in
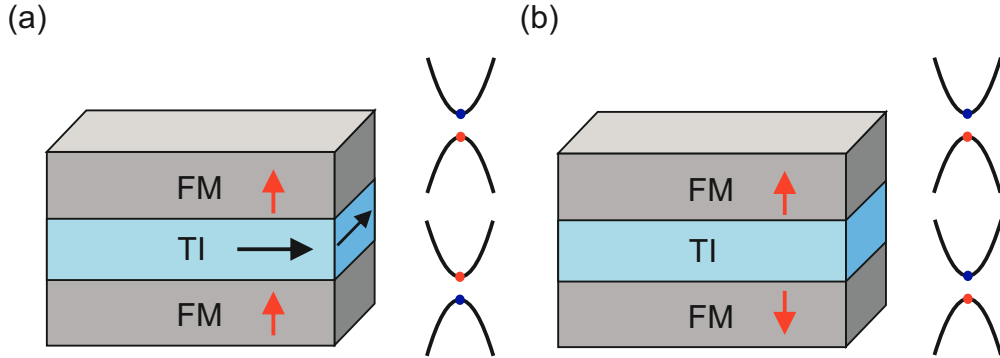
a real system.

Figure 2.9: *Illustration of the Hall conductance in ferromagnet-topological insulator hetero-structure.* ***(a)*** *When the magnetization at the top and bottom surfaces are parallel, there is a quantized Hall conductance accompanied by a chiral edge state in topological insulator films.* ***(b)*** *When the magnetization are anti-parallel, the Hall conductance from the top and bottom surfaces cancel each other. Adapted from Ref. [48]. © 2016, Annual Reviews.*

We have discussed in the earlier section that we can consider the quantum spin Hall (QSH) states as two copies of Haldane model for two electrons with opposite spin. Intuitively we can think of the electrons in the QSH state with one spin component as already in the QAH state, but due to the time reversal symmetry two electrons with opposite spin results into zero net Hall conductance. An initial proposal was to introduce ferromagnetism in two dimensional topological insulators e.g doping HgTe/CdTe quantum wells with Mn impurities, which will break time reversal symmetry and suppress one of the spin channels in the QSH edge state and give rise to a quantized Hall conductance e^2/h [49]. In this section, we will describe the basic mechanism of the quantum anomalous Hall effect by breaking the time-reversal symmetry in a magnetic topological insulator. There are a few review articles available on this topic with more detailed theoretical descriptions as well as recent experimental evidences [48, 50–52].

The surface state of a 3D TI with a single Dirac cone can be expressed by the low energy effective Hamiltonian as

$$\mathcal{H}_{surf}(k_x, k_y) = \upsilon_F \left(\sigma^x k_y - \sigma^y k_x \right) \tag{2.29}$$

where, we consider the sample surface lies on the xy plane, z direction is perpendicular to the sample surface, and υ_F represents the Fermi velocity. Now we can add a time reversal breaking ferromagnetic perturbation at the surface, and the corresponding Hamiltonian is given by $\mathcal{H}_1 = \sum_{a=x,y,z} m_a \sigma^a$. The total Hamiltonian has the energy:

$$E_k = \pm \sqrt{(\upsilon_F k_y + m_x)^2 + (\upsilon_F k_x - m_y)^2 + m_z^2} \tag{2.30}$$

We can further obtain that only the $m_z \sigma^z$ term destabilizes the surface state and opens

up a gap, which is odd under time-reversal. We calculate the QH conductance, which is half integer in this particular case, expressed as:

$$\sigma_{xy} = \frac{m_z}{|m_z|} \frac{e^2}{2h} \tag{2.31}$$

The half integer QH conductance is unique to the 3D TI surfaces, which originates from the non-trivial bulk topology. The surface of a 3D TI has no edge, and it is always represented by a closed two dimensional manifold. This makes it impossible to measure the half-integer QH conductance in 3D TI–unlike the IQHE which is a measurable effect. Alternatively if we create a ferromagnetic phase in the 3D TI by magnetic doping, this will lead to a magnetic domain wall on the side surfaces. So from the above equation this will give rise to a Hall conductance of e^2/h, and there will be a chiral edge state at the domain wall. Fig. 2.9 shows the Hall conductance in a ferromagnet-topological insulator heterostructure. When the magnetization at the top and bottom surfaces are parallel, there is a quantized Hall conductance accompanied by a chiral edge state in topological insulator films fig. 2.9(a). However, when the magnetizations are anti-parallel, the Hall conductance from the top and bottom surfaces cancel each other (fig. 2.9(b)).
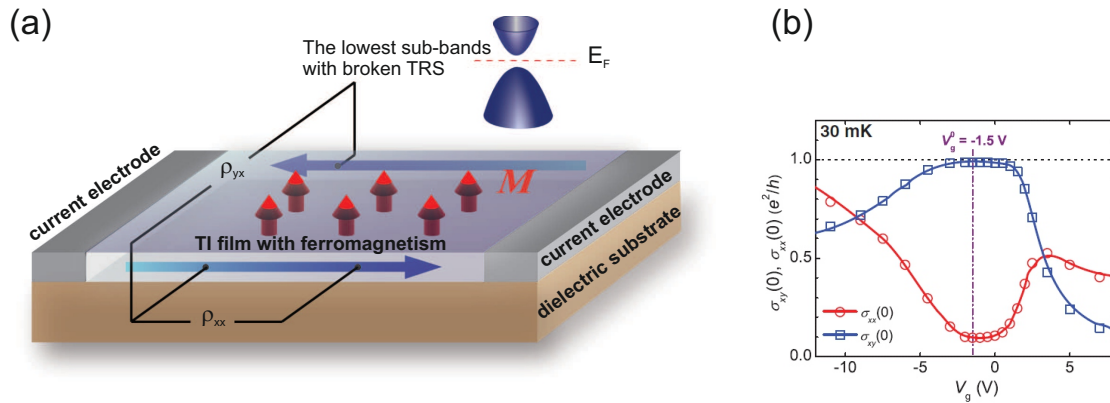

Figure 2.10: Quantum Anomalous Hall effect: *(a) A schematic drawing depicting the principle of the QAH effect in a TI thin film with ferromagnetism. The magnetization direction (M) is indicated by red arrows. The chemical potential of the film can be controlled by a gate voltage (V_g) applied on the back side of the dielectric substrate. (b) Dependence of Hall conductance and longitudinal conductance at zero magnetic field $\sigma_{xy}(0)$ (empty blue squares) $\sigma_{xx}(0)$ (empty red circles) on V_g respectively. Adapted from ref. [53]. © 2013, AAAS.*

Theoretical prediction has been made for the tetradymite semiconductor family: Bi_2Te_3, Bi_2Se_3, and Sb_2Te_3 which form magnetically ordered insulators when doped with transition metal elements such as chromium (Cr) or iron (Fe) [54]. In the case of a 3D topological insulator, magnetization creates a gap at the surface Dirac point which leads to a half quantized Hall conductance $e^2/2h$ due to broken time reversal symmetry. In a 3D TI film with

perpendicular magnetization, the top and bottom surfaces give rise to a gapped Dirac cone which have distinct topological characters due to their opposite normal direction. On the contrary, the edge state is gapless as the magnetization direction is parallel to this plane. This is viewed as a domain wall between the upper and lower surface, which induces a chiral edge state that carries a Hall conductance of e^2/h giving rise to quantum anomalous Hall effect [55]. Carefully tuning the Fermi level by a gate voltage into the magnetization induced gap gives rise to a quantized Hall conductance $\sigma_{xy} = e^2/h$, and zero longitudinal conductance σ_{xx} without an external magnetic field. Recent experimental evidence report the observation of the quantum anomalous Hall effect in thin films of chromium-doped $(Bi,Sb)_2Te_3$, a truly both insulating and magnetic topological insulator [53]. At zero magnetic field, the gate-tuned anomalous Hall resistance reaches the predicted quantized value of h/e^2, accompanied by a considerable drop in the longitudinal resistance. Under a strong magnetic field, the longitudinal resistance vanishes, whereas the Hall resistance remains at the quantized value shown in fig 2.10(a,b).

2.6 Spin Orbit Coupling and Rashba Effect

It is essential to discuss the Rashba effect and the origin of spin-split trivial surface state due to the broken structural inversion symmetry at the surface within the scope of this thesis. The effect which was first discovered by Emmanuel Rashba in 1960 is crucial for creating spin polarized electronic states for technological applications in spintronics.

Besides the Zeeman splitting which gives rise to spin split electronic bands due to the magnetic field, it is also possible to achieve a similar situation in the presence of external electric fields. In this case, it is due to the effective magnetic field seen by the electron in its rest frame. When an electron moves with velocity $\vec{v}$ in a perpendicular electric field $\vec{E}$, the effective magnetic field experienced by the electron is given by

$$\mathbf{B}_{eff} = \frac{1}{c^2}\vec{E} \times \vec{v} \tag{2.32}$$

The spin-orbit coupling Hamiltonian can be written in terms of the Dirac equation:

$$\mathbf{H}_{SO} = -\frac{e\hbar}{4m_e^2 c^2}\sigma(\mathbf{E} \times \mathbf{p}) = -\frac{\mu_B}{2m_e c^2}\sigma(\mathbf{E} \times \mathbf{p}) \tag{2.33}$$

where μ_B is the Bohr magneton, m_e the electron mass, $\mathbf{p}$ is electron momentum and $\sigma = (\sigma_x, \sigma_y, \sigma_z)$ the Pauli spin matrices related to a spin operator by $\hat{\mathbf{S}} = \frac{\hbar}{2}\sigma$.

$$\sigma_x = \begin{pmatrix} 0 & 1 \\ 1 & 0 \end{pmatrix} ; \sigma_y = \begin{pmatrix} 0 & -i \\ i & 0 \end{pmatrix} ; \sigma_z = \begin{pmatrix} 1 & 0 \\ 0 & -1 \end{pmatrix} \tag{2.34}$$

When an electron moves in a 2D plane with momentum $\mathbf{p} = \hbar\mathbf{k} = \hbar(k_x, k_y, 0)$ and the external electric field is normal to the plane $E = (0, 0, E_z)$, the above Hamiltonian transform to:

$$\mathbf{H}_{SO} = -\frac{\mu_B}{2m_e c^2} E_z (\sigma_x k_y - \sigma_y k_x) = \alpha_R (\sigma_x k_y - \sigma_y k_x) = \alpha_R \begin{pmatrix} 0 & k_y + ik_x \\ k_y - ik_x & 0 \end{pmatrix} \quad (2.35)$$

where the Rashba-parameter $\alpha_R \propto E_z$ depends linearly on the electric field or the potential gradient $-\frac{\partial \Phi(z)}{\partial z}$ which determines the strength of the Rashba spin-orbit coupling. In the case of time reversal symmetry, the transformation $t \to -t$ changes the electron momentum from $\mathbf{k}$ to $-\mathbf{k}$ and inverts the electron spin. As we have mentioned earlier this leads to the so-called Kramers degeneracy, and the energy relation is expressed as

$$E(\mathbf{k}, \uparrow) = E(-\mathbf{k}, \downarrow) \quad (2.36)$$

where, $\uparrow$ ($\downarrow$) represents spin-up (spin-down) electrons.
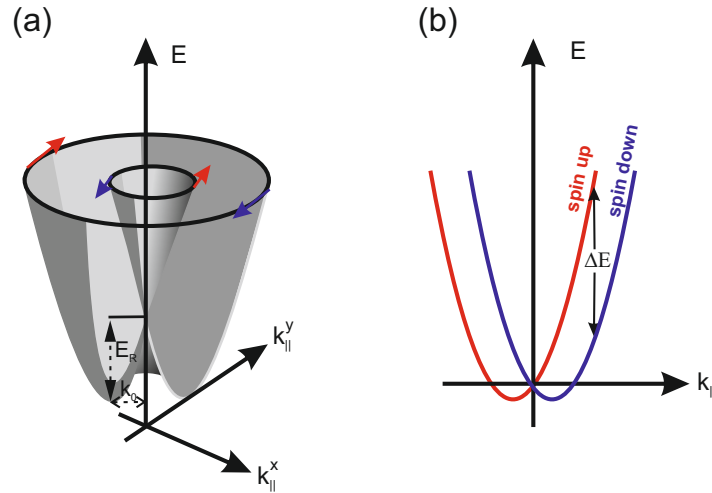

Figure 2.11: Rashba effect: *(a) Effect of the Rashba-type spin-orbit interaction on the parabolic energy dispersions of a nearly-free electron system at the surface. The spin-degenerate bands are shifted by k_{SO} and the energy splitting vanishes in the center of the surface Brillouin zone. The Fermi surface becomes two concentric circles with opposite spins. (b) Two components with opposite spin: red - spin up and blue - spin down.*

In a crystal with an additional inversion symmetry, the energy relation is expressed as $E(\mathbf{k}, \downarrow) = E(-\mathbf{k}, \downarrow)$, which in turn means that all electronic bands are spin-degenerate. At surfaces and interfaces due to the appearance of a potential gradient, the Rashba parameter becomes nonzero and the energy relation is $E(\mathbf{k}, \uparrow) \neq E(-\mathbf{k}, \downarrow)$, which leads to a lifted degeneracy of the bands with different spins. In the case of a two-dimentional electron gas, the full solution is represented by two parabolic bands with opposite spins shifted by $k_{\parallel}$

relative to each other. The energy eigenvalues are given by

$$E_\pm = \frac{\hbar^2 \mathbf{k}_{||}^2}{2m_e} \pm \alpha_R \left| \mathbf{k}_{||} \right| \tag{2.37}$$

The minimum energy E_0 at $\pm k_0$ of these parabolas is given by:

$$k_0 = \frac{m_e \alpha_R}{\hbar^2}; E_0 = -\frac{m_e \alpha_R^2}{2\hbar^2} \tag{2.38}$$

Apart from the applied external electric field E_z which we have discussed above, the work function step at the sample surface or interface between two materials, and a heavy metal with high atomic number enhances the Rashba effect. Fig. 2.11 (a) shows the effect of the Rashba-type spin-orbit interaction on the parabolic energy dispersion of a nearly-free electron system at the surface. The spin-degenerate bands are shifted by k_{SO}, and the energy splitting vanishes at the center of the surface Brillouin zone. The Fermi surface becomes two concentric circles with opposite spins shown in fig. 2.11. Rashba type spin-orbit split surface states have been demonstrated by some pioneering experimental work. The Au(111) Rashba type surface state was shown by Lashell et al. [56]. Subsequently, spin-orbit split surface states were identified in other metals such as W [57, 58], Bi [59], and Gd [60] with high atomic number (Z). However, the low-Z metals Mo [57], and Ag [61] showed smaller or vanishing splitting.
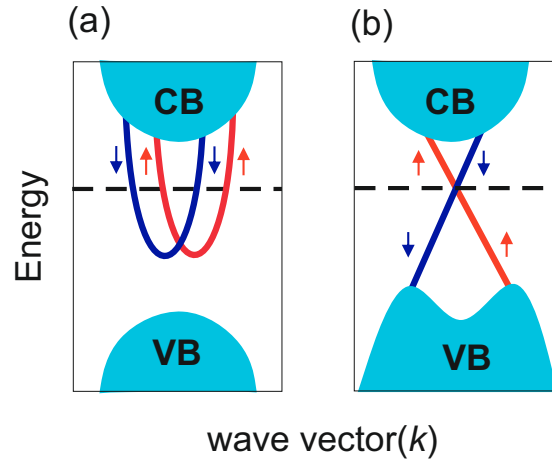

Figure 2.12: *Difference between the Rashba type SOC split bands in a trivial surface and in the topological edge/surface state. **(a)** For Rashba SOC, the split bands bend backward at higher momentum as the quadratic term in the kinetic energy begin to dominate over the SOC. Thus the 2D bands fail to connect both conduction and valence bands and remains topologically trivial. **(b)** On the contrary the surface state of a TI remains 'massless' it connects the bulk valence band to obey the bulk boundary correspondence.*

Indeed, owing to the loss of inversion symmetry at the surface of a TI, the surface states actually originate from a lifted spin degeneracy due to spin-orbit coupling (SOC) with a cru-

cial difference. In the topological surface state, the kinetic energy of each spin is much smaller compared to the SOC strength. This is a manifestation of the bulk-boundary correspondence of the TI. For the Rashba-band, in Fig. 2.12(a), each spin band bends backward away from the time reversal momenta as the kinetic energy term dominates over the SOC term at higher momenta. The Rashba-bands are also not required to connect to the bulk states at all. On the other hand, topological surface states are required to adiabatically connect to both the bulk conduction and valence bands, and thus cannot bend backward and rather disperse across the bulk insulating gap, illustrated in Fig. 2.12(b). It is obvious that not all surface states are topological surface states. More importantly, even in a topological insulator not all surface states are necessarily topological surface states as well [62]. A topological surface state must have a Dirac cone at the time reversal invariant point where band inversion occurs in the bulk connecting the valence and the conduction bands. There are also cases where an apparently isolated topological state may arise which is not connecting any other state [63].

Summary

In this chapter, we have seen successful classification of solid sate materials in terms of topology, beyond the band theory picture. Spin polarized surface state of $\mathbb{Z}_2$ topological insulator is realized due to high spin orbit coupling and protected by the time reversal symmetry. We discussed a new type of topological insulator known as topological crystalline insulator where the surface state is protected by the mirror symmetry of the crystal, and characterized by the mirror Chern number. We also discussed the preconditions to observe the quantum anomalous Hall effect experimentally in the the context of the present thesis by magnetic doping in $\mathbb{Z}_2$ topological insulator. The difference between the Rashba type surface state and the topological surface state have been discussed as well. Since the topic is new and exciting, there are many extensive reviews available in various forms. Three review articles are published in the Review of Modern Physics [36, 64, 65]. Topological band theory and topological field theories are discussed extensively in Ref. [64, 66] and [67] respectively. A topological insulator materials repository can be found in Ref. [68]. Quantum spin Hall effect [69] and quantum anomalous Hall effect [48, 52, 70] are also reviewed separately. Some books are covering the basics of various topological insulators [71, 72].

Chapter 3

Experimental Techniques

As the concept of topological insulators came from the topology of the electronic band structure, it is crucial to study its properties for fundamental concepts and future technological applications. Photoemission spectroscopy proved to be one of the direct and extensive experimental methods to study the electronic band structure of metals, superconductors, and correlated systems, to name a few. Many new topological insulators have also been experimentally discovered and studied further using this technique. In this chapter we will introduce the basic principles of photoemission spectroscopy which has been used to probe the surface states of topological crystalline insulators, and magnetic topological insulators in the context of the present thesis. In addition, we will mention about synchrotron radiation as a photon source and our sample preparation techniques for the experiment.

3.1   Photoelectron Spectroscopy

3.1.1   Single Electron Picture

Photoelectron spectroscopy is a well established tool based on the principle of the photoelectric effect discovered by Heinrich Hertz in 1887 while doing experiments with electric sparks created by electrodes illuminated with ultraviolet light [73]. Later the phenomenon was quantitatively explained by Albert Einstein in 1905 introducing the photon as quantum of light with the fundamental photoelectric equation [74, 75]:

$$E_{\text{kin}}^{\max} = h\nu - \Phi_0 \tag{3.1}$$

The Einstein equation relates to the maximum kinetic energy E_{kin} of an electron emitted by the photoelectric effect with the quantized photon energy $h\nu$ minus the minimum energy required to release the electron from the solid, the so called *work function* Φ_0. It depends on the material and crystallographic phase and has a typical value of 4–5 eV as a measure of the potential barrier at the surface which prevents the valence electrons from escaping into the vacuum. One of the foundations for studying the electronic band structure of solids using photoelectron spectroscopy was laid by Kai Siegbahn who received the Nobel prize in 1981 for his work [76]. He referred to the technique as Electron Spectroscopy for Chemical Analysis (ESCA), as the core levels have typically small energy shifts depending on the chemical environment of the atom which is ionized, thus allowing the determination of the chemical structure. If a monochromatic source of photons with frequency ν and work function of the material Φ_0 is known the equation 3.1 can be extended as a first approximation to determine the binding energy E_B of the electron by the following equation.

$$E_B = h\nu - E_{\mathrm{kin}}^{\max} - \Phi_0 \tag{3.2}$$

The fundamental principle of the photoemission process is sketched in Fig. 3.1. In a simplified *single-particle picture*, i.e. a non-interacting electron system, the density of occupied states of a solid as a function of binding energy and the number of detected electrons as a function of kinetic energy.
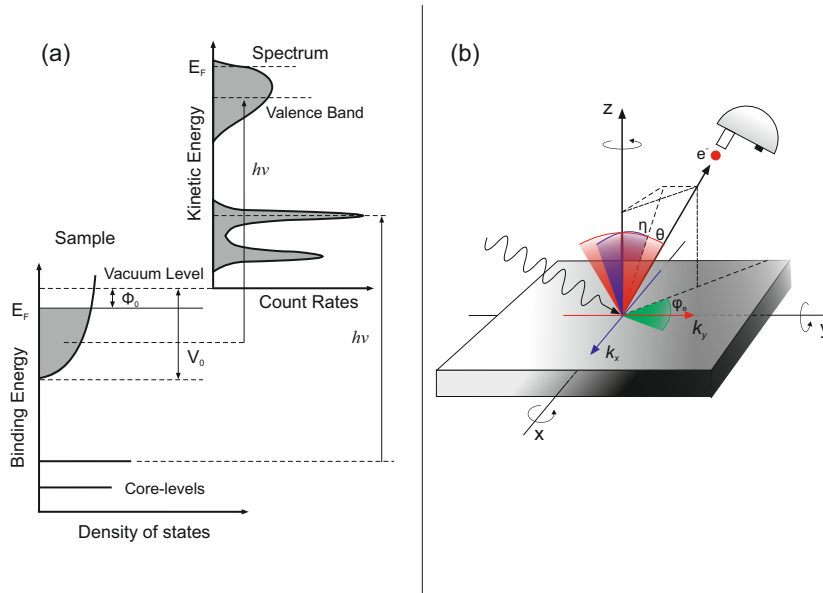

Figure 3.1: *(a) Schematic of Photoemission process in single electron picture using monochromatic light. Density of states of the electrons is measured by the photoelectron count rate as a function of the kinetic energy.(b) Schematic of angle resolved photoemission experiment.*

The excitation of the photoelectron is much more complicated than the simplified illustration shown previously (Fig. 3.1). As a quantum mechanical process it involves many body interaction with all possible interactions with the incident photon in the sample. However we can explain many photoemission application within the single particle picture which does not involve electronic correlation effects such as satellites in the spectra or features like line shapes [77].

3.1.2   Three Step Model

The single particle picture involves three independent steps: (i) photo-excitation of an electron, (ii) transport of that electron to the surface, and (iii) escape from the surface into free electron state in vacuum [77, 78].
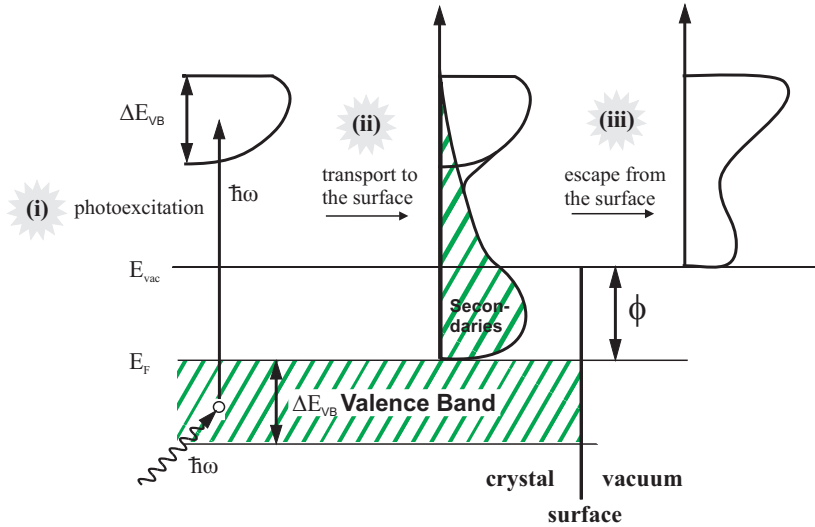

Figure 3.2: Three Step Model of photoemission: *(i) Excitation of the electron by photon **(ii)** transport of the photo-excited electron to the sample surface and **(iii)** escape of the electron from the sample surface.*

(i) Photo excitation process

The transition rate or the *transition probability* of the photo excitation from the initial state (*occupied eigen state*) $|\psi_i\rangle$ to the final state $|\psi_f\rangle$ (Fig. 3.2) due to absorption of the photon can be derived from first order perturbation theory. According to Fermi's Golden Rule the transition rate is expressed as

$$P_{fi} = \frac{2\pi}{\hbar} \left| \left\langle \psi_f | H^{'} | \psi_i \right\rangle \right|^2 \delta(E_f - E_i - \hbar\omega) \tag{3.3}$$

where the δ function guarantees energy conservation and $H^{'}$ is the perturbation due to the photon. The perturbation in the photoemission process has been calculated using the non relativistic Schrödinger approach where the electrons are treated as spinless particles,

which does not allow one to get information about the spin of the electrons. As in our measurements we mainly focus on the the spin integrated photoemission, such description is adequate [79]. If we consider the electron in an external electromagnetic field, the electron momentum $\mathbf{p}$ will be replaced by $(\mathbf{p} - \frac{e\mathbf{A}}{c})$ where $\mathbf{A}$ is the vector potential and can be expressed as $\mathbf{A} = \mathbf{A_0}e^{i\omega t}$. In the non-relativistic limit, the perturbation due to the external field arising from the incident photon can be expressed by [77, 79]

$$H^{'} = \frac{e}{2mc}(\mathbf{A} \cdot \mathbf{p} + \mathbf{p} \cdot \mathbf{A}) + \frac{e^2}{2mc^2}|\mathbf{A}|^2 + e\phi \tag{3.4}$$

where e and m denote electron charge and mass as usual. The order of magnitude of the second term on the right hand side is $\frac{e\vec{A}}{c\vec{p}}$, where $\vec{p} = i\hbar\nabla$ is the momentum operator and negligibly small in experimental terms. Thus we can neglect this term in the first order perturbation theory. The third term is a constant and a suitable choice of energy allows this term to vanish. Using the commutation relation $\left[\vec{A}, \vec{p}\right] = -i\hbar\nabla \cdot \vec{A}$ and dipole apporximation, i.e, $\nabla \cdot \mathbf{A} = 0$ the transition probability can be written as

$$P_{fi} \propto |\langle\psi_f|\mathbf{A}.\mathbf{p}|\psi_i\rangle|^2\delta(E_f - E_i - \hbar\omega) \tag{3.5}$$

The matrix elements in Eq. 3.5 introduce selection rules, which can be used to determine the symmetry of the initial state [80]. In the non relativistic picture, the excitation by the linearly (circularly) polarized light between the one electron states, $|nlm_l\rangle$ is allowed for $\Delta l = \pm 1$ and $\Delta m_l = 0$ (± 1 depending on the direction of the polarization). In the relativistic limit a spin-orbit term is included and one has to consider the total angular momentum j and the selection rules become $\Delta j = 0, \pm 1$ and $\Delta m_j = \pm 1$ [79].

(ii) Transport of the photoexcited electron to the sample surface

In this stage the photo-excited electron travels through the solid to the sample surface. The number of electrons that are transported through the crystal depends on its thickness. Inelastically scattered electrons are practically lost for the band structure determination. Electron-phonon interaction becomes important at very low energies only and can be neglected for the moment [77]. The intensity of the electron close to the sample surface can be expressed as

$$I(d) = I_0 \exp[-(d/\lambda \cos\theta)] \tag{3.6}$$

where d is the depth perpendicular to the surface which contribute to the photoemission signal at the detection angle θ, and λ is called the inelastic mean free path of the electrons (IMFP). This electron mean free path depends mainly on the electron energy. The shortest mean free path is often found within the energy range of 40 eV to 100 eV which makes photoelectron spectroscopy a very surface sensitive technique. However for higher energies

the inelastic mean free path is described by a semiempirical formula [81]:

$$\lambda = 0.41a^{3/2}\sqrt{E_{\text{kin}}} \qquad (3.7)$$

where a the lattice constant of the material expressed in nm and E_{kin} is the kinetic energy of the electron in eV. The dependence of λ on the kinetic energy is shown in Fig 3.3, the so-called universal curve [81].
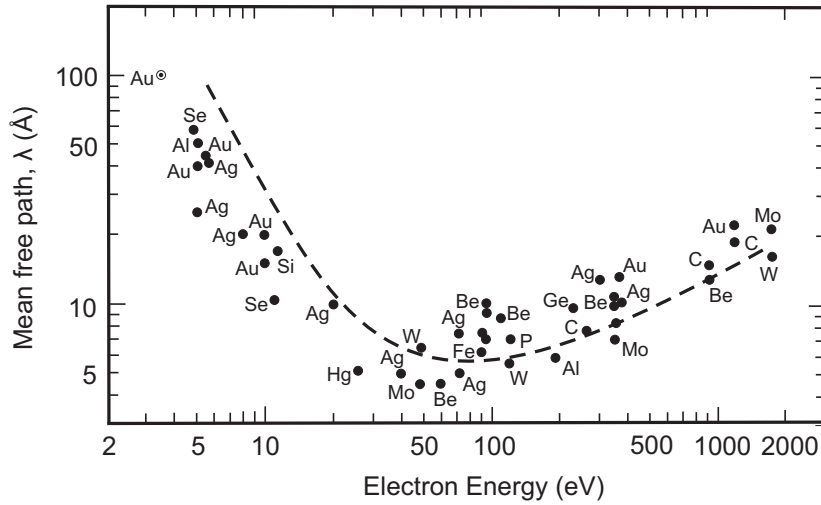

Figure 3.3: *Universal curve of inelastic mean free path of electrons as a function of kinetic energy in the solid. Dotted line represent the theoretical estimation. Adapted from ref. [82].* © *1979, Heyden and Son Ltd.*

For our measurements presented in this thesis has been performed in a low energy ultra violet (UV) UE112 beamline of BESSY II in the energy range of 15-110 eV.

(iii) Transmission Through Sample Surface and Angle Resolution

A refraction effect occurs when the electron passes through the sample surface due to the potential change at the surface. The momentum vector of the electron **k** inside the crystal can be expressed as $k^{\text{int}} = k_{||}^{\text{int}} + k_{\perp}^{\text{int}}$ where $k_{||}^{\text{int}}$ and $k_{\perp}^{\text{int}}$ are parallel and perpendicular component of the momentum to the surface, respectively. When the electron escapes from the surface, the parallel component of the electron momentum is conserved.

Thus

$$k_{||}^{\text{int}} = k_{||}^{\text{ext}} \pm G \qquad (3.8)$$

where *int* and *ext* denote the inner and outer wave vector respectively. Photoemission processes, where the addition of the reciprocal lattice vector, that is not perpendicular to the sample surface, is involved, are called *umklapp processes* which give rise to extra final state bands. Neglecting the umklapp processes, $k_{||}^{\text{int}}$ can be calculated when kinetic energy and
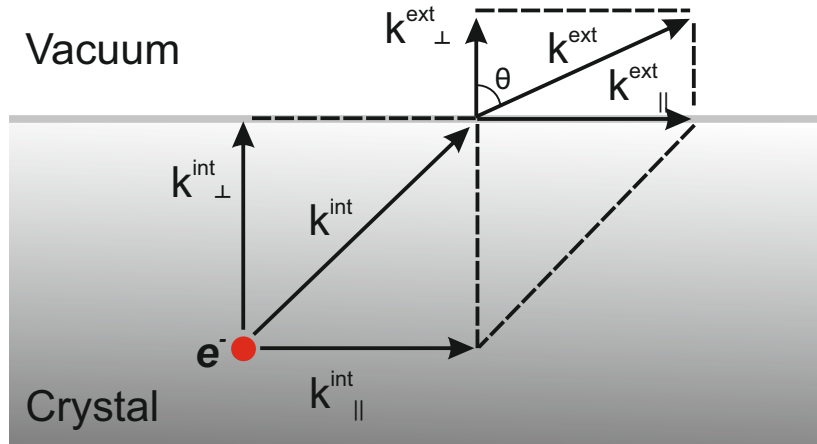
Figure 3.4: *Photoemission refraction of the electron while escaping from the sample surface because of the broken translational symmetry perpendicular to the sample surface. Parallel component of the momentum is conserved and this determines the angular resolution in the experiments.*

angle of photoemission are known.

$$k_{\parallel}^{\mathbf{int}} = \sqrt{\frac{2m}{\hbar^2} E_{\mathbf{kin}}} \sin \theta \tag{3.9}$$

The perpendicular component can be obtained if one assumes free-electron like final states, which offset from the vacuum potential by the inner potential V_0 [83]. Thus

$$k_{\perp}^{\mathrm{int}} = \sqrt{\frac{2m}{\hbar^2}(E_{\mathrm{kin}} + \Phi_0 - V_0)} \cos \theta \tag{3.10}$$

V_0 is a priori not known but can be estimated experimentally by locating the extremal points in the band dispersions. The inner potential is a phenomenological parameter and has to be adjusted for a given material. It is possible to determine the perpendicular component of the wave vector by systematically collecting the photoemitted electrons along normal emission and measuring their kinetic energy by varying the photon energy $h\nu$ of the excitation source.

These formulas provide the basis for determining the electronic band structure using Angle Resolved Photoemission Spectroscopy (**ARPES**). However photoemission spectra need further consideration of matrix elements effect, final state broadening etc. We will briefly describe these in the following sections.

3.2   Many Body Aspects

In the previous section we have explained photoemission using a single electron picture but in reality we are dealing with N number of electrons. In the photoemission process the

system relaxes and determining the final state is no longer trivial. Photoelectrons with high enough kinetic energy can be described in a simplified way with the *sudden approximation* which is used to calculate the photoemission spectra of highly correlated systems [84,85]. In this case we assume that an electron is instantaneously removed and the effective potential of the system changes discontinuously at that instant, i.e suddenly. On the other hand, electrons with low kinetic energy cannot be treated in this way and the *adiabatic limit* has to be considered. For our present study we assume the sudden approximation scenario so the wave function in Eq. 3.5 can be factorized between the photo-excited electron and $(N-1)$ electron terms given as [84]:

$$\Psi_f^N = \mathcal{A}\phi_f^{\mathbf{k}}\Psi_f^{N-1} \tag{3.11}$$

where $\mathcal{A}$ is the antisymmetric function satisfying the Pauli principle for the N electron wave function. $\phi_f^{\mathbf{k}}$ is the wave function with momentum $\mathbf{k}$ and Ψ_f^{N-1} is the final state wave funtion of $(N-1)$ electrons left behind. We can choose this state as an excited state with eigenfunction Ψ_m^{N-1} and energy E_m^{N-1} so that the total transition probability is then given by the sum over all possible excited states m. If we can assume the initial state as a single Slater determinant, it can be written as

$$\Psi_i^N = \mathcal{A}\phi_i^{\mathbf{k}}\Psi_i^{N-1} \tag{3.12}$$

However Ψ_i^{N-1} is not an eigenstate of the $(N-1)$ particle Hamiltonian, but is just what remains of the $N-$particle wave function after having pulled out one electron. It can be expressed in general as $\Psi_i^{N-1} = C_{\mathbf{k}\Psi_i^N}$. The matrix element can be written as:

$$\left\langle \Psi_f^N \left| H_{int} \right| \Psi_i^N \right\rangle = \left\langle \phi_f^{\mathbf{k}} \left| H_{int} \right| \phi_i^{\mathbf{k}} \right\rangle \left\langle \Psi_m^{N-1} | \Psi_i^{N-1} \right\rangle \tag{3.13}$$

where $\left\langle \phi_f^{\mathbf{k}} \left| H_{int} \right| \phi_i^{\mathbf{k}} \right\rangle \equiv M_{f,i}^{\mathbf{k}}$ is the one electron dipole matrix element. Now the total photocurrent is proportional to

$$\sum |M_{f,i}^k|^2 \sum |c_{m,i}|^2 \delta(E_{kin} + E_m^{N-1} - E_i^N - h\nu) \tag{3.14}$$

If only one final state is possible for the $(N-1)$ particle system then Eq. 3.14 resembles again Eq. 3.3.

To discuss to the photoemission intensity of the correlated system, most frequently the Greens function formalism approach has been followed. The photoemission spectral function can be written as the imaginary part of the Greens function $A(\mathbf{k},E) = \frac{1}{\pi}\Im(G(\mathbf{k},E))$. The electron correlation can be expressed in terms of a complex self energy function $\Sigma_i(\mathbf{k},E) = \Re\Sigma(\mathbf{k},E) + i\Im\Sigma(\mathbf{k},E)$ [77,86]. Real and imaginary part contain all the information on the energy renormalization and lifetime broadening, respectively. The Greens and spectral func-

tions expressed in terms of the self energy are then given by

$$G(\mathbf{k}, E) = \frac{1}{E - E_\mathbf{k} - \Sigma(\mathbf{k}, E)} \tag{3.15}$$

$$A(\mathbf{k}, E) = \frac{1}{\pi} \frac{\Im\Sigma(\mathbf{k}, E)}{[E - E_i(\mathbf{k}) - \Re\Sigma(\mathbf{k}, E)]^2 + [\Im\Sigma(\mathbf{k}, E)]^2} \tag{3.16}$$

3.3   Symmetry and Selection Rules

Photoemission intensity in the ARPES experiment is mostly affected by matrix element effects, finite experimental resolution and extrinsic background due to the secondary electrons. Matrix element effects are responsible for the dependence of photoemission intensity on photon energy and experimental geometry and may even result in the complete suppression of the intensity [84, 87, 88]. By considering special experimental geometries, selection rules for the observability of particular initial states $|\psi_i\rangle$ can be derived. If we assume a mirror plane containing the direction of the incident photon and the detector perpendicular to the crystal surface, we can determine whether the initial electronic state is even or odd with respect to reflection in the mirror plane. The matrix element in Eq. 3.13 should be symmetric with respect to the mirror plane and thus the final state wave function must always be even, otherwise the detector located in the mirror plane would see a node of the emitted electron wave function. Depending on the polarization of the incident light, the dipole operator $\vec{A} \cdot \vec{p}$ is even or odd with respect to the mirror plane and therefore the symmetry of the initial state can be determined. We can summarize the matrix elements as follows [84]:

$$\left\langle \phi_f^\mathbf{k} | \vec{A} \cdot \vec{p} | \phi_i^\mathbf{k} \right\rangle \begin{cases} \phi_i^\mathbf{k} & \text{even} & \langle + | + | + \rangle \Rightarrow \vec{A} & \text{even} \\ \phi_i^\mathbf{k} & \text{odd} & \langle + | - | - \rangle \Rightarrow \vec{A} & \text{odd} \end{cases} \tag{3.17}$$

3.4   Dimensionality: Bulk and Surface States

Angle resolved photoemission can also used to distinguish between bulk and surface electronic states. We can explore the band structure of a solid moving along different high symmetry direction in the Brillouin zone just by changing ϕ_e, θ and the incident photon energy hν. Now considering the normal emission ($k_\parallel = 0$) condition of the photo-excited electron, only changing the photon energy ($h\nu$) we can obtain the electronic band dispersion along the k_z direction of the bulk Brillouin zone as shown in Fig. 3.5. The Bloch wave function of the bulk state, surface state and surface resonances all are extended up to the surface region and confined by the surface potential barrier. Bulk states exist with periodically varying amplitude throughout the crystal, while true surface states are localized strictly at the surface and are periodic in only two dimensions. Surface resonances, on the other hand,

result from the mixing of surface and bulk state wave functions and exhibit an exponentially decaying amplitude in the direction into the solid. They are equivalent to bulk wave functions with an enlarged amplitude in the surface region of the crystal. True surface states (blue dashed lines inside the gaps), so-called Shockley [89] or Tamm [90] states, lie only inside the relative gaps and are characterized by energy levels that are not degenerate with bulk bands. Although there is no strict physical distinction between them, Shockley states can be theoretically derived from the nearly-free electron model and are more localized, in contrast to Tamm surface states which are more delocalized and related to tightly bound electrons, thus calculated in the framework of the tight-binding model [91]. A mixing between surface and bulk bands occurs if one of these surface states penetrates into a part of the surface Brillouin zone (SBZ) (blue dashed lines outside the gaps) where propagating bulk bands of the same symmetry exist, leading to surface resonances which as a result penetrate deep into the bulk.
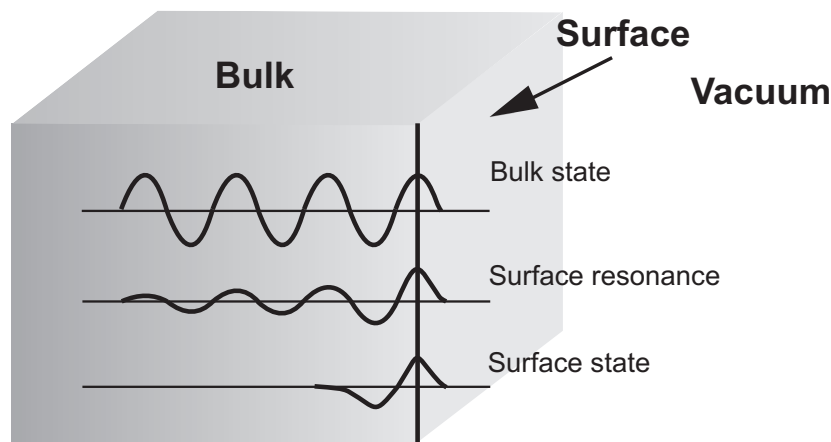

Figure 3.5: *Representation of bulk and surface states and surface resonance and the decaying wave-functions of these states.*

As we have discussed in Chapter 2, there exists another type of surface state, the so called topological surface state which differs from the conventional or trivial surface states. We show our measured topological surface states in the following result chapters 4, 5 and 6.

3.5   Instrumentation

We discussed in the previous section, photoemission techniques include a light source to create photo-electrons and suitable instruments to detect the photoemitted electrons with high accuracy in energy, and momentum. The resolution of the photoemission data depends on the experimental setup used for the measurements. We will briefly discuss the experimental set up and light source used to measure topological surface states.

3.5.1   Experimental Setup

ARPES 1^2 and 1^3 setup:

All of our measurements presented in this thesis have been performed in the ARPES stations 1^2 and 1^3 of undulator beamline UE112-PGM2 at the BESSY II synchrotron radiation source. The ARPES 1^2 end station is equipped with two chambers separated by a gate valve. The upper chamber is used to prepare and transfer clean surfaces for the ARPES experiments. The preparation chamber is equipped with several exchangeable ports for evaporators for deposition purposes. The samples are transferred to the ultra high vacuum chamber through a load lock. After preparing a clean sample surface by cleaving or decapping we go down to the bottom chamber i.e., analysis chamber, for the photoemission experiment. Typical pressures lie between 1×10^{-10} and 1×10^{-11} mbar. The ARPES 1^2 chamber is equipped with a six axes cryo-manipulator providing three rotational and three translational degrees of freedom for k space mapping. For low temperature measurements we can cool the sample to 20 K, and regulate the temperature with a LakeShore temperature controller using cryogenic temperature sensors. The analysis chamber is connected with the designated beamline and hosting an R8000 Scienta hemispherical electron analyzer. The radius between the inner (r_i) and the outer shell of the electron analyzer (r_o) is given by $r = (r_i + r_o)/2$ which is 200 mm. The pass energy E_P of the analyzer is defined by the potential difference between the inner and outer hemispheric shell (U_P) given as

$$E_P = \frac{eU_P}{r_2/r_1 - r_1/r_2}. \tag{3.18}$$

The electrons which pass through the electron analyzer are multiplied by a multi-channel plate and then reach a phosphor screen, monitored by a CCD camera. Real time images on the detector can be seen on a computer screen. This helps to optimize the sample position and analyzer parameters. The energy and angular resolution of the ARPES 1^2 are around 5 meV and 0.1°, respectively.

On the other hand the ARPES 1^3 experimental chamber was built to enable experiments that require the highest energy resolution at ultimately low sample temperatures. To achieve this goal, all contributions to the experimental broadening the resolution of both the excitation source and the electron energy analyzer as well as the sample temperature have been reduced to ≤ 1 meV or their equivalent, yielding the name of the station: 1 meV $\times$ 1 meV $\times$ 1 K = 1^3 [92, 93]

3.5.2   Light Source: Synchrotron radiation

The discovery of synchrotron radiation followed by the availability of next generation synchrotron light source has improved the photoemission technique by a great deal. Syn-

chrotron radiation is the name given to the radiation which occurs when charged particles are accelerated in a curved path or orbit. Electrons traveling at a speed close to the speed of light c and forced to change the direction of their motion under the effect of magnetic fields (perpendicular to the direction of their motion), emit a narrow cone of radiation with angular spread $\Delta\phi$. Synchrotron light source has great advantage over the lab based gas-discharge lamp. It offers highly intense and highly polarized photon beam of wide spectral range from the visible to the x-ray region. It has a precise time structure and the photons are highly collimated which enhances the overall angular resolution of the experiment. We have performed our ARPES experiments at the third generation synchrotron light source BESSY II in Berlin. Electrons ejected from an electron gun are first accelerated through a linear accelerator (LINAC) and then they are sent to a circular accelerator which is typically known as booster synchrotron where they obtain the final kinetic energy of 1.7 GeV. After that these high energy electrons are injected into the large storage ring where they circulate for many hours with constant energy in an ultra high vacuum environment. The storage ring is composed of bending magnets and insertion devices (IDs). IDs are mainly wigglers and undulators which are composed of alternating magnet arrays. When the circulating electrons pass through these devices they emit photons of different energy which are then directed along the beamline. A schematic of the BESSY-II synchrotron radiation centre is shown in Fig. 3.7. The energy of the particle moving with velocity v is given by

$$E = \gamma m_0 c^2 \tag{3.19}$$

where $\gamma = \frac{1}{\sqrt{1-\frac{v^2}{c^2}}}$, the opening angle of the radiation is $\Delta\phi \cong \gamma^{-1}$ [94]. The higher the value of γ the more collimated the beam would be. The spectral range of photons produced by electrons following a path with a radius of curvature R_b can be characterized with the critical energy given by

$$E_c = \frac{3c\gamma^3}{2R_b} \tag{3.20}$$

E_c is defined in terms of the spectral power radiated by relativistic particles. We can obtain a monochoromatic photon beam by placing a monochromator tangential to the circular orbit [95, 96].

The setup is connected to the PGM2a branch of the UE112 beamline which is an undulator beamline designed for ultimate energy resolution in the VUV-XUV regime (15-200 eV). The APPLE II type undulator has a period length of 112 mm and a minimal gap of 22.2 mm. The difference of the APPLE II to a standard planar undulator is that the bottom and top magnet rows are separated horizontally into two parts that can be shifted relative to each other. In addition to linearly polarized light these undulators are capable of producing elliptically and circularly polarized light.
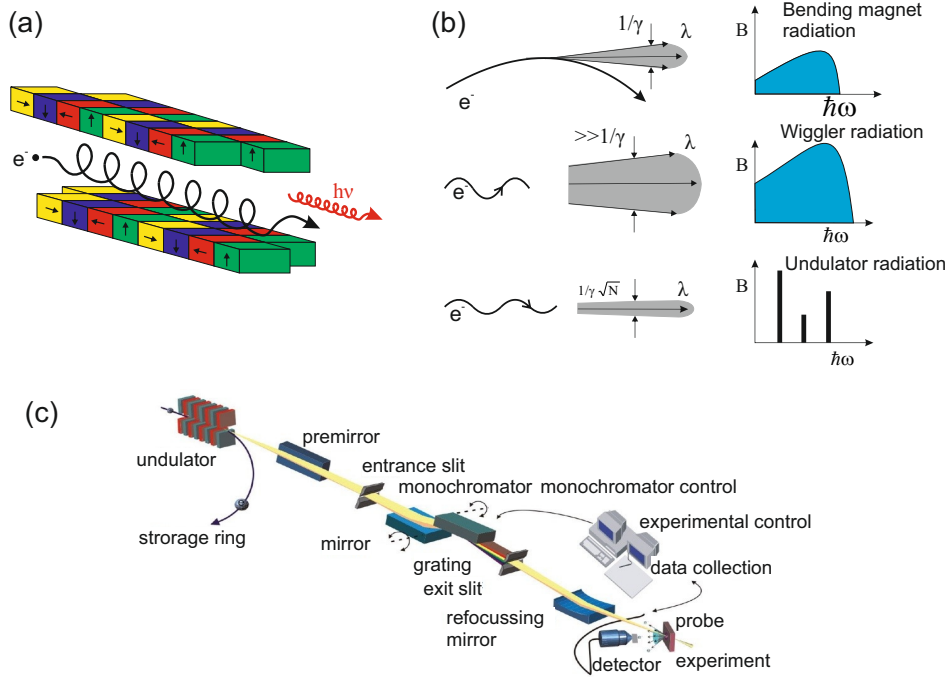
(a)

(b)

1/γ   λ

e⁻

Bending magnet radiation

B

$\hbar\omega$

>>1/γ   λ

e⁻

Wiggler radiation

B

$\hbar\omega$

1/γ √N   λ

e⁻

Undulator radiation

B

$\hbar\omega$

hν

(c)

undulator

premirror

storrage ring

mirror

entrance slit

monochromator   monochromator control

experimental control

grating

exit slit

refocussing mirror

data collection

probe

detector   experiment

Figure 3.6: *(a) Schematic of an undulator. By varying the longitudinal and lateral distance between the top and bottom magnets we can produce different light polarization. (b) Comparison of the emssion angle for bending magnet, wiggler and undulator. (c) Schematic of a typical beamline at BESSY-II.*

3.5.3   Sample Preparation for ARPES

Epitaxial growth of (111) $Pb_{1-x}Sn_x$Se (Te) films on BaF_2 substrates was performed by our collaborator from JKU, Linz using molecular beam epitaxy in ultra-high vacuum (UHV) conditions better than 5×10^{-10} mbar. Effusion cells filled with stoichiometric PbSe and SnSe were used as source materials, as well as a ternary $Pb_{1-x}Sn_x$Se source with different Sn concentration. Bi-doping was realized using a compound BiSe effusion cell. The chemical composition of the layers was varied over a wide range from $x_{Sn} = 0$ to 40% by control of the SnSe/PbSe beam flux ratio that was measured precisely using a quartz microbalance moved into the substrate position. The growth rates were around 1 μm/h ($\sim$ 1 monolayer/s) and the growth temperature set to 380°C as checked by an infrared pyrometer. The film thickness was in the range of 1–3 μm. For all layers smooth 2D growth occurs after few nanometer deposition on BaF_2 (111) as revealed by reflection high-energy electron diffraction (RHEED) patterns recorded in-situ during MBE growth for films with various Sn compositions. The high quality of the layer is evidenced by sharp diffraction spots on the Laue semicircle and intense Kikuchi lines arising from diffraction from bulk lattice planes. No surface reconstruction is observed during deposition. The epitaxial films were capped in situ after MBE growth with a 200 nm thick amorphous Se layer at room temperature to protect the surface against oxidation during transport to BESSY II, where the Se cap was completely desorbed in the preparation
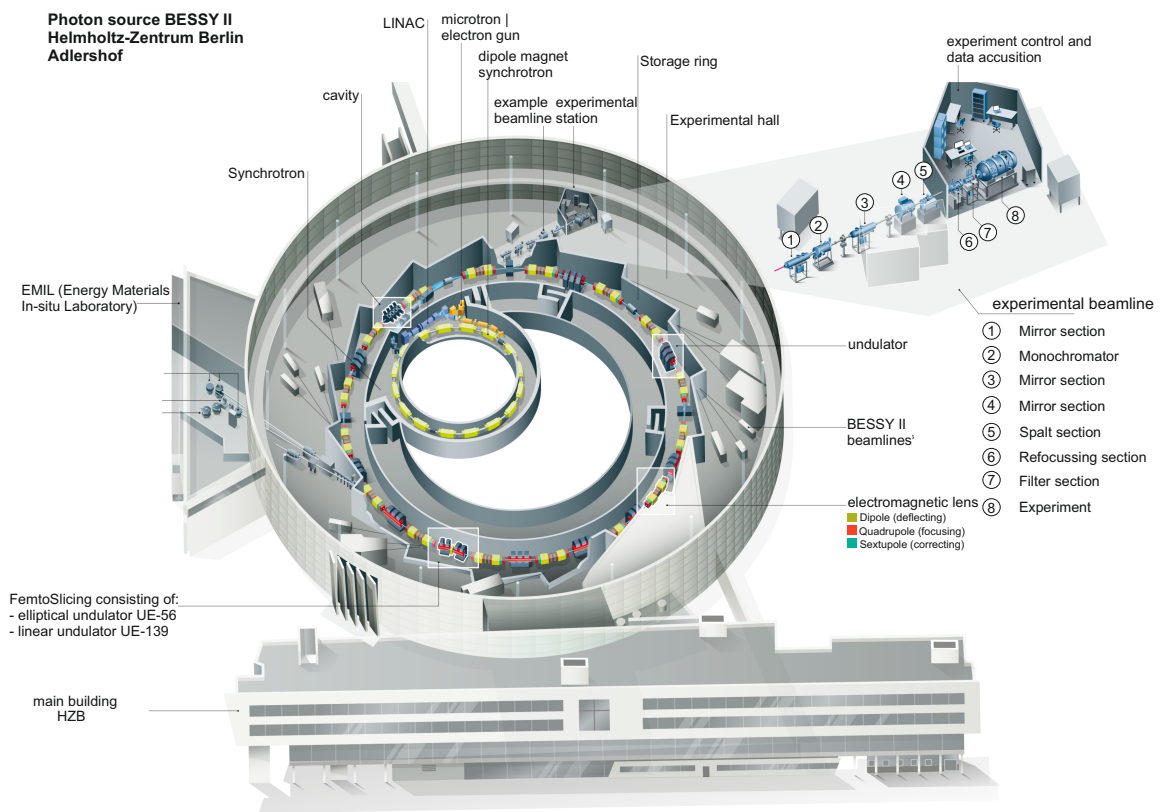
Figure 3.7: *Schematic of the electron storage ring at BESSY II (©:HZB/Ela Strickert)*

chamber by annealing at about 230°C for 15 min in 3×10^{-10} mbar vacuum.

Mn-doped Bi_2Te_3, Bi_2Se_3 layers were grown by molecular beam epitaxy (MBE) on BaF_2 (111) substrates using a Riber 1000 and a Varian GEN II MBE system. Compound Bi_2Te_3, Bi_2Se_3 as well as elemental sources for Mn, Te and Se were used for control of stoichiometry and composition. Deposition was carried out at a growth temperature of 330°C for Bi_2Te_3 and 360°C for Bi_2Se_3 to obtain perfect two-dimensional growth independently of dopant concentrations. Immediately after growth, samples used for ARPES were capped in situ with amorphous Se and Te capping layers at room temperature to protect the surface against oxidation. This cap was removed just before the ARPES experiments by in-situ sputtering and annealing at ARPES-1[3] experimental station.

Chapter 4

Topological Crystalline Insulator Phase in $Pb_{1-x}Sn_xSe$

We have seen earlier that the topological classification is given by the so-called $\mathbb{Z}_2$ invariant (ν_0). An odd number of Dirac cones $\nu_0=1$, corresponds to a strong ($\mathbb{Z}_2$) topological insulators, while an even number of cones $\nu_0=0$, characterize a weak topological or trivial insulators [97,98]. However, it is also possible to transform a $\mathbb{Z}_2$ topological insulator into a trivial insulator by alloying which has been observed in Bi_2Se_3:In [99,100], and $BiTl(S_{1-x}Se_x)_2$ [101]. The topological phase transition is characterized by the bulk band gap closing, and subsequent appearance of a surface state, determined by the bulk-boundary correspondence. In this picture, the crystal symmetry is maintained supposedly through the complete phase transition. We have seen in the section 2.4.1, the crystal symmetry itself can protect topologically distinct phases known as topological crystalline insulators (TCIs) [37, 44, 45, 97, 102, 103], where the topological protection depends on the specific crystal face [37]. Although the topological invariants allow for an even number of Dirac cones in such cases, they are not robust against disorder [97]. $Pb_{1-x}Sn_xSe$ and $Pb_{1-x}Sn_xTe$ represent such mirror-symmetry protected TCIs with four-fold valley degeneracy [45,97] in which the trivial-to-TCI phase transition is reached for sufficiently large Sn contents and upon cooling [37, 104]. The underlying mechanism is due to the lattice contraction and subsequent enhanced orbital overlap which leads to an inverted (i.e., negative) bulk band gap which, via bulk-boundary correspondence, gives rise to the topologically protected surface states. This phase has been experimentally observed in $Pb_{1-x}Sn_xSe$ protected by the mirror symmetry of the crystal along the [110] direction in the bulk Brillouin zone of the FCC crystals. The first theoretical prediction of topological crystalline insulator was made by Liang Fu in 2011 [37] and since then many studies have been conducted on this topic. Hsieh et al. were the first to predict the topological nature in the SnTe system using first principles band structure calculations [45]. Subsequently a detailed calculation of the surface states and their spin texture was done by Safaei et al. [105]. First

experimental evidence of a topological crystalline insulator was shown on a p-type cleaved (110) SnTe by Tanaka et al. [102] and later with the $Pb_{1-x}Sn_xTe$ single crystals by Xu et al. [103]. However, they show only the bulk valence band, and there was no information available about the gap or the Dirac cone. The temperature-driven topological phase transition from a trivial insulator to a TCI on the $Pb_{1-x}Sn_xSe$ (110) surface was nicely shown in ARPES measurements by Dziawa et al. [104]. On the other hand, there are crystals which are not necessarily topological but change their symmetry and their electronic properties with temperature. Such phase change materials have been studied intensively for non-volatile data storage because their properties can be altered dramatically at the structural phase transition [106]. GeTe is such a prototypical material [106, 107] which transforms upon cooling from the cubic rock salt to a rhombohedral structure characterized by a large relative sublattice displacement. This gives rise to pronounced ferroelectricity in GeTe [108], has recently been found to allow for an electrical switching of the electronic properties [109]. Symmetry changes are potentially very interesting also for topological insulators. In fact, it has been shown for the TCI $Pb_{1-x}Sn_xSe$ that by breaking of mirror symmetries two out of the four Dirac cones at its (100) surface can be gapped [45, 110–112]. In that case, the topological phase remains, however, unchanged by the symmetry breaking and the $\mathbb{Z}_2$ invariant stays even. For our present work, it is crucial to note that the topological phase does not need to be preserved by a distortion in principle. In fact, topological phase transitions have recently been predicted for two-dimensional TlSe, where the topological phase transition between 2D TCI and 2D TI is mediated by uniaxial strain [113]. Another theoretical study reveals that the three-dimensional SnTe goes from TCI phase to $\mathbb{Z}_2$ TI phase and ultimately to a ferroelectric Rashba semiconductor phase with its structural changes from room temperature cubic phase to low-temperature ferroelectric phase induced by ferroelectric distortions [114]. Safaei et al. predicted that the quantum spin Hall effect could be observed in (111)-oriented thin films of SnSe and SnTe TCI as well, where the transition from the trivial to a 2D TI phase is obtained by tuning the thickness of the films [115].

In this chapter, we will present our ARPES studies of $Pb_{1-x}Sn_xSe$ epilayers on the (111) surface which follows our already published results in Nature Communication journal [1] [116]. We show systematically the temperature dependent trivial to TCI phase transition of the $Pb_{1-x}Sn_xSe$ samples with three different Sn concentration namely, 10%, 20% and 28%. Furthermore, we also demonstrate an atypical quantum phase transition from TCI phase to $\mathbb{Z}_2$ TI phase in $Pb_{1-x}Sn_xSe$ (111) epilayers with Bi-doping. We show the existence of a gapped topological surface state at the $\overline{\Gamma}$ point induced by Bi-doping, while the other three Dirac

cones at the $\overline{M}$ point of the surface Brillouin zone (SBZ) remain intact, which results in an odd number of Dirac cones in the SBZ. This is because Bi contributes to the structural symmetry breaking from cubic to rhombohedral distortion, and triggers the novel TCI-to-$\mathbb{Z}_2$ topological phase transition. This has the implication of an extended topological phase diagram, and switching between a strong and weak topological insulator by lattice distortions or by an applied electric field becomes possible.

4.1 Observation of TCI Phase in Pb$_{1-x}$Sn$_x$Se

We investigate the band topology of the (111) surface of Pb$_{1-x}$Sn$_x$Se by cooling through the complete trivial to topological phase transition. At first we briefly discuss the sample growth, followed by the ARPES measurements of undoped Pb$_{1-x}$Sn$_x$Se samples with different Sn concentrations.

4.1.1 Sample Growth and Structural Characterization

Epitaxial growth of (111) Pb$_{1-x}$Sn$_x$Se films on BaF$_2$ substrates were performed by our collaborators at Johannes Kepler University in Linz using molecular beam epitaxy (MBE) in ultrahigh vacuum conditions better than 5×10^{-10} mbar. The composition of the layers determined from the beam flux ratio agrees within $\pm 2\%$ to the composition determined independently by x-ray diffraction which is described in appendix A. The growth rates were kept around 1 μm/h ($\sim$1 monolayer/s), and the growth temperature was set to 380°C as checked by an infrared pyrometer. The film thickness was in the range of 1-3 μm. For all
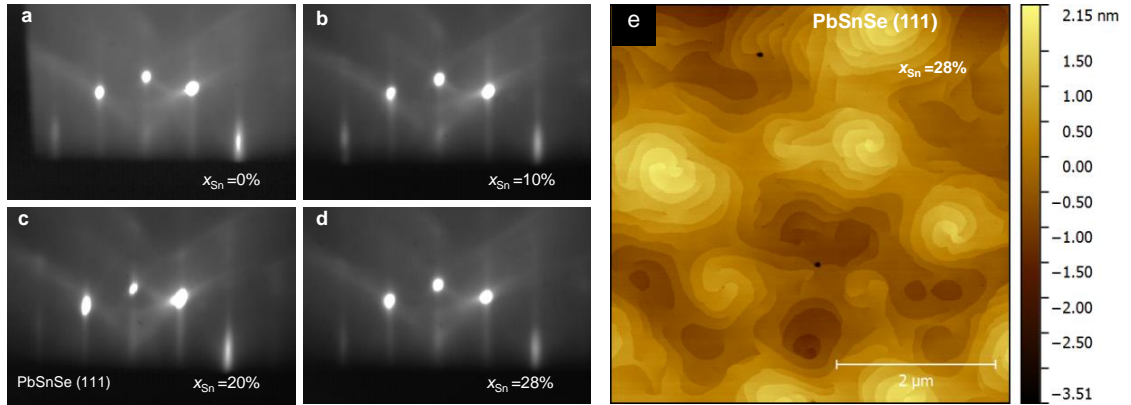

Figure 4.1: *Growth and Surface Characterization: (a)-(d) Reflection high-energy electron diffraction of Pb$_{1-x}$Sn$_x$Se epilayers on BaF$_2$ (111) substrates recorded during MBE growth for $x_{Sn} = 0, 10, 20$ and 28%, respectively. (e) Atomic force microscopy image of the $x_{Sn} = 28\%$ epilayer with 1 μm thickness. The different heights are described by the color scale bar shown on the right.*

layers smooth 2D growth occurs after few nanometer deposition on BaF$_2$ (111) as evidenced by

Fig. 4.1(a-d) which present the reflection high-energy electron diffraction (RHEED) patterns recorded *in-situ* during MBE growth for films with various Sn compositions. The high quality of the layers is evidenced by sharp diffraction spots on the Laue circle and intense Kikuchi lines arising from diffraction from the subsurface bulk lattice planes. No surface reconstruction was observed during deposition. The surface of the films is atomically flat, exhibiting only single monolayer steps of 3.52 Å height as exemplified by the atomic force microscopy (AFM) image presented in Fig. 4.1(e) for $x_{Sn} = 28\%$. At the given growth temperature, growth proceeds in a 2D step-flow mode, and the spiral step structure shown Fig. 4.1 (e) is mainly due to the pinning of the surface step at screw type threading dislocation, which originates from the lattice mismatch $\Delta a/a \sim 1.6\%$ $Pb_{1-x}Sn_xSe/BaF_2$ (111) of the film and the substrate [117].

4.1.2 Temperature and Sn Concentration Dependent Band Inversion of Undoped $Pb_{1-x}Sn_xSe$

We have collected the corresponding valence band ARPES data in a wide range of temperatures between 300 and 30 K using linearly-polarized $(p + s)$ light with photon energies ranging from 18 to 23 eV. The ARPES dispersions around the $\overline{\Gamma}$ and $\overline{M}$ points were acquired using the photon beam geometry shown in Fig. 4.2(a), where the light incidents on the sample under an angle of $\phi = 45°$ with respect to the surface normal. The light incidence, and electron detection planes were parallel to the $\overline{M}$ -$\overline{\Gamma}$ -$\overline{M}$ and $\overline{K}$ -$\overline{\Gamma}$ -$\overline{K}$ high symmetry directions of the surface Brillouin zone, respectively. The corresponding energy and angular resolutions of our ARPES analyzer were set to 5 meV and 0.1°, respectively. The bulk and (111) surface Brillouin zone of the rock salt $Pb_{1-x}Sn_xSe$ are shown in Fig. 4.2 (a). Fig. 4.2 (b) reproduces the SBZ overlaid on a Fermi surface map.

In contrast to the natural (100) cleavage plane of bulk crystals previously studied [102–104, 118], for the (111) orientation the four bulk L-points project on the following four time-reversal invariant surface momenta: $\overline{\Gamma}$ and three equivalent $\overline{M}$ points [119]. This is observed in the ARPES data shown in Fig. 4.2(b), where the intensity from the Dirac cones at the three $\overline{M}$ points is suppressed by the photoemission final-state effect similar to the case of graphene where part of the experimental Fermi surface is suppressed due to the interference of photoelectrons emitted from the two equivalent carbon atoms per unit cell of its honeycomb lattice [120]. Due to the sensitive dependence of the bulk band inversion on the lattice constant, the trivial to topological phase transition can be monitored during cooling by tracing the evolution of the bulk band gap [121] or by observation of the appearance of the gapless Dirac cones in ARPES measurements [104, 118].

Indeed, for (111) films with low Sn concentrations and without Bi doping ($x_{Sn} = 10\%$), the Dirac cone at the $\overline{\Gamma}$ point does not form down to 22 K as shown in Fig. 4.3(a-d). We have estimated the bulk band gap in the measured temperature range shown in Fig. 4.3(e). Bulk
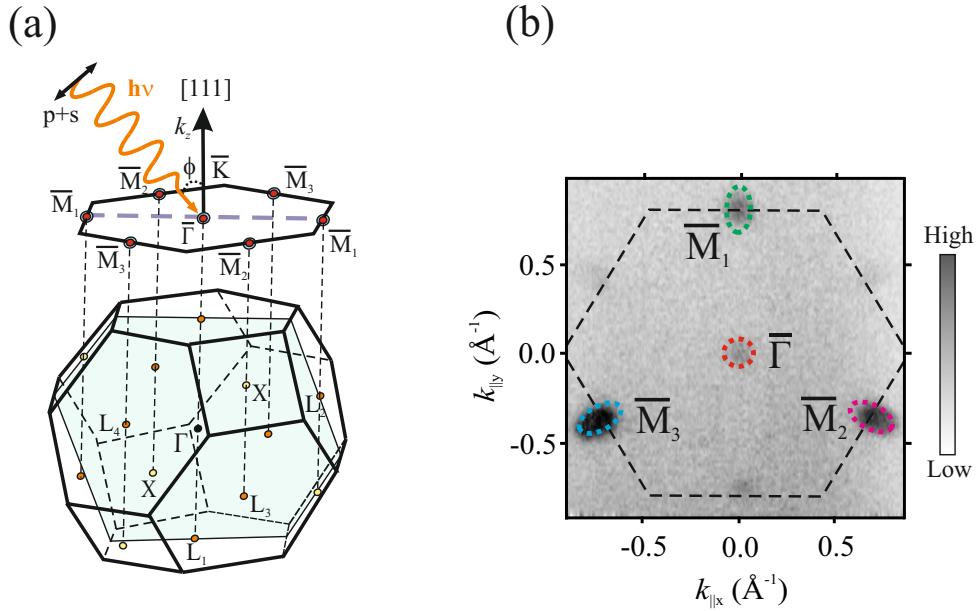
(a)

(b)

Figure 4.2: *(a) For (111) films the four bulk L-points of the bulk Brillouin zone project onto the surface $\overline{\Gamma}$ -point for the longitudinal L–valley along [111], whereas the three oblique valleys project on the $\overline{M}$ points. (b) Fermi surface map represent the bulk band inversion and subsequent appearance of the Dirac cone occurs at the $\overline{\Gamma}$ and three $\overline{M}$ point, makes it an even number of band inversion which is the signature of a TCI.*

band gap starts with around 180 meV at room temperature, and then it starts to decrease as we cool down the sample, finally reaches 60 meV at 22 K, which was the lowest temperature achievable for the current experimental setup. This represent the topologically trivial state for the $Pb_{1-x}Sn_xSe$ sample with $x_{Sn} = 10\%$.

As we increase the Sn concentration to 20% in the $Pb_{1-x}Sn_xSe$ system, we observe the bulk band gap closing at around 90 K and subsequently the gapless Dirac cones appear. Temperature dependence band inversion for 20% have shown in Fig. 4.4(a–d). As we further cool down the sample to 40 K we expect further increase of the bulk band gap, but the system is already in the TCI phase, depicted by a high photoemission intensity of the Dirac type topological surface state. We have traced the evolution of the bulk band gap for each temperature which are plotted in Fig. 4.4(e). The surface band gap (red squares) with the bulk band gap (blue line) from optical data [119], evidencing that the surface gap closes when the bulk band gap changes sign. The error bars in the measured surface band gap correspond to the uncertainty of determining the energy position of the band dispersions.

As we further extend our measurement with $x_{Sn} = 28\%$, we observe that the gapless Dirac cone appears even at higher temperature at 130 K, compared to the sample with 20% Sn concentration. The corresponding ARPES band dispersions are shown in Fig. 4.5(a-d), and the respective surface band gaps plotted in Fig. 4.5(e).
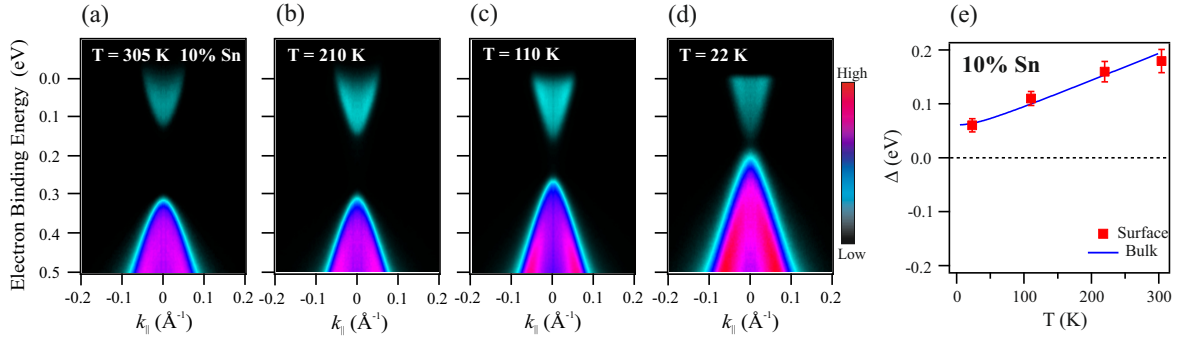
Figure 4.3: *(a)−(d) ARPES data measured at 18 eV photon energy as a function of temperature. (b) The x_{Sn} = 10% sample remains trivial down to low temperature as seen from the persistence of a band gap.*
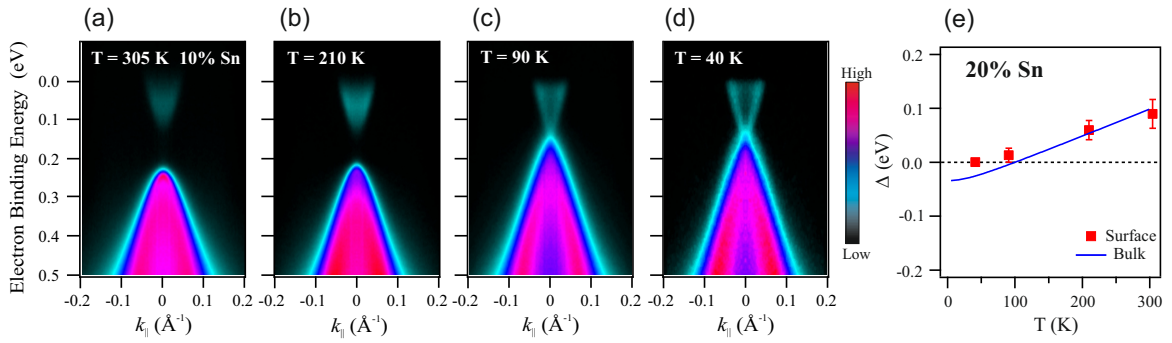

Figure 4.4: *(a)−(d)Temperature dependence ARPES measurements of 20% Sn concentration samples. The bulk band closes around 90 K. (e) Corresponding surface band gap vs the temperature.*
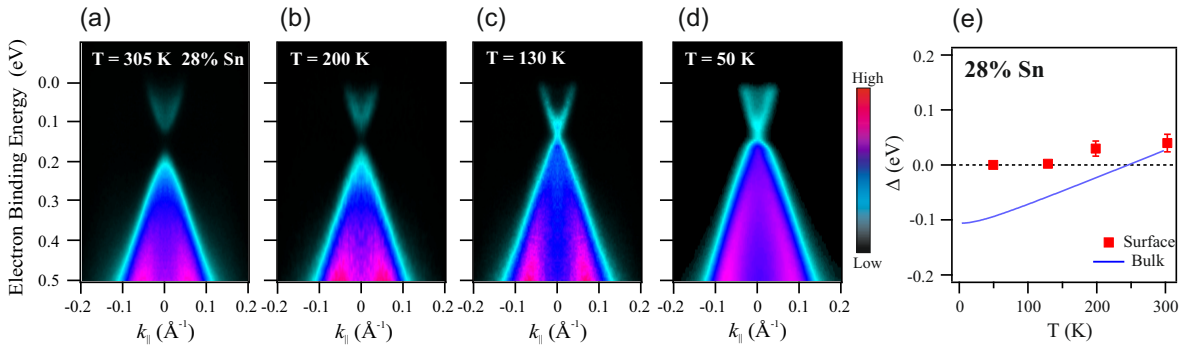

Figure 4.5: *(a)−(d) ARPES measurements of Pb$_{1-x}$Sn$_x$Se with X_{Sn} = 28% and appearance of gapless Dirac cones at 130 K due to the bulk band gap inversion. (e) Variation of the surface band gap with temperature.*

We will further discuss our method of determining the size of the band gaps in terms of fitted energy-distribution curves (EDCs) at the zero momentum derived from the ARPES measurements in the next section.

4.2   Gapped Surface State in the Topological Phase: Influence of Bi Doping

As we have described in the last section undoped Pb$_{1-x}$Sn$_x$Se exhibits a p-type background carrier concentration due to cation (Pb/Sn) vacancies formed during growth. These cation vacancies form resonant acceptor like energy levels and thus induce a p-type hole conductivity [122]. The p-type carrier concentration increases with increasing Sn content from around 10^{17} cm^{-3} for PbSe to above 10^{18} cm^{-3} for x$_{Sn} > 30\%$ [116]. Incorporating Bi gives rise to n-type doping and allows tuning the Fermi level into the conduction band. This is required for studying the properties of the entire Dirac cones of the topological surface states by ARPES. Here we use a Bi$_2$Se$_3$ effusion cell for doping, which promotes substitutional incorporation of Bi on cation lattice sites without the need of an additional Se flux. The solubility of Bi in PbSe and SnSe amounts to several percent according to the quasi binary phase diagrams [117], for n-doping only a small Bi$_2$Se$_3$ flux in the range of 10^{-5}-10^{-2} ML/s (ML= mono-layer) range is required, depending on the desired doping level. This doping flux was calibrated as described in detail in Ref. [122], where the unity doping efficiency was achieved for Bi concentrations up to 5×10^{19} cm^{-3}, above which the doping coefficient slowly decreases and eventually causes a rapid structural degradation of the layers. However, incorporating Bi into Pb$_{1-x}$Sn$_x$Se system has significant consequences as observed in our ARPES measurements shown in the following section.

Here we discuss a new type of phase transition from crystal-symmetry protected to time-reversal symmetry protected topology controlled by Bi doping in Pb$_{1-x}$Sn$_x$Se. We have observed that when Bi is introduced in the bulk, a gap opened up at the Dirac cone at $\overline{\Gamma}$, located at the center of the surface Brillouin zone. Nevertheless, the other three Dirac cones located at the $\overline{M}$ points at the zone boundaries behave as in pure Pb$_{1-x}$Sn$_x$Se, i.e., are gapless at low temperature. More interestingly, we can demonstrate the 2D nature of the gapped state at $\overline{\Gamma}$ as a signature of the surface state. This will be followed by a systematic comparison of Bi doping in Pb$_{1-x}$Sn$_x$Se system with Sn concentration within the trivial side. We then represent our detailed investigation of the Dirac cones at $\overline{\Gamma}$ and $\overline{M}$ point of the Pb$_{1-x}$Sn$_x$Se with x$_{Sn}$ =28% where the trivial to TCI phase transition is easily achieved by cooling the sample. These findings provide the significant experimental evidence for a topological phase transition from a TCI with an even number of Dirac cones to a time-reversal-symmetry protected strong $\mathbb{Z}_2$ topological insulator with odd (three) number of Dirac cones.

Following the recent prediction by Plekhanov et al. [114], the origin of the novel topological phase transition is interpreted as due to a sublattice shift and rhombohedral distortion along the [111] direction, which lifts the bulk band inversion only at the Z-point (L-point in the undistorted phase) projected onto $\overline{\Gamma}$. At the same time, we do not find any evidence for a bulk band gap closing across the phase transition, most likely, because the rhombohedral distortion does not leave the system in the same symmetry class where the TCI is defined.
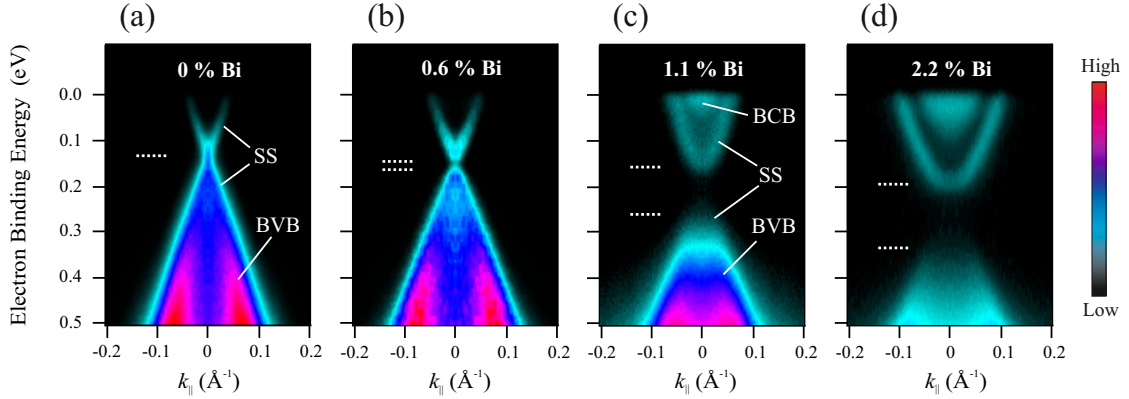

Figure 4.6: *Doping effect and gap opening at $\overline{\Gamma}$ induced by Bi. (a)–(d) Incorporation of Bi in $Pb_{0.72}Sn_{0.28}Se$ (111) films leads to n-type doping and a gap opening at the $\overline{\Gamma}$ point as revealed by ARPES data measured at a temperature of 30 K and 18 eV photon energy. Most notably, the appearance of the bulk conduction band is observed for Bi doing $\geq$ 1.1%.*

Figure 4.6 shows the effect of bulk Bi doping on the $\overline{\Gamma}$ Dirac cone of $Pb_{0.72}Sn_{0.28}Se$. When substitutionally incorporated at cation (Pb, Sn – group IV) lattice sites, the group V element Bi acts as electron donor due to its excess valence electron [123]. Increasing the Bi concentration n_{Bi} thus leads to a strong upward shift of the Fermi level by 200 meV for $n_{Bi} = 2.2\%$ shown in Figs. 4.6(d). Remarkably, we have observed an intact Dirac cone for undoped $Pb_{0.72}Sn_{0.28}Se$ at 30 K, but as we start incorporating Bi, a surface gap opens up at the $\overline{\Gamma}$ Dirac cone. We have estimated the gap size as as large as ~100 meV for the sample with 2.2% Bi-doping. Our particular choice of our photon energy of 18 eV helps us to nicely trace the bulk conduction band, and parabolic shape of the gapped Dirac cone as shown in Fig. 4.6 (c), and (d). Estimated gap sizes for different temperature and different doping level of Bi are shown in Fig. 4.7. We observe that the surface energy gap increases strongly with increasing Bi content as shown in Fig. 4.7(b). This leads to our general conclusion that for Bi doping $>\sim 0.6\%$ the band gap at $\overline{\Gamma}$ does not close at the lowest temperature.

Determination of the surface band gap: It is essential at this point to discuss our methodology of determining the surface band gap. Here we summarize the procedure used by taking an example of the $Pb_{0.72}Sn_{0.28}Se$ sample doped with 0.6% Bi. We have fitted the
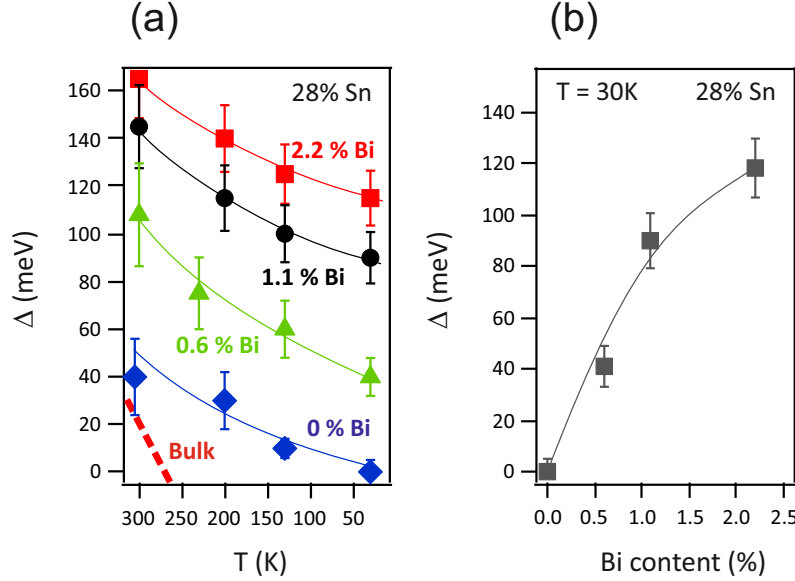
Figure 4.7: *(a) Dependence of the surface band gap (Δ) with temperature. The error bars in Δ correspond to the uncertainty of determining the energy position of the band dispersions. (b) Increase of the band gap as a function of Bi doping for $Pb_{0.72}Sn_{0.28}Se$.*

experimental energy-distribution curve (EDC) at zero momentum extracted from the ARPES data. Fig. 4.8(a) shows the corresponding energy-momentum ARPES dispersion measured at 30 K with 18 eV photon energy. The intensity contributions from the bulk-valence band (BVB) states at high binding energies are clearly distinguishable from the dispersion of the upper and lower part of the surface state (SS) at lower binding energies. In particular, we observe that in contrast to the undoped $Pb_{0.72}Sn_{0.28}Se$ sample measured under the same experimental conditions as shown in Fig. 4.6(a), incorporating Bi leads to an intensity dip at the energy position of the original Dirac point which is the signature of a small energy gap. We have also seen in Fig. 4.6(c),(d) that by increasing the Bi concentration, the intensity dip becomes more and more pronounced which is related to the widening of the surface gap.

In Fig. 4.8(b) we show the corresponding EDCs extracted from Fig. 4.8(a), where the EDC at normal emission is highlighted with a thick red line. The corresponding fit results (black solid lines) of the EDC (red circles) are shown in Fig. 4.8(c). The error bars in the determination of the surface gap correspond to the uncertainty of determining the energy position of the band dispersions, and are estimated from the standard deviations of the peak positions over several fitting cycles. Specifically, the size of the surface band gap is determined from the energy separation between the fitted Lorentzian peaks shown in blue (green) color, which are located at the energy minimum (maximum) of the upper (lower) part of the SS. We also would like to point out that a lower limit of the surface band gap can be obtained from the ARPES spectra after considering the contribution from the line-width broadening. The
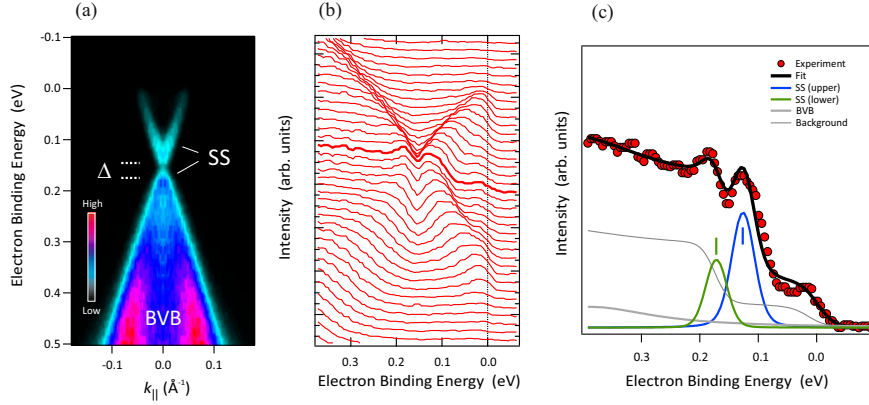
Figure 4.8: *(a) Energy-momentum ARPES dispersion measured at 30 K and 18 eV photon energy for $Pb_{0.72}Sn_{0.28}Se$ doped with 0.6% Bi. **(b)** Corresponding energy-distribution curves (EDCs) extracted from the ARPES data. The EDC at zero momentum is highlighted by a thick red line, which contains a double peak structure as the signature of a gap. **(c)** Corresponding fit results (black solid lines) of the EDC at zero momentum (red circles) considering a Shirley-like background [124]. The size of the surface band gap is determined from the energy separation between the fitted Lorentzian peaks shown in blue (green) color, which are located at the energy minimum (maximum) of the upper (lower) part of the SS. The Lorentzian peaks shown in gray color as a thick solid line represent the contribution from the BVB. The calculated gap size is $\sim45\pm10$ meV from our corresponding fitting method.*

lower limit of the surface band gap is approximately represented by horizontal dashed lines around the region of the gap as shown in Figs. 4.89(a). The other Lorentzian peaks shown in gray color are contributions from the BVB shown in Fig. 4.8(c). To extract the energy positions, the obtained EDC was fitted by a sum of Lorentzian functions plus a background. A typical spectrum containing N number of peaks were fitted by a function involving a convolution of the form:

$$I(E,k) = [f(E,T) \cdot \sum_{i=1}^{N} M_i^2 \cdot A_i(E_i, w_i) + B(E)] \otimes G(E) \tag{4.1}$$

Where E_i, ω_i and the matrix elements M_i are fitting parameters corresponding to the binding energy, width, and intensity of each Lorentzian peak, and $f(E,T)$ is the Fermi function. The spectral function $A_i(E_i, \omega_i)$ is approximated by Lorentzian functions, and $B(E)$ is assumed to be a Shirley-like background [124]. The full width at half maximum (FWHM) of the Gaussian slit function $G(E)$ corresponds to the total energy resolution of the experiment, which is photon energy ($h\nu$) dependent. Following the above mentioned procedure, we have estimated the gap size to be $\sim 45\pm10$ meV for this particular example as shown in Fig. 4.8(c).

2D nature of the gapped surface state: Now take a look at the gapped surface state of the $Pb_{1-x}Sn_xSe$ sample with Bi doping in more detail to determine its characteristics. For simplicity, here we consider the sample $Pb_{0.72}Sn_{0.28}Se$ doped with 2.2% Bi. Fig. 4.9 shows a 3D ARPES map around the $\overline{\Gamma}$ point for n_{Bi}=2.2% measured at temperature 30 K with 18 eV photon energy. This is to demonstrate that we have not missed any gapless states around $\overline{\Gamma}$ due to misalignment.
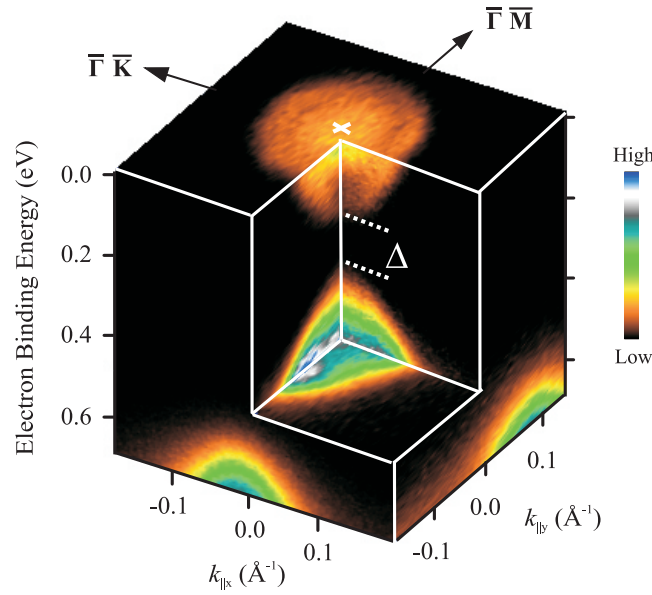

Figure 4.9: *Corresponding 3D ARPES map around the $\overline{\Gamma}$ point for n_{Bi}=2.2% measured with 18 eV photon energy. The measurement temperature is 30 K, well below the topological phase transition temperature for the same $Pb_{0.72}Sn_{0.28}Se$ sample without Bi doping.*

Figure 4.10 (a–f) demonstrate the photon energy dependence ARPES measurements of the gapped Dirac cone. The chosen photon energy range is in between 18 to 23 eV, where the both BCB and BVB dispersions are clearly visible. However, the gapped SS does not disperse with the photon energy, i.e., momentum perpendicular to the surface plane, and thus is two dimensional. The size of the surface gap also remains unchanged as indicated by horizontal dashed lines. In contrast, the intense BVB states appearing at higher binding energy clearly disperse with photon energy as marked by horizontal white arrows. Similarly, the dispersion of the BCB can be observed between 18 and 20 eV due to its three dimensional nature. Despite the overlap of the lower half of the SS with the BVB states, its intensity contribution can be seen as a non-dispersing feature near the border of the gap. This observation is important to rule out that the probed state could correspond to the gapped bulk states. To
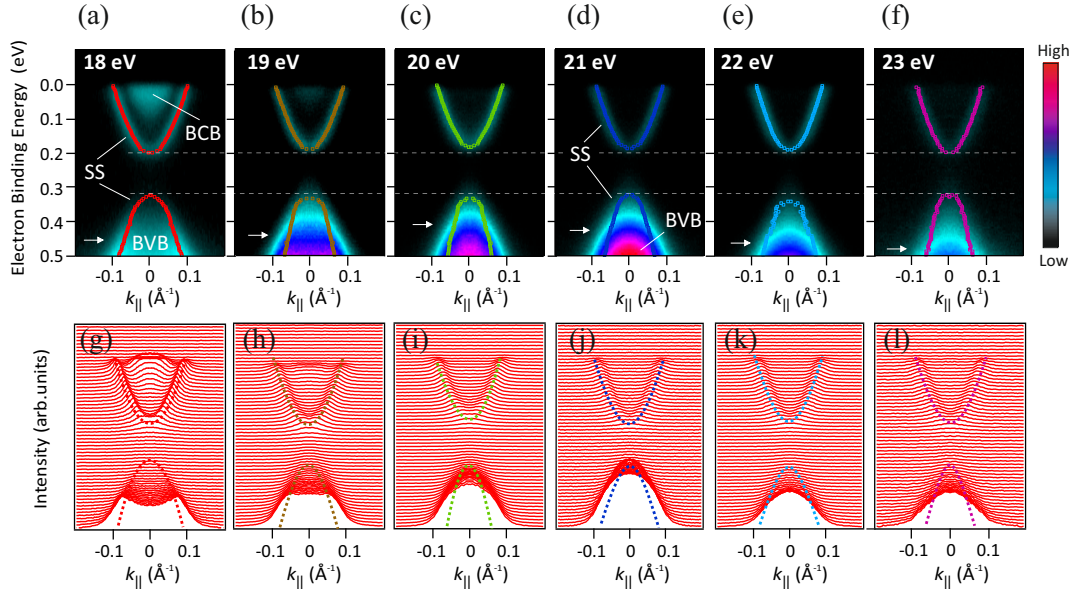
Figure 4.10: *Photon energy dependence of $Pb_{0.72}Sn_{0.28}Se$ doped with 2.2% Bi.(a-f) Photon-energy dependent ARPES spectra measured at 30 K.(g-l) Corresponding momentum-distribution curves (MDCs) derived from the ARPES results. the traced peak positions are the MDC spetra are marked by the dotted curves.*

evaluate the experimental band dispersions, we have traced the peak positions by analyzing the corresponding momentum-distribution curves (MDCs) as shown in the lower panels in Figs. 4.10 (g–l).

We summarize the procedure used by taking representative results at 18 eV and 22 eV photon energy as an example shown in Figs. 4.11 (a) and (e) respectively. For the fitting procedure, we have used a sum of Lorentzian peaks plus a constant background convoluted with a Gaussian function representing the momentum resolution, and thus a fit function which is similar to Eq. 4.1 but with the electron momentum parallel to the surface as the main variable. Fig. 4.11(a) shows the fit results of the upper and lower parts of the surface state superimposed on the corresponding ARPES dispersion measured at 18 eV. The fitted peak positions are also shown independently in Fig. 4.11 (b). Analogous results for measurements at 22 eV photon energy are displayed in Figs. 4.11(c),(d). From this comparison, we observe good agreement concerning both the energy positions of the upper parts of the surface state (USS) and lower part of the surface state (LSS) as well as their overall dispersion with momentum parallel to the surface. In Figs. 4.11 (e-h), we show few-selected fits (black solid lines) to the experimental MDCs (red symbols) obtained at various binding energies across the USS and LSS for photon energies of 18 eV (Figs. 4.11 (e,f)) and 22 eV (Figs. 4.11 (g,h)). The intensity contributions from the surface state are marked with black filled circles on top of
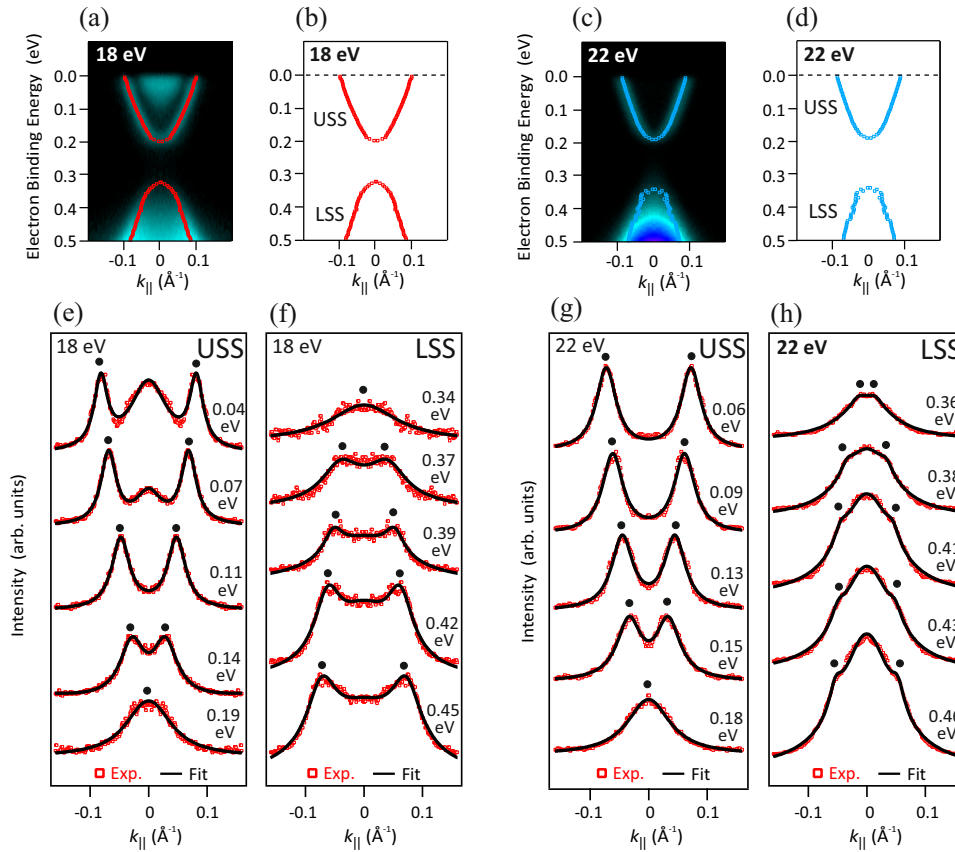
Figure 4.11: *(a) Band dispersion of the gapped surface state at 18 eV photon energy, with the peak positions extracted from fits to momentum-distribution curves (MDCs) superimposed. (b) Fit results as shown in (a), with the upper surface state (USS) and lower surface state (LSS). (c),(d): Analogous results for a photon energy of 22 eV. (e-h) Fits (black solid lines) to the experimental MDCs (red symbols) shown for selected binding energies across the upper and lower parts of the surface state at 18 eV and 22 eV photon energy. The intensity contributions from the surface state are marked with black filled circles on top of each fit.*

each fit. Additional intensities from the bulk-conduction band (BCB) near the Fermi level and from the bulk-valence band (BVB) at high binding energies were fitted by extra Lorentzian peaks introduced into the analysis procedure. As seen in Figs. 4.11 (e-h), the obtained fits are in remarkable agreement with the experimental MDCs. The intensity contributions from the upper part of the surface state as shown in Figs. 4.11 (e,g) appear as distinct peaks in the corresponding MDCs. This is also the case for the whole measured photon-energy range shown in Figs. 4.10, even for photon energies where the dispersion of the BCB is clearly observed. Similarly, the lower part of the surface state appears as pronounced peaks around the BVB intensity, which becomes progressively smaller with decreasing binding energy can be seen in as seen in Fig. 4.11 (f). This situation is more or less representative for fits to experimental MDCs up to photon energies of 21 eV. At higher photon energies, despite the dispersion of the BVB with momentum perpendicular to the surface k_z, we clearly resolve the opposite branches of the lower part of the surface state as pronounced shoulders around the BVB intensity shown in Fig. 4.11 (h). This allows us to extract the energy positions of the lower surface state with relatively good accuracy, despite the partial overlap with the BVB which nevertheless introduces additional errors in the fitted band dispersions. The error bars in the MDC fits were estimated from the standard deviations of the peak positions over several fitting cycles. In particular, the error bars in $\Delta k_{||}$ (ΔE) for each photon energy as shown in Figs. 4.10 were taken as the maximum error obtained for the whole fitted range, and the corresponding error bars in energy were estimated from the obtained $\Delta k_{||}$ values. These error bars represent the maximum uncertainty in determining the corresponding band dispersions as extracted from the MDC fits. By comparing the maximum error bar obtained from the MDC fits to the maximum deviation between the fitted results for different photon energies, we derive a total accuracy representing the upper bound for the maximal k_z dispersion of the surface state of ± 20 meV. This result strongly indicates that the gapped surface state is two dimensional, in contrast to the three-dimensional character of the BCB or the BVB which clearly disperse with photon energy.

4.2.1 TCI to $\mathbb{Z}_2$ Phase Transition

To determine whether in the topologically trivial phase the temperature dependence of the band gaps is similar at the $\overline{\Gamma}$ and at $\overline{M}$ points, ARPES data were recorded for a ~0.6% Bi-doped Pb$_{1-x}$Sn$_x$Se sample with a Sn content of 16% at temperatures ranging from 300 to 30 K. This particular Sn content was chosen to be close to the quantum critical point of the phase transition, but staying in the trivial phase for all investigated temperatures. The ARPES data shown in Figs. 4.12 reveal both the valence and conduction band states with an open gap corresponding to the non-inverted band structure. At $\overline{\Gamma}$, we clearly observe the contribution from topologically trivial surface states forming as precursor states of the quantum phase

transition, which are also seen in our ARPES spectra measured for $Pb_{1-x}Sn_xSe$ system as discussed above. This is in agreement with previous observations on undoped topological crystalline insulators [125]. We also point out that the same precursor states have been observed in quantum-phase transitions between trivial and $\mathbb{Z}_2$ topological insulators, which in addition preserve the helical spin texture despite their trivial origin [126]. Note that the intensity from the precursor states at the $\overline{M}$ points is less resolved in our data most probably because of their tilted projection onto the (111) plane, which corresponds to an electron emission angle of about $21°$ in the particular geometry.

On the topologically trivial side ($x_{Sn} <16\%$), for Bi doping $n_{Bi} <0.6\%$ no difference in the gap size Δ observed for $\overline{\Gamma}$ and $\overline{M}$. the states remain open at all temperatures as shown in Figure 4.12 (a-d). The band gaps at $\overline{\Gamma}$ and $\overline{M}$ follow the general trend and become smaller but remain open at the lowest measured temperature. This leads to the conclusion that the band gaps at the $\overline{\Gamma}$ and $\overline{M}$ points exhibit similar behavior with decreasing temperature.

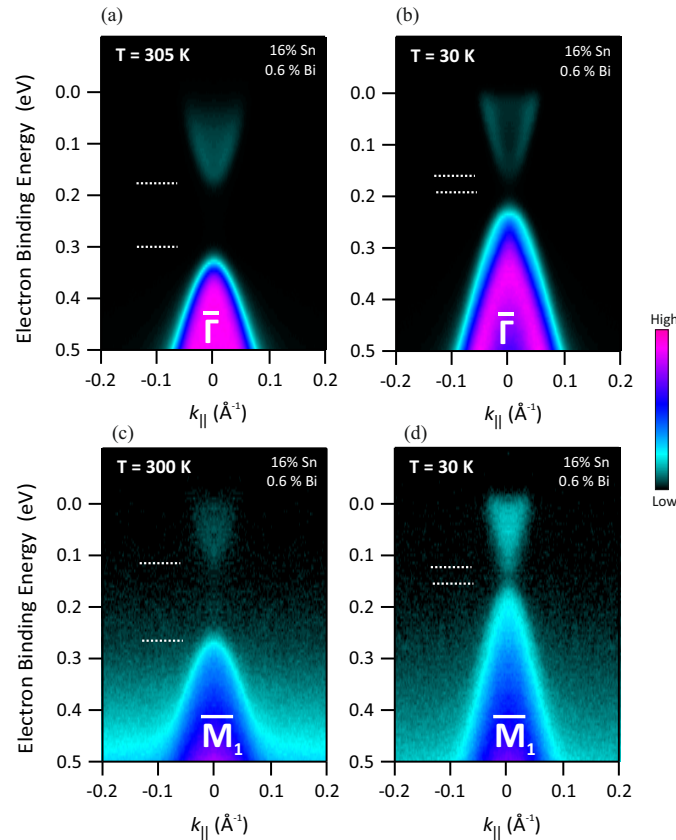**Figure 4.12: ARPES spectra of a control sample in the trivial state.** *(a-d) Energy momentum ARPES dispersions of a $Pb_{1-x}Sn_xSe$ (111) epilayer with 16% Sn and 0.6% Bi doping at (a,b) $\overline{\Gamma}$ and (c,d) $\overline{M}$, acquired at room temperature and 30 K.*

On the topologically non-trivial side (x_{Sn} >16%) in $Pb_{1-x}Sn_xSe$, the Dirac cones at $\overline{\Gamma}$ and $\overline{M}$ close synchronously as a function of temperature as shown in Fig. 4.13. For both $\overline{\Gamma}$ and $\overline{M}$ point we start with a trivial gapped state at room temperature as shown in Fig. 4.13(a,c). However upon cooling down the sample to a temperature well below the topological phase transition temperature, the bulk band gap closes and subsequent appearance of the Dirac cones at the $\overline{\Gamma}$ and $\overline{M}$ point are observed.
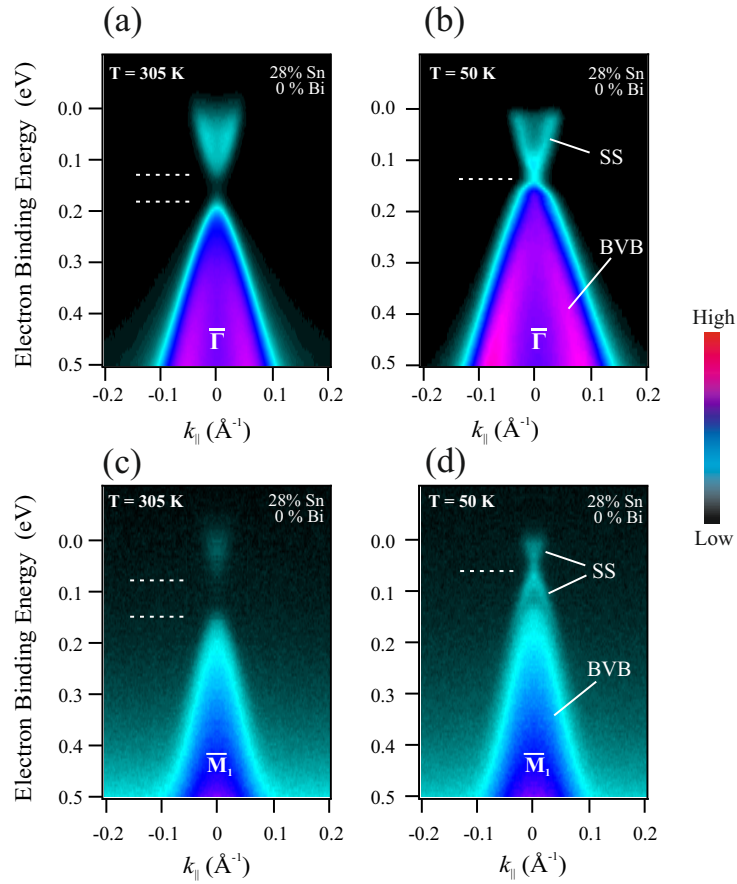

Figure 4.13: *ARPES data recorded using 18 eV photon energy at $\overline{\Gamma}$ and $\overline{M}$ without Bi doping where the Dirac cones simultaneously close at $\overline{\Gamma}$ and $\overline{M}$ below 150 K.*

On the contrary, for the samples with higher Bi doping (Fig. 4.14) the four-fold valley degeneracy is completely lifted such that the gap is closed at all three $\overline{M}$ points as shown in Figs. 4.14 (d-f), but remain opens as wide as 100 meV at the $\overline{\Gamma}$ point at 30 K (Fig. 4.14b). Thus, we conclude that of the even numbered Dirac cones per surface Brillouin zone, characteristic of a TCI, only three remain, qualifying $Pb_{1-x}Sn_xSe$:Bi as a strong $\mathbb{Z}_2$ topological insulator already for moderate Bi doping. This is the central result of chapter 4. While for a TCI the underlying protection is due to mirror symmetry, the odd numbered Dirac cones of a strong $\mathbb{Z}_2$ topological insulators are protected by time-reversal symmetry.

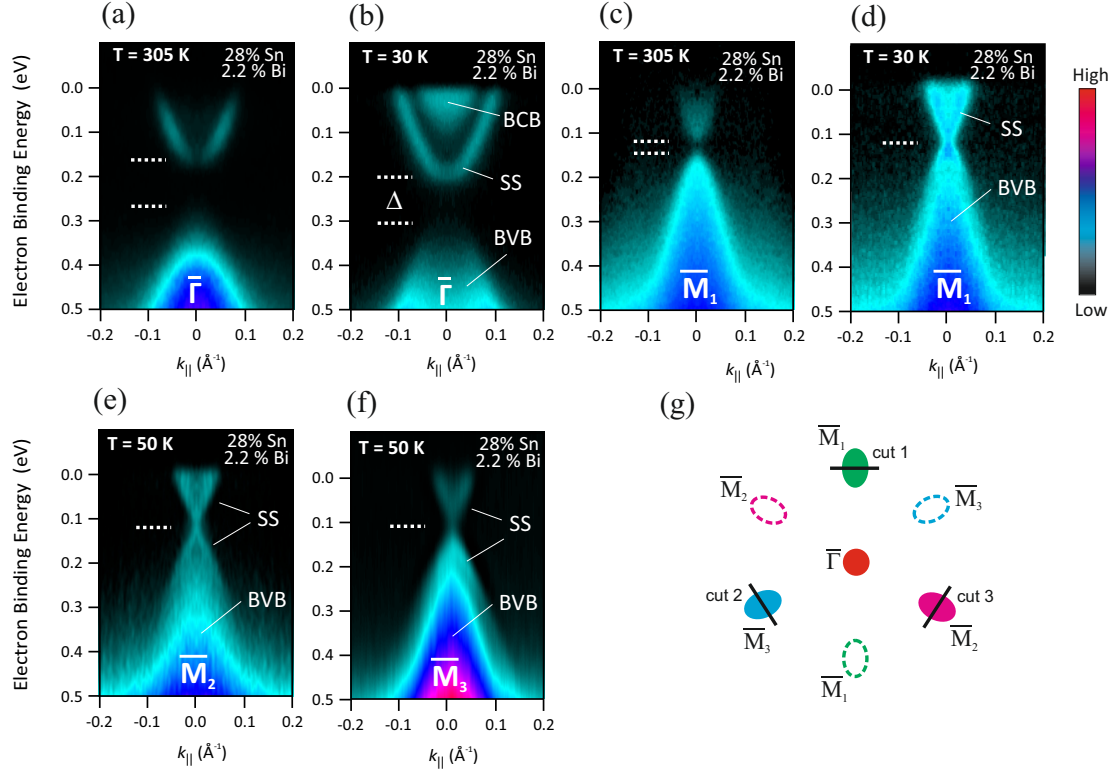Unlike the TCI surface state the strong $\mathbb{Z}_2$ surface states are robust against disorder.

Figure 4.14: *ARPES data recorded using 18 eV photon energy at $\overline{\Gamma}$ and $\overline{M}$ with 2.2% Bi doping where the Dirac cone is gapped at $\overline{\Gamma}$ (b) and intact at all three $\overline{M}$ points at low temperatures (d, e, f) respectively. **(g)** The momentum cut for the corresponding ARPES measurement for $\overline{M}$ point is perpendicular to the $\overline{\Gamma}$ $\overline{M}$ direction.*

Core-level photemission: Core-level spectra measured with 90 eV photon energy for Pb$_{1-x}$Sn$_x$Se with 28% Sn concentration and 2.2% Bi doping are shown in Fig. 4.15(a). The overlap of Bi 5d$_{5/2}$ with Sn 4d$_{5/2}$ emission is resolved by a fitting procedure, the results of which is shown in Fig. 4.15(b). To further evaluate the stoichiometry from the core-level spectra, in particular the Bi concentration, we analyzed the intensity ratios by taking into account the peak areas and the corresponding photoemission cross sections of the individual elements [127]. Specifically, we used a similar fitting procedure as the one described in determining the surface band gap. After normalizing the peak areas of individual elements by their photoemission cross section, we derived the Bi concentration from the ratio n$_{Bi}$=A$_{Bi}$/(A$_{Bi}$+B$_{Pb}$+C$_{Sn}$), where A, B, C denote the corresponding peak areas normalized with respect to the area under the Se peak. For the corresponding core-levels spectra, we derive A$_{Bi}$=0.0973, B$_{Pb}$=2.04129 and C$_{Sn}$=0.84593, which yields an absolute value of n$_{Bi}$ ∼ 3.2% that is in fair agreement with the more accurate result obtained using high resolution
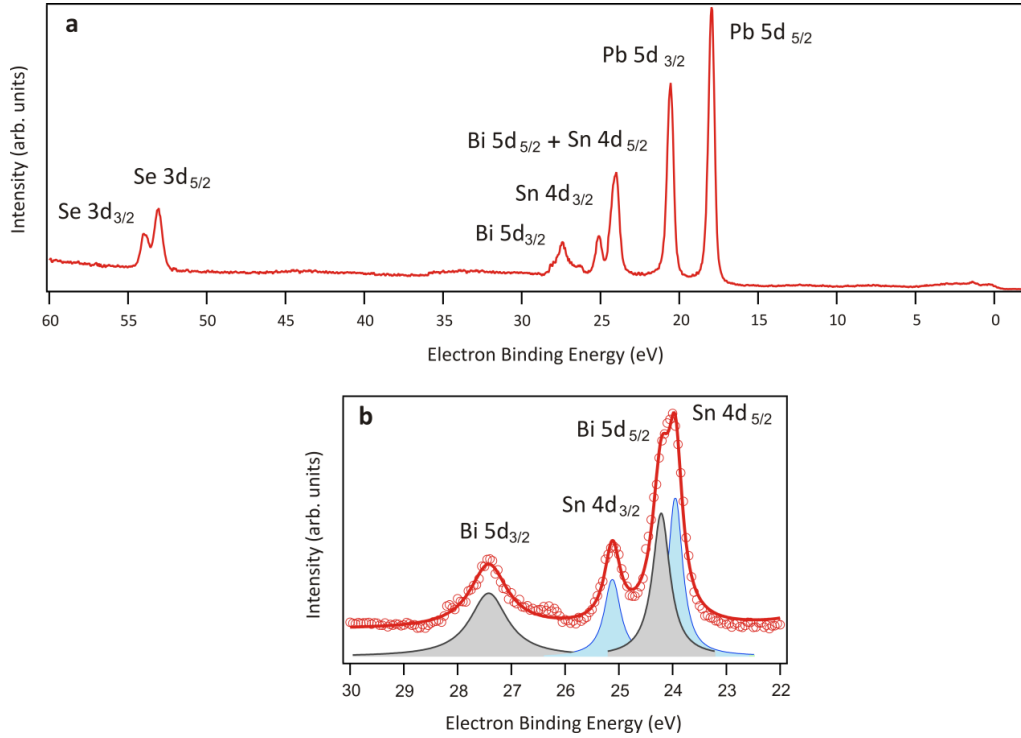
x-ray diffraction and the Vegard law shown in Appendix A.

Figure 4.15: *Core level spectra measured with hν = 90 eV photon energy for $Pb_{0.72}Sn_{0.28}Se$:Bi film. **(a)** 2.2% Bi doping measured after desorption of the Se cap at the ARPES setup. **(b)** Fitted spectra for Bi 5d and Sn 4d peaks.*

As described above, $Pb_{1-x}Sn_xSe$ (111) exists in different topological states depending on temperature, Sn and Bi doping. The band structures and the shape of the Dirac cones corresponding to the different topological phases are illustrated schematically in Figs. 4.16(a-c), where the open and closed Dirac cones are colored such as to indicate the changes of the predominant charge density at the anion (blue) and cation sites (orange) occurring during the band inversion [114]. For low $x_{Sn} < 16\%$, $Pb_{1-x}Sn_xSe$ is topologically trivial with an open and equal band gap at the $\overline{M}$, and $\overline{\Gamma}$ points of the surface Brillouin zone as schematics in Fig. 4.16(a). For higher x_{Sn}, a bulk band inversion occurs at low temperatures, which renders $Pb_{1-x}Sn_xSe$ as topological crystalline insulator, in which Dirac cones are formed at all four high symmetry points, i.e., all $\overline{M}$, and $\overline{\Gamma}$ points shown in Fig. 4.16(b). Upon Bi-doping, the valley degeneracy is lifted and a gap opens up at the $\overline{\Gamma}$ point, while the Dirac cones remain closed, i.e., ungapped at all three $\overline{M}$ – points. This makes Bi-doped $Pb_{1-x}Sn_xSe$ a $\mathbb{Z}_2$ topological insulator with odd number of band inversions in the surface Brillouin zone. This means the discovery of two new topological phase transitions in $Pb_{1-x}Sn_xSe$: (i) from trivial to topological $\mathbb{Z}_2$ by cooling and (ii) from topological crystalline to $\mathbb{Z}_2$ topological by adding Bi. The resulting topological phase diagram (Fig. 4.16 (d)) derived from our data

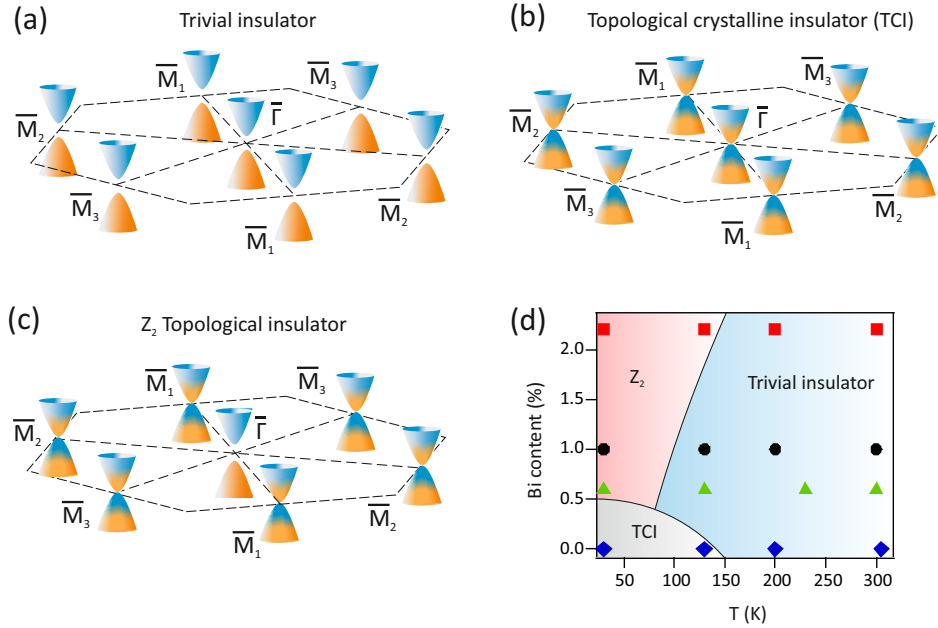shows the interdependence of these two pathways.

Figure 4.16: Topological phase transition as a function of Bi doping and temperature. *Schematic illustration of the transition from **(a)** trivial to **(b)** topological crystalline insulator (TCI) and eventually to **(c)** strong $\mathbb{Z}_2$ topological insulator. (d) Topological phase diagram derived from our ARPES data for $x_{Sn} = 28\%$. The phase diagram contains a trivial phase at high temperature (positive gap Δ at all four L-points) with massive gapped cones at $\overline{\Gamma}$ and $\overline{M}$; a TCI phase at low temperature with even $\mathbb{Z}_2$ invariant (all bulk L-points have negative, i.e., inverted gaps) and closed Dirac cones at $\overline{\Gamma}$ and all $\overline{M}$ points; a $\mathbb{Z}_2$ topological insulator phase with odd $\mathbb{Z}_2$ invariant due to a distortion along [111], giving three closed Dirac cones at the M points and an open gap at the $\overline{\Gamma}$ point.*

The behavior resembles the predictions by Plekhanov et al. for SnTe [114]. SnTe is known for its ferroelectric phase transition in which the anion and cation sub-lattices are shifted against each other along [111] direction according to the ref. [104], connected to a transverse optical phonon softening [123]. Plekhanov et al. tested small displacements and theoretically predicted that for a certain range of displacements a $\mathbb{Z}_2$ topological insulator can exist. In general, all IV-VI compounds are close to such a structural phase transition due to their mixed covalent-ionic bonding. They belong to the family of 10 electron systems and crystallize either in the cubic rock salt, rhombohedral, or orthorhombic structure. As calculated by Littlewood [128, 129] the type of structure in which a IV-VI compound crystallizes critically depends on the values of two bond orbital coordinates one is a measure of the ionicity and the other of covalency or s-p hybridization, and based on these a phase diagram has been established [128,129]. Due to the not fully saturated p-bonds, the rock salt structure is inherently unstable against rhombohedral distortions [128–130], which reduces the six nearest neighbors to three. The cubic/rhombohedral phase boundary is determined

by the electronegativity difference between the constituting elements and as a physical explanation of the instability the resonating bond model was invoked [131]. For the six nearest neighbors, the number of available p-electrons (six per atom pair) is not sufficient to stabilize the cubic bonds [132]. Thus, SnTe and GeTe assume a rhombohedral structure and even for PbTe minute addition of <0.5% of Ge suffices to drive $Pb_{1-x}Ge_xTe$ into the rhombohedral phase, rendering it ferroelectric [133, 134]. Thus, very small changes on the group IV lattice sites give rise to structural phase transitions. Indeed, for our Bi-doped films, we find a small Bi-induced rhombohedral distortion along the [111] direction using x-ray diffraction shown in Appendix A. The visualization of the rhombohedral angle α and the shift of anion and cation (111) planes that typically cause the rhombohedral distortion is depicted in Fig. 4.17. This indicates a ferroelectric inversion symmetry breaking as the underlying physical mechanism, which has been suggested to be much enhanced at the surface [111, 135]. Because of the (111) orientation of our films, this symmetry breaking lifts the even number degeneracy of the Dirac cones such that a gap is opened only at the $\overline{\Gamma}$ point. This leaves an odd number of Dirac cones intact at the three M points, causing the topological phase transition from a TCI to a $\mathbb{Z}_2$ topological insulator.
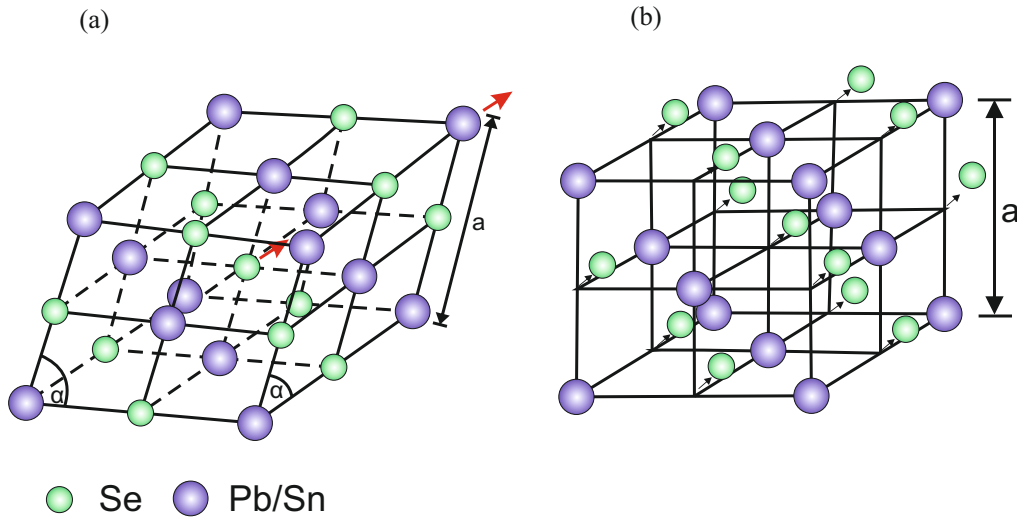

Figure 4.17: *Rhombohedral distortion:(a)* *Sketch of a rhombohedral distortion with rhombohedral angle $\alpha < 90°$. This angle corresponds to an elongation along the [111] direction. **(b)** A sublattice shift (green atoms) is shown which is responsible for ferroelectricity. For simplicity, this is shown for a cubic structure. The sublattice shift typically also leads to a rhombohedral distortion.*

Summary

In this chapter we have provided experimental evidences for two different topological phase transition in $Pb_{1-x}Sn_xSe$ system. First we have shown a trivial to TCI phase transition with systematic study of different Sn concentration ranging from 10% to 28% below and above the critical Sn concentration responsible for TCI phase transition together with a range of temperature from 300 K to 30 K. We also discussed a separate phase transition from TCI to $\mathbb{Z}_2$ topological insulator for $Pb_{0.72}Sn_{0.28}Se$ upon Bi doping. Here we would like to address the role of Bi as decisive ingredient for symmetry breaking even at small concentrations. Bi is another 10 electron system [136], covalently bonded and crystallizing in a rhombohedral structure. Accordingly, when incorporated at group IV lattice sites in $Pb_{1-x}Sn_xSe$, it shifts the alloy towards a more covalently bonded structure in the phase diagram [135, 137]. Moreover, on such lattice sites, Bi also reduces the cation vacancy concentration and the latter strongly enhances the ferroelectric Curie temperature T_C of the cubic-to-rhombohedral phase transition [131, 134, 138, 139]. Indeed, in SnTe thin films with reduced vacancy concentration, ferroelectricity up to room temperature was recently reported [139]. Thus, both effects of the Bi, higher covalency and lower vacancy concentration, contribute to structural symmetry breaking and trigger the TCI-to-$\mathbb{Z}_2$ topological phase transition discovered in the present work.

Chapter 5

Topological Crystalline Insulator Phase in $Pb_{1-x}Sn_xTe$

Lead tin telluride $Pb_{1-x}Sn_xTe$ is a tunable narrow bandgap semiconductor with a relatively higher operating temperature as compared to mercury cadmium telluride, which makes it a favorable candidate for commercial applications such as infrared detectors, diode laser, and thermoelectric devices [140–142]. There have been many studies in the late 60s showing $Pb_{1-x}Sn_xTe$ possess an even number of band inversions, tuned by the Pb/Sn ratio [143,144]. There were also theoretical predictions for the existence of the surface and interface states in the inverted bandgap but without any experimental evidence [145,146]. Since the prediction by Hsieh et al. the existence of a nontrivial surface states in SnTe, protected by the crystal mirror symmetry [45], it got much attention from the experimental condensed matter physics community. Soon enough it was shown by ARPES that SnTe and $Pb_{1-x}Sn_xTe$ are indeed a new type of topological insulator with even number of Dirac cones in their surface Brillouin zone [102, 103] and the band inversion occurs only above a certain value of Sn concentration in $Pb_{1-x}Sn_xTe$. We have discussed the properties of the TCI in chapter 1 and chapter 4.

In the first part of this chapter we will discuss the temperature and Sn concentration dependence of the trivial to TCI phase transition. As we have seen in the previous chapter the intrinsic p-type character in $Pb_{1-x}Sn_xSe$ which increases with increasing Sn concentration, caused by the natural tendency of cation vacancy formation, creates resonant acceptor levels in the valence band [131]. This effect is even more pronounced in the $Pb_{1-x}Sn_xTe$ system. In the second part of this chapter we will discuss the effect of Bi doping and the appearing of a Rashba effect in the valence band of $Pb_{1-x}Sn_xTe$ topological crystalline insulator. The Rashba splitting can be tuned by the doping level and therefore opens up new possibilities for technological applications which will also be discussed accordingly. The results of this chapter were published in Advanced Materials journal [1] [147].

---

[1]Author contribution: P. S. M. contributed to this publication the ARPES measurements together with

5.1   Basic Properties of $Pb_{1-x}Sn_xTe$

We will start this section by comparing the two very similar systems SnTe and PbTe in the same IV–VI semiconductor group where SnTe is topologically non trivial but PbTe is trivial. Both SnTe and PbTe have rock salt crystal structure with the space group symmetry $Fm\bar{3}m$ and they are both direct band gap semiconductors with slightly different gap values. SnTe has a lattice constant of $a_0 = 6.327$ Å and band gap of $E_g = 0.33$ eV whereas PbTe has lattice constant of $a_0 = 6.464$ Å and band gap of $E_g = 0.19$ eV. The topological character of SnTe is due to the reflection symmetry with respect to the (110) mirror plane. Fundamental band gaps in SnTe are located at four equivalent valleys in the face-centered cubic (FCC) Brillouin zone, where the valence band maximum is an L_{6-} and the conduction band minimum is an L_{6+} state. Although PbTe has similar band structure, the ordering of the valence band state and the conduction band state is reversed as compared to SnTe. In the case of PbTe the valence band maximum is an L_{6+} state and the conduction band minimum is an L_{6-} state.
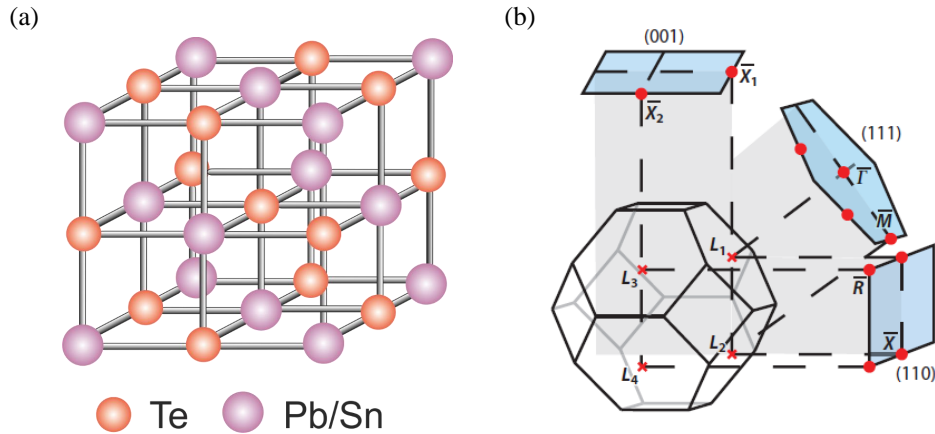

Figure 5.1: *(a) Rocksalt crystal structure of $Pb_{1-x}Sn_xTe$ with the space group symmetry $Fm\bar{3}m$, (b) High-symmetry points in the 3D Brillouin zone and in the projected surface Brillouin zone for three different surfaces of the rock-salt crystal structure. Adapted from Reference [148]; © 2013 by the American Physical Society.*

The different topological classification between SnTe and PbTe is directly related to their different Dirac masses [45]. The Sn concentration dependence of the band gap in $Pb_{1-x}Sn_xTe$ is shown in Fig.5.2, going from pure PbTe to SnTe. It has long been known that the band gap of the alloy closes at a critical Sn composition of $\sim x = 0.35$, and then reopens [144]. This band inversion corresponds to a sign change of the Dirac mass in the low-energy theory [149]. Theoreticians recognized the implication of the Dirac mass reversal in terms of the topology, which changes the mirror chern number associated with the plane passing through Γ and two

---

V. V. V., and their analysis performed together with V. V. V., J. S.-B., and G. S.

L points as shown in the Fig.5.1(b). Energy bands in the $\Gamma L_1 L_2$, $\Gamma L_3 L_4$, and $\Gamma L_1 L_3$ planes are mirror eigenstates indexed by $\eta = -is_x$, and the simultaneous band inversion at the two L points gives rise to a integer mirror chern number $|1 + 1| = 2$ [45]. On the basis of tight-binding calculations Hsieh et al. have shown that SnTe is a topological crystalline insulator whereas PbTe is not [45]. Nevertheless, even number of band inversions in the Brillouin Zone restricts the system to be a time reversal symmetric $\mathbb{Z}_2$ topological insulator [150]. The existence of the topological surface state in Pb$_{1-x}$Sn$_x$Te is protected by the mirror symmetry with non-zero mirror Chern number $|N_M| = 2$.
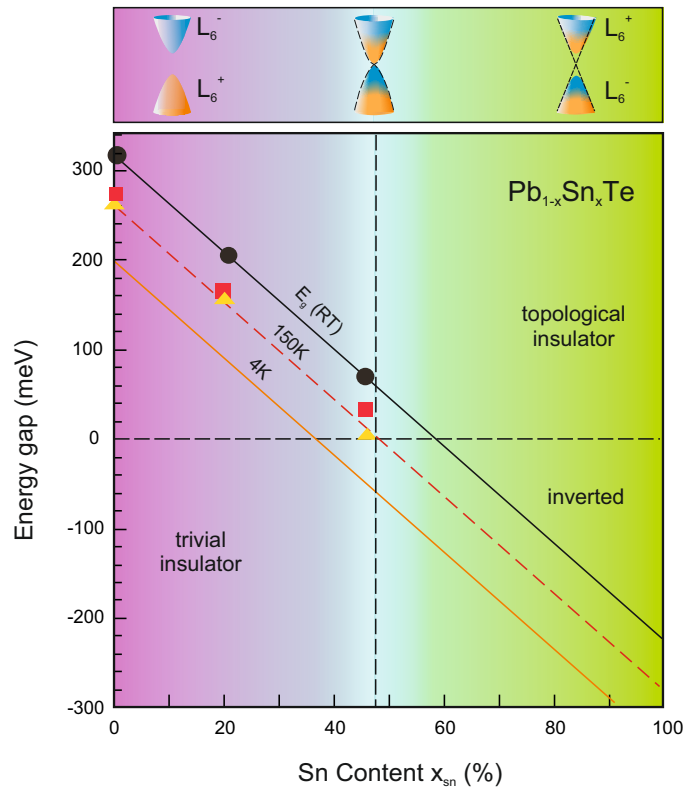

Figure 5.2: *Band gap dependence of Sn content x_{Sn} at T= 300, 150 and 4 K (solid and dashed lines)according to ref. [151,152]. Solid symbols represent the ARPES measurement at room temperature, 200 K, 150 K and 100 K obtained in the present study. The band inversion and trivial to non-trivial phase transition occurs at x_{Sn}= 0.36% and =0.6% for 4 and 300 K, respectively.*

The topological surface states in Pb$_{1-x}$Sn$_x$Te appear only on particular surfaces such as (001), (111) and (110), where the mirror symmetries are preserved [37, 45, 105]. Since the prediction of SnTe being a topological crystalline insulator, a series of studies have been performed mostly using ARPES to confirm the claim. Up to now most studies have been performed on bulk crystals with (001) surface, which is the natural cleavage plane of IV–VI compounds [102–104], but the samples are highly p-type. Because of the p type car-

rier concentration the chemical potential in these systems lies below the bulk valence band maximum, which makes it possible to observe only the lower Dirac cone from the valence band. However, a few recent studies demonstrate the possibility of studying the (111) surface [153, 154]. The (111) orientation is particularly interesting due to the polar nature of its surface [105] as well as the ease of lifting the fourfold valley degeneracy at the L-points of the Brillouin zone [155] by opening a gap at particular Dirac points by strain [156] and quantum confinement [115, 157, 158] to induce a transition from a TCI to a $\mathbb{Z}_2$ -TI material [114, 116]. Trivial to non-trivial band inversions in these systems are highly sensitive to external perturbation such as temperature [37, 104], pressure [45], hybridization in ultra-thin film geometries [115, 157, 158], magnetic interactions [159], or the breaking of mirror symmetries by strain [156, 160–162], electrostatic fields [158], or ferroelectric (FE) lattice distortions [114, 160].

Our present goal for the current chapter is to study (111) oriented $Pb_{1-x}Sn_xTe$ epilayers. Most challenging, however, is the intrinsic p-type character of $Pb_{1-x}Sn_xTe$ caused by the natural tendency of cation vacancy formation, creating resonant acceptor levels in the valence band (VB) [131]. This tendency strongly increases with increasing Sn content and thus, SnTe always exhibits very high bulk hole concentrations of around 10^{20} cm^{-3}. To overcome the bulk hole problem we have doped bismuth in $Pb_{1-x}Sn_xTe$ to achieve n-type conduction in the samples. Since the samples were grown by our collaborators at Johannes Kepler University in Linz, I will only briefly describe the method in the following section.

5.2   Topological Phase Transition of $Pb_{1-x}Sn_xTe$

We require high quality $Pb_{1-x}Sn_xTe$ films in which extrinsic n-type doping is employed for compensation and control of carrier concentration. We show that Bi doping allows to tune the Fermi level over a wide range from the valence to the conduction band. This will help us to observe the trivial to nontrivial topological phase transition with temperature and composition variation. By careful tuning of the doping level and growth conditions, low free carrier concentrations of 10^{18} cm^{-3} and carrier mobilities as high as 10^4 cm^{2}V^{-1}s^{-1} are achieved, which provides excellent conditions to study the non-trivial topological effect using quantum transport and optical measurements [163]. Epitaxial growth of $Pb_{1-x}Sn_xTe$ was performed by molecular beam epitaxy on BaF_2 (111) substrates using stoichiometric PbTe and SnTe beam flux sources [164, 165]. The chemical composition of the layers was varied over a wide range from $x_{Sn} = 0$ to 1 by control of the SnTe/PbTe beam flux ratio, which was measured precisely using the quartz crystal microbalance method [164]. The n-type doping was realized using a Bi_2Te_3 compound source to promote substitutional incorporation of bismuth into cation lattice sites [122] where Bi acts as donor because of its additional valence

electron compared to Pb or Sn [122,166]. The solubility of Bi_2Te_3 in SnTe and PbTe amounts to several percent according to the quasi binary phase diagrams where the solubility decreases with decreasing temperature according to ref. [167]. However, only small Bi concentrations and Bi flux rates in the $10^{-4} - 10^{-3}$ ML/s range are required for compensation of the native p-type carrier concentration, compared to overall film growth rates of 1 ML/s^{-1} (=3.7Å s^{-1}) used in our case.
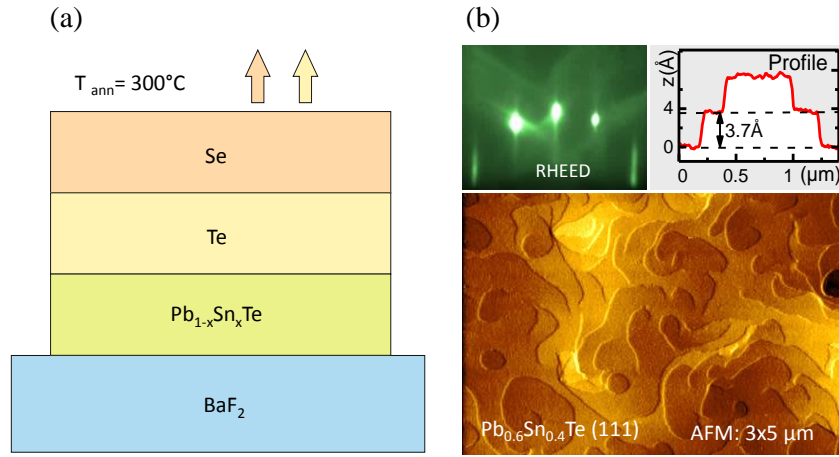

Figure 5.3: *(a) Schematic of the sample preparation on BaF_2 substrates, typical substrate temperature of $350^{\circ}C$ Composition and doping controlled by beam flux calibration using a quartz microbalance. (b) RHEED pattern and AFM image of $Pb_{0.6}Sn_{0.4}Te$ film grown by MBE on BaF_2 (111) substrate. The extracted surface profile shows only single monolayer steps with a height of 3.7 Å in the top right panel.*

2D growth of $Pb_{1-x}Sn_xTe$ (111) films is observed for all compositions beyond a thickness of 100 nm. This is illustrated by the reflection high-energy electron diffraction (RHEED) patterns and atomic force microscopy image depicted in Figures 5.3(b,c) for $x_{Sn} = 0.4\%$. The high film quality is evidenced by sharp diffraction spots arranged on the Laue circle and the intense Kikuchi lines arising from scattering at subsurface lattice planes. No surface reconstruction is observed as well. The surface is atomically flat exhibiting about 200 nm wide terraces separated by single monolayer steps of 3.7 Å height, which is shown in the top right panel of Fig. 5.3(b). At the given substrate temperature of 350°C, growth proceeds in a step-flow mode with the surface steps pinned by threading dislocations that originate from the growth on the lattice mismatched substrate as described in Refs. [117, 168]. Structural characterization done by high resolution x-ray reciprocal space mapping is discussed in Appendix B, which further demonstrate that the layers exceeding 100 nm in thickness are fully relaxed. The epilayers are undistorted with equal in- and out-of-plane lattice constants, and for all samples the Sn content derived by x-ray diffraction perfectly agrees with the nominal growth values.

The importance of Bi doping in $Pb_{1-x}Sn_xTe$ and its effect have been studied using Hall measurements, which we will discuss in more detail in Appendix B [147]. Studies have found that the carrier type of $Pb_{1-x}Sn_xTe$ switches from n to p-type at $x_{Sn} > 15\%$ and thereafter the hole concentration rises exponentially with increasing Sn content, and the doping of Bi develops an amphoteric character in the ternary materials and starts to occupy Te lattice sites as well, on which it acts like an acceptor. Thus, compensation of the native hole concentration becomes increasingly difficult at higher Sn contents [147].

We have studied the evolution of the topological surface state and population of the electronic bands in detail by ARPES as a function of temperature and composition in the 17–90 eV photon energy range. Fig. 5.4 shows the ARPES measurement with three different Sn concentration samples from 300 K downto 110 K, and we have observed the evolution of the bulk energy band gap with temperature. For both PbTe and $Pb_{0.74}Sn_{0.26}Te$, we did not observe any gap closing at the lowest temperature possible for our experiment, therefore no topological phase transition was observed. On the other side the sample with highest Sn concentration of $Pb_{0.32}Sn_{0.68}Te$ ($X_{Sn}68\%$) was highly p-doped and we were not able to observe the gap-closing at the Dirac point. Nevertheless the most promising sample for our experiment turns out to be the sample with moderate Sn concentration $Pb_{0.54}Sn_{0.46}Te$. We observed the band gap closing and appearance of the topological surface state very clearly for the sample with 46% Sn concentration shown in Fig 5.5. We will mainly focus on that sample for further studies. .

We have observed for n-doped $Pb_{0.54}Sn_{0.46}Te$:Bi films both conduction and valence bands, they are clearly visible in the ARPES measurements as shown in Fig. 5.5(a-d). However, for undoped films only the lower branch of the valence band is seen because the Fermi level is well below the valence band edge shown in Fig. 5.7(a). For a Bi doping of $n_{Bi} = 4\times 10^{19}$ cm^{-3} ($\sim 0.3\%$ Bi), the Fermi level E_F at room temperature is already by +100 meV above the conduction band edge and lowering the temperature induces a further upward shift to +160 meV at 110 K as shown in in Fig. 5.5 (a-c). At this temperature we observe a pronounced 2D topological surface state with linear dispersion, indicating the transition from the trivial to the non-trivial TCI state. Also, an increase in the Fermi velocity, i.e., slope of the $E(k)$ dispersion occurs due to the decrease of the effective masses accompanying the closing of the gap [131, 152]. This in turn leads to a decrease in the electronic density of states, which means that the Fermi energy must shift upwards at lower temperatures to accommodate the temperature independent, i.e., constant carrier concentration as observed by the Hall effect measurements. The topological phase transition in the $Pb_{0.54}Sn_{0.46}Te$:Bi happens at about 110 K, and we also observe some instability in the ARPES spectra below 80 K which we assign as due to the photo-induced adsorption of residual gases and resulting charging of the sample.
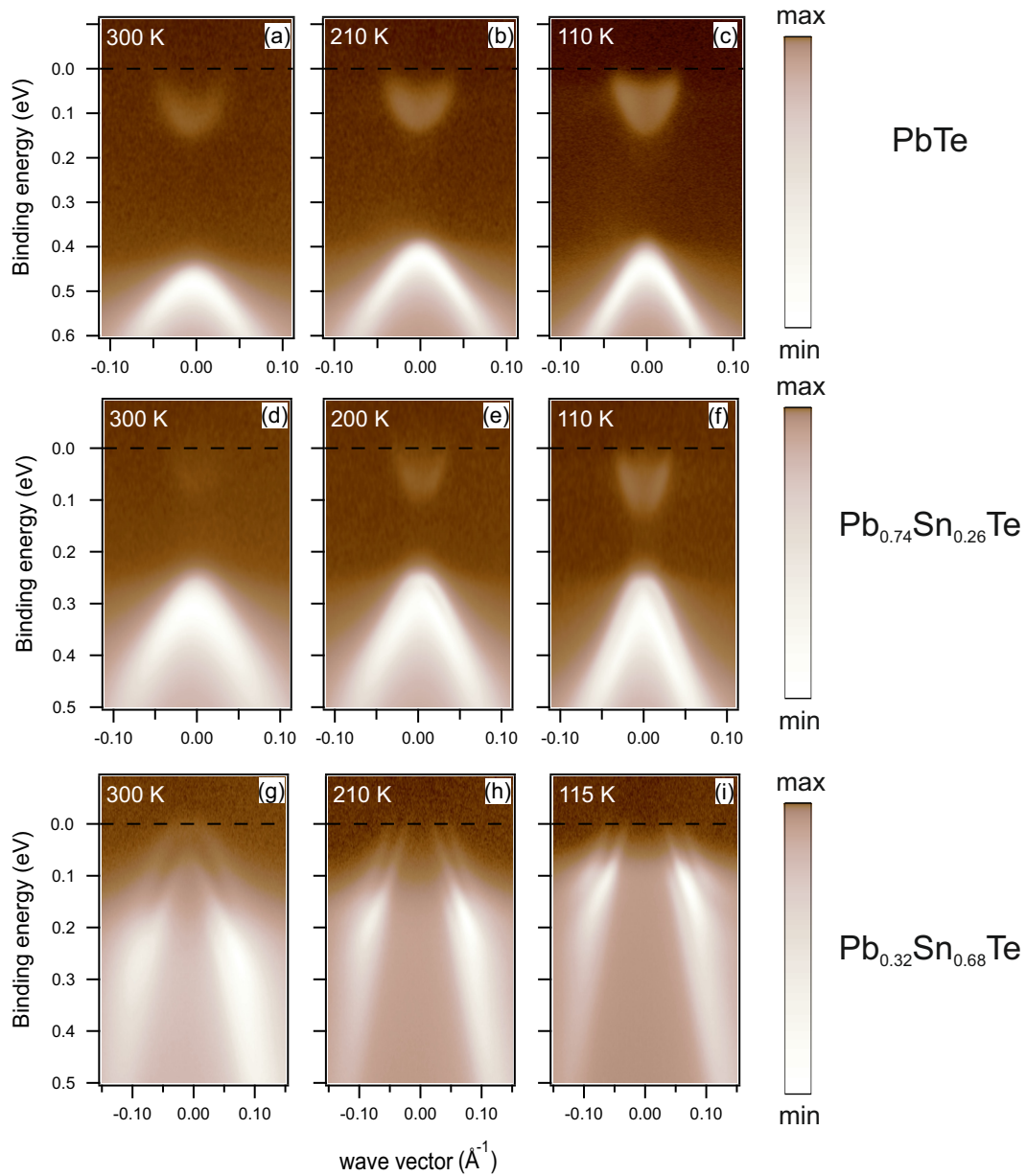
Figure 5.4: Temperature and Sn concentration dependent ARPES measurements of $Pb_{1-x}Sn_xTe$ with x_{Sn} = 0%, 26%, and 68%. PbTe and $Pb_{0.74}Sn_{0.26}Te$ does not show bulk band inversion at the lowest measured temperature. In the case of $Pb_{0.32}Sn_{0.68}Te$ (68%), Dirac point of the topological surface state is not observable due to high p-doping of the sample.

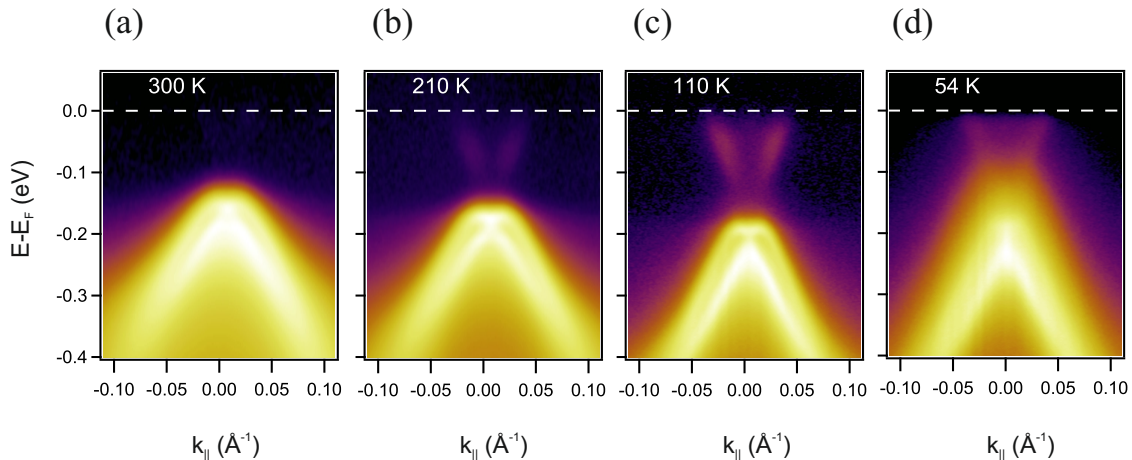**Figure 5.5:** *Topological phase transition charaterized by ARPES Temperature-dependent E(k) maps of $Pb_{0.54}Sn_{0.46}Te$ (111) epilayers with 0.3% bismuth measured around $\overline{\Gamma}$ using a photon energy of 18eV. Topological phase transition occurs at about 110 K. Below 80 K photoemission becomes unstable due to photoinduced adsorption of residual gas and charging of the sample.*

The 2D nature of the observed surface state was verified by photon energy dependent ARPES investigations shown in Figs. 5.6 (a-e). In spite of different admixtures of dispersive bulk and non-dispersive surface signals at different photon energies, our ARPES measurements corroborates that the observed bands indeed have 2-D character, i.e are surface states. Moreover at this temperature, we observe a Rashba split state overlapping with the topological surface states (TSS) in the lower part of the Dirac cone. The coexistence and hybridization of the topological surface states and Rashba-split surface state is unexpected especially in view of the inversion symmetry of the TCI rock salt structure and might pave the way for novel topological spin-orbitronic devices [169].

For the n-doped $Pb_{0.54}Sn_{0.46}Te$:Bi films, linear extrapolation of the TSS from the conduction band yields a Dirac point position at $10-20$ meV below the VB maximum at 110 K. This is revealed clearly by Figs. 5.7 (b,c), where the ARPES intensity is depicted on a logarithmic scale. The ARPES data of a film with $x_{Sn} = 26\%$, in which the gap remains fully open with $E_g \approx 120$ meV even at low temperatures, i.e., for low Sn contents $Pb_{1-x}Sn_xTe$ remains topologically trivial. Thus, the trivial to non-trivial topological phase transition is demonstrated for (111) epitaxial films both as a function of temperature and Sn content. It is noted that the topological phase transition was previously suggested to occur already at $x_{Sn} \approx 0.25$ for cleaved (001) bulk $Pb_{1-x}Sn_xTe$ crystals [170]. However, that conclusion was based only on extrapolation of the dispersion of the valence band of highly p-type material without directly observing the Dirac point and conduction band.

5.3   Giant Rashba Splitting in Pb$_{1-x}$Sn$_x$Te Controlled by Bi Doping in Bulk

As briefly mentioned above, we find that Bi-doping induces a very large Rashba splitting of the valence band. It is absent for undoped material and reaches values as high as 0.022 Å^{-1} [147]. This yields a giant Rashba coupling constant of 3.8 eVÅ^{-1} that is comparable to the record values recently reported for the BiTe-halide compounds [171–173]. To map out the correlation with the doping level, ARPES experiment was performed for a series of Pb$_{0.54}$Sn$_{0.46}$Te layers with systematically increasing doping of Bi. The results are presented
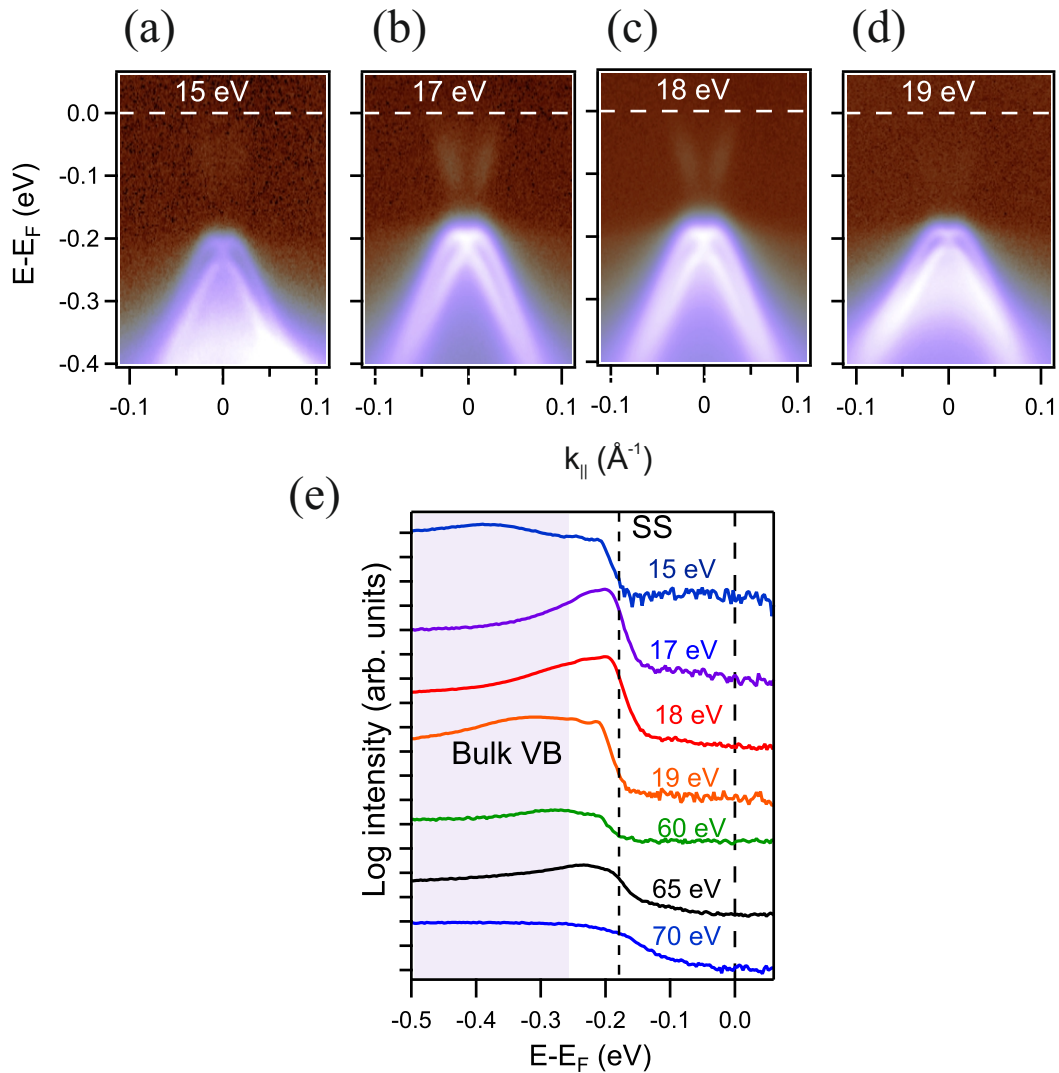

Figure 5.6: *Photon energy dependent ARPES spectra of Pb$_{0.54}$Sn$_{0.46}$Te: Bi (111) epilayers measured at 110 K shows the two-dimensional nature of the Rashba split state overlapping with the topological surface states in the lower part of the Dirac cone.*
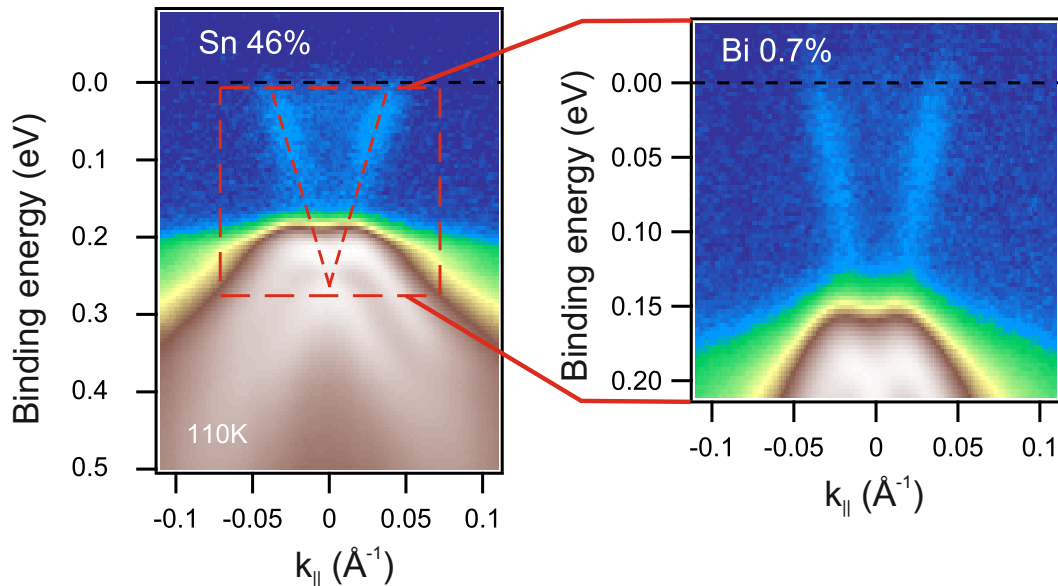
Figure 5.7: *ARPES spectra of $Pb_{0.54}Sn_{0.46}Te$:Bi epilayer shows closed gap Dirac cone surface state measured at 110 K with 18 eV photon energy. Close view of shows the Dirac point of the topological surface state (TSS) and the Kramer's point of the Rashba split valence band coexist. The photoemission intensity is shown on a logarithmic scale to reveal the TSS in the conduction band.*

in Fig. 5.8 for Bi concentrations varying from 0% to 1%. For the undoped film the Fermi level stays deep inside the valence band and it strongly moves upward with increasing Bi content. A doping level of $n_{Bi} > 0.2\%$, the full valence and conduction bands appears as observed in our ARPES measurements. In fact, a total shift of E_F by as much +280 meV is achieved by 1% Bi doping, evidencing the effective control of the Fermi level as this was the intended effect of the Bi doping. However, and retrospectively most importantly, we find that the Rashba splitting systematically increases with the Bi concentration. Thus, the Rashba effect is induced by the bulk doping of the material, which is in complete contrast to the reported Rashba effect in $\mathbb{Z}_2$ -topological insulators such as Bi_2Se_3. The Rashba effect for Bi_2Se_3 is usually induced by alkaline [174, 175] or transition metal deposition [176] or adsorption of water on the surface [177, 178], but not upon bulk doping [176, 179–182]. Moreover, it is to be noted that in these $\mathbb{Z}_2$ TIs the Rashba bands are completely separated in energy from the topological surface state, whereas in our TCI case the Dirac and Kramers points overlap as seen in Fig 5.7. This suggests that a strong a hybridization between the topological surface states and the Rashba bands may occur.

For quantitative evaluation, the Rashba bands were modeled using the effective mass approximation where the energy-momentum dispersion is given by

$$E(k_\pm) = \hbar^2 k^2/2m^* + \alpha_R(\vec{\sigma} \times \vec{k})\hat{z} = \hbar^2 k^2/2m^* \pm \alpha_R k \qquad (5.1)$$
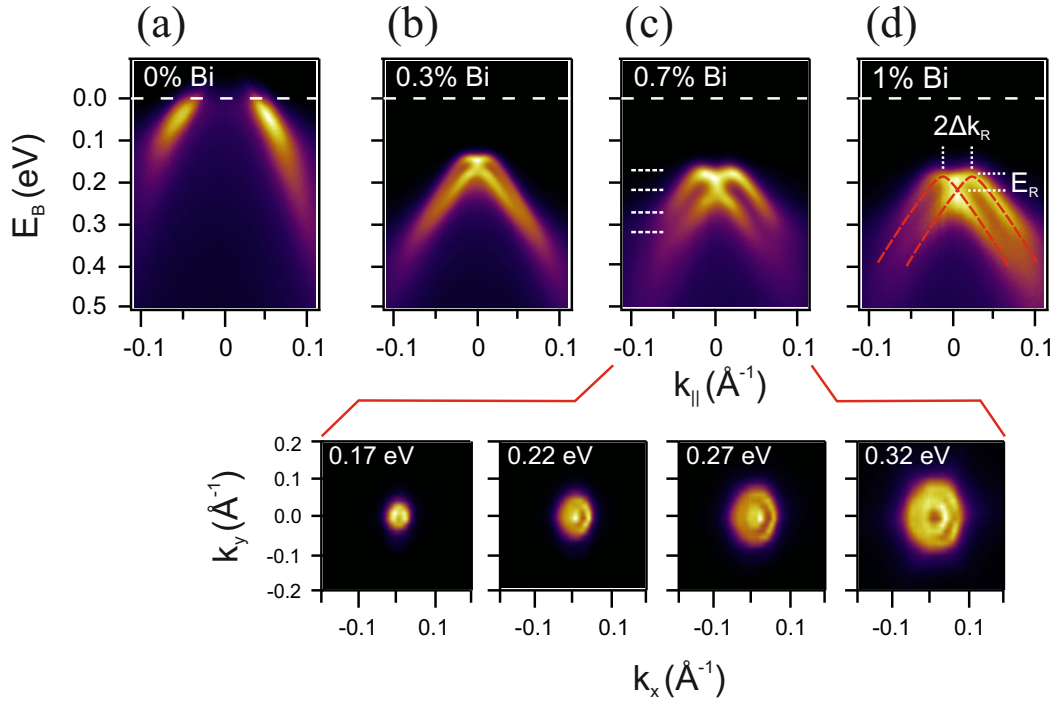
Figure 5.8: *Effect of bulk Bi doping on the Rashba effect:(a)−(d) ARPES spectra of $Pb_{0.54}Sn_{0.46}$Te (111) with bulk Bi concentration varying from $n_{Bi} = 0$ to 1%, demonstrating the effective tuning of the Fermi level and the strong increase of the Rashba splitting with Bi concentration. The ARPES maps were recorded around the $\overline{\Gamma}$-point at 100 K with a photon energy of 18 eV. The derivation of the Rashba coefficient α_R from the measured Δk_R and E_R is shown schematically in (d) and the result is listed in table 5.1. Constant-energy contours at different binding energies for the sample with $n_{Bi} = 0.7\%$ showing the concentric rings of the Rashba bands and increasing hexagonal warping.*

where m^* is the effective carrier mass in the $k_{||}$ direction, σ the Pauli spin matrix, and α_R the Rashba coefficient due to spin-orbit coupling and structural asymmetry at the surface. The Rashba effect causes the formation of two separate spin polarized bands $E(k_+)$ and $E(k_-)$ that are split by $2\Delta k_R$ in the $k_{||}$ direction as discussed in the introductory chapter 2. The Rashba effect in $Pb_{1-x}Sn_xTe$ for 1.1% Bi doping is indicated schematically by the dashed lines in Fig. 5.8(d). This leads to a nested band structure with helical spin texture, forming concentric rings in the k_{xy} plane as corroborated by the constant energy ARPES maps depicted in Fig. 5.8 for $Pb_{0.54}Sn_{0.46}Te$ with 0.7% Bi doping. This is a key hallmark of the Rashba effect. From the data, we derive the momentum splitting Δk_R and Rashba energy E_R (= energy difference between the band maxima and the Kramers point) for each sample, which yields the Rashba coefficient $\alpha_R = 2E_R/\Delta k_R$ as a function of the doping level. The results are summarized in Table 5.1, demonstrating a clear correlation between the Rashba parameters and Bi concentration. In particular, the Rashba coefficient assumes exceedingly large values of $\alpha_R = 3.8$ eV for 1% Bi-doping, which is comparable to the recently reported record values of the giant Rashba systems such as BiTeX (X=I, Br, Cl) and α-GeTe where α_R is of the order of 2–4 eVÅ [109, 171–173, 183–185].

n_{Bi} [%]	E_F [meV]	E_R [meV]	k_R [Å^{-1}]	α_R [eVÅ^{-1}]
0	-80	-	-	-
0.3	+140	13	0.011	2.4
0.7	+170	30	0.017	3.5
0.9	+190	38	0.022	3.8

Table 5.1: Rashba parameters of $Pb_{0.54}Sn_{0.46}Te$ (111) as a function of Bi concentration n_{Bi} measured by ARPES at 110 K (Fig. 5.8), including Fermi energy E_F (relative to the top of valence band), Rashba energy E_R, momentum splitting k_R, and Rashba constant $\alpha_R = 2E_R/k_R$.

The giant Rashba splitting is quite unexpected for materials possessing inversion symmetry as applies for the IV-VI compounds with cubic rock salt crystal structure. As recently suggested, ferroelectric (FE) lattice distortions can lead to a giant bulk Rashba splitting [183] in α-GeTe [184, 185] and SnTe [114]. Plekhanov et al. obtained in the phase diagram for SnTe in addition to the $\mathbb{Z}_2$ phase observed for $Pb_{1-x}Sn_xSe$ in chapter 4 also a bulk, i.e, 3D, Rashba phase as a function of the Ferroelectric (FE) lattice distortion. In our $Pb_{1-x}Sn_xTe$ films, however, we do not observe such distortions by x-ray diffraction down to 80 K, and even pure SnTe becomes ferroelectric only at low temperatures. Moreover, for films we do not observe any abrupt change of the Rashba effect with temperature (cf. Figure 5.3) as would be expected at such a FE phase transition. Thus, we rule out bulk inversion symmetry breaking and the Dresselhaus mechanism as discussed in the Chapter 2 as an origin for our

Rashba effect. Instead, we invoke a symmetry breaking at the surface. In fact, the mere existence of the surface can produce spin polarized surface states, as has been shown in the case of $Pb_{0.73}Sn_{0.27}$Se in the trivial insulator phase [186]. A surface band bending can tune these states to the band gap region, and/or produce new states localized at the surface and enhance the spin splitting. The pertaining Rashba effect will be thus confined to the surface, in agreement with the observed 2D nature of the Rashba bands revealed by the photon energy dependence Fig. 5.6. We suggest that the surface band bending for PbSnTe (111) is caused by a pinning of the Fermi level by localized trap states at the surface due to dangling bonds. This results in the presence of a fixed surface charge σ_S that induces a depletion layer below the surface. For degenerately doped semiconductors this is described by the Thomas-Fermi screening model with a screening potential of

$$V(z) = V_0 exp(-z/\lambda) \tag{5.2}$$

where V_0 is the potential at the surface at z = 0 and $\lambda = \pi^{2/3}\hbar\sqrt{\epsilon_0\epsilon_s/e^2m^*(3n)^{1/3}}$ is the Thomas-Fermi screening length [187], which is of the order of a few nanometers for highly doped semiconductors. The surface potential V_0 is related to the surface charge by $V_0 = -\sigma_S\lambda/\epsilon_0\epsilon_s$ through the Poisson equation and the overall charge neutrality condition. For acceptor-like trap states, the trapped surface charge σ_S is negative so that the bands bend upwards at the surface and V_0 assumes a positive value. Likewise, for donor-like surface states σ_S is positive, inducing a downward band bending corresponding to negative V_0 values.

To show that the Rashba effect is neither due to Bi accumulation at the surface nor due to specific properties of the Bi, additional experiments were performed. It is well known that Bi on metal surfaces can induce a large Rashba splitting due to its large spin-orbit coupling, as e.g., for Bi/Ag(111) surface alloys [187, 188]. To rule out such an effect, we have deposited 0.5–1 ML of Bi on top of undoped $Pb_{0.54}Sn_{0.46}$Te (111) at a temperature of 200 K. The resulting ARPES data, shown in Figure 5.9(b,c) reveals that this does not cause any Rashba splitting of the $Pb_{1-x}Sn_x$Te bands. After 1 ML surface deposition, the characteristic Bi $5d_{3/2}$ core level peak is higher than the Sn 4d and Pb 5d core level peaks. This corroborates that simple Bi accumulation on the PbSnTe surface, e.g. by surface segregation, would not explain our Rashba effect.

To further demonstrate that the Rashba effect also does not rely on any specific property of the Bi dopant, we have prepared $Pb_{0.54}Sn_{0.46}$Te films where Bi was replaced by Sb as group V and n–type dopant. As shown by the Fig. 5.9(a), for such films a similar giant Rashba effect is observed. In fact, for a nominal Sb concentration of 3% we obtain an even larger Rashba splitting of $\Delta k_R = 0.036$ $Å^{-1}$ and $E_R = 56$ meV as compared to the 1% Bi doped sample. This is further underlined by the core level spectra of our bulk-doped films in Fig. 5.10, which show that the surface concentration of Bi remains very small in all samples
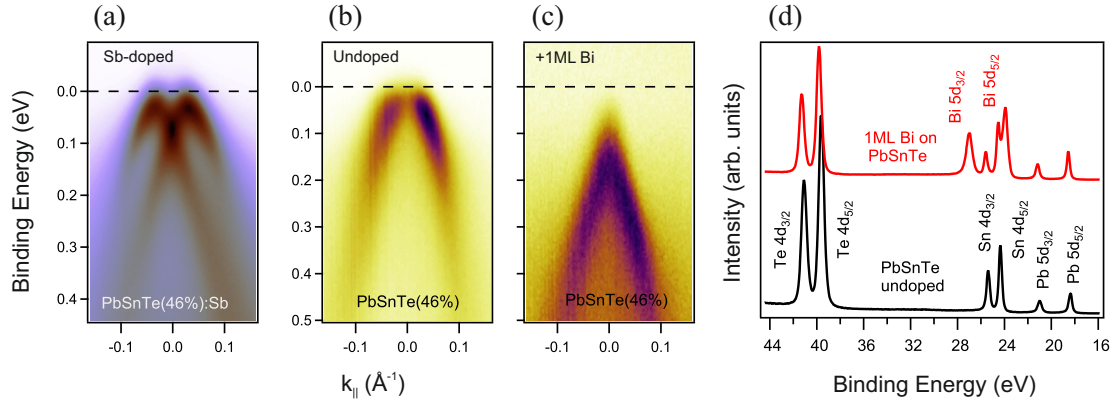
Figure 5.9: *(a) ARPES spectra of a $Pb_{0.54}Sn_{0.46}Te$ (111) layers with 3% Sb doping in the bulk, evidencing a similar type of the Rashba effect as observed for Bi-doped sample. (b-c) ARPES map of an undoped $Pb_{0.54}Sn_{0.46}Te$ (111) layer before, and after 1 ML Bi deposition on the surface at 200 K respectively. The ARPES measurements were recorded around the $\overline{\Gamma}$ point at 100 K with a photon energy of 18 eV. (d) The corresponding core level spectra recorded before and after 1 ML Bi deposition using 90 eV photon energy.*

and that no notable Bi accumulation occurs. This clearly indicates that the Rashba effect is solely controlled by the bulk Fermi level and thus will occur for any other n-type dopant of the system.

The influence of the surface band bending on the surface spectral density of states was evaluated by tight binding (TB) calculations by our collaborator at Polish Academy of Science. In this TB calculation different surface potentials according to Equation 5.2 were superimposed on the atomic potentials of $Pb_{0.54}Sn_{0.46}Te$ obtained in refs. [104] and [105]. We assume an anion (Te) termination of the (111) surface as density functional theory (DFT) calculations [189] suggest that this surface exhibits a lower surface energy than the cation termination. The results are presented for $\lambda = 2.5$ Å and V_0 varying from -0.5, $+0.3$, and $+0.1$ eV from Figs. 5.11(a) to (c), respectively. The solid lines correspond to the 2D surface states and the shaded regions to the bulk bands. Evidently, surface band bending induces a strong Rashba splitting in either the CB or VB depending on the "sign" of V_0. Positive V_0 (i.e., upward band bending) leads to a Rashba splitting in the VB due to the confinement of the hole wave functions near the surface. Conversely, for negative V_0 the Rashba-split states appear in the CB. Comparison with our experiments reveals that only the upward band bending, i.e., $V_0 > 0$, is consistent with the ARPES data, which demonstrates the presence of a negative surface charge σ_S on the anion-terminated surface.

From our TB calculations, we derive the dependence of Rashba parameters as a function of surface potential as presented in Fig. 5.11(d). Evidently, the momentum splitting Δk_R and Rashba coefficient scale linearly, and E_R quadratically with the surface potential V_0, i.e., with increasing electric field strength $E \approx dV/dz$ at the surface. Comparison with the
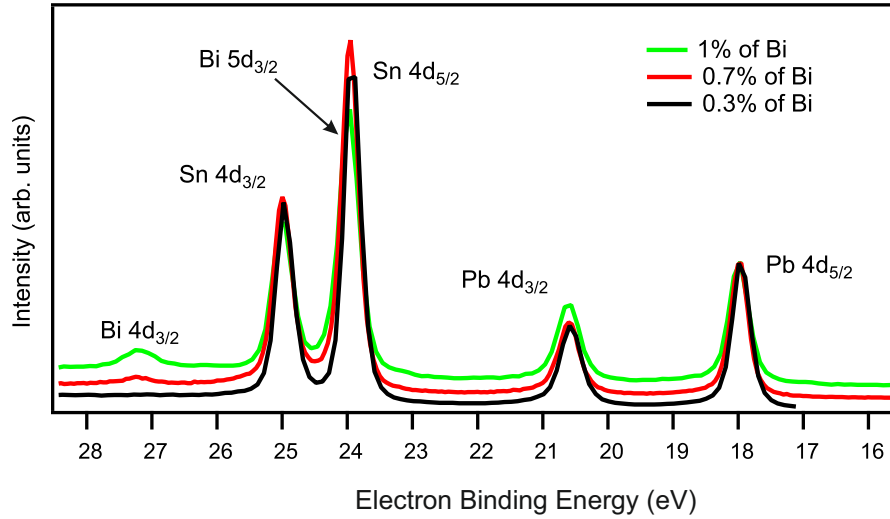
Figure 5.10: *Core level spectra excited with $h\nu = 90eV$ showing the Bi $4d_{(3/2)}$ peak for increasing doping level.*
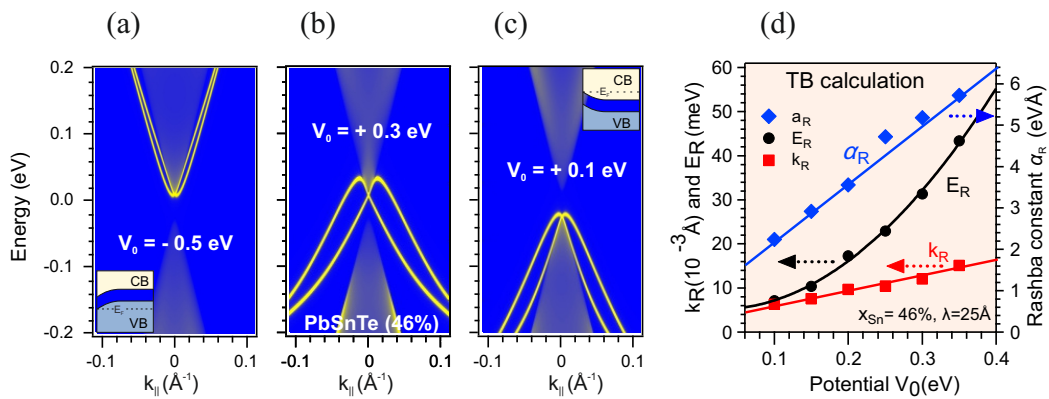
Figure 5.11: *Tight binding supercell calculation of the Rashba effect of $Pb_{0.54}Sn_{0.46}Te$ (111) induced by (a) a downward or (b),(c) an upward band bending towards the surface due to a negative and positive surface potential V_0, respectively. the screening length was set to $\lambda = 25$ Åand $T = 200$ K. The Rashba coefficient derived from the calculation k_R(■), E_R(●), and $\alpha_R = 2E_R/k_R$(◆) are plotted in (d) as a function of surface potential.*

experimentally obtained values indicates a surface potential V$_0$ of around +0.1 to +0.3 eV for our samples, which for the given screening length and dielectric constant yields a surface charge of the order of 1/10 electron per surface atom. However, the observed increase of the Rashba splitting with increasing Bi-doping dictates that this surface charge is not constant but varies with the bulk Fermi level. Thus, it cannot be simply due to the polar nature of the (111) surface as previously suggested [153], but rather by localized surface trap states that are successively filled by electrons as the bulk Fermi level increases. For p-doped samples these trap states are unoccupied, corresponding to a flat band condition shown in Fig. 5.12 without a Rashba effect–as seen in our performed experiments. Comparing calculated and measured Rashba parameters, we find a good agreement for V$_0$= +0.2 eV where α_R is of the order of 3 eVÅ^{-1} in both theory and experiment.
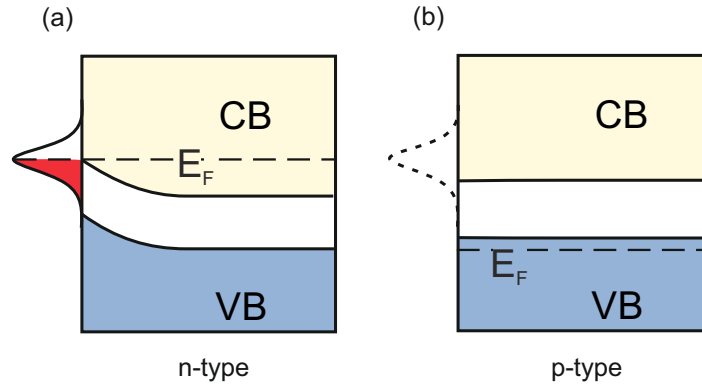

Figure 5.12: *Illustration of the surface band bending induced by localized electron traps at the surface that become populated with increasing bulk doping* **(a)**, *whereas without Bi doping the traps are not occupied and no band bending occurs* **(b)**.

The upward surface band bending also nicely explains the weak intensity of the CB band states in the ARPES maps as well as TB calculations because accordingly their spectral weight is much reduced at the surface because their wave functions are pushed into the bulk away from the surface. Also note that for a given α_R value, Δk_R and E$_R$ of the TB calculations are somewhat smaller than the experimental values. Since both are proportional to the in-plane effective mass m*, this is attributed to the fact that m* is underestimated by a factor of 1.8 in the TB binding calculations as compared to the experiments. The effect of temperature and screening length variation is discussed in the following.

To find appropriate parameters for the Thomas-Fermi screening potential, a series of calculations have also been performed, in which both the potential amplitude as well as the potential screening length have been changed (Equation 5.2). For each pair of parameters the recursive, decimation method for finding the spectral density function for surface atoms [190] has been used. The method requires a finite range of the applied potential and therefore, the potential has been cut off at the range equal to λ and shifted in order to avoid a potential step.
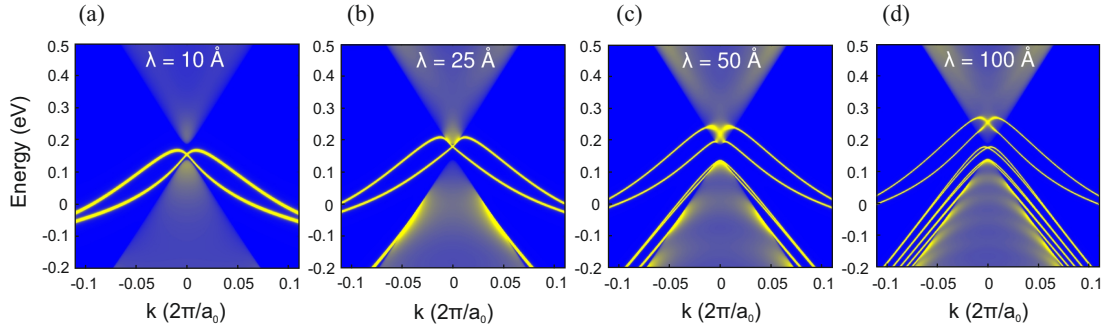
Figure 5.13: *Tight binding calculation af the surface spectral density of states of $Pb_{0.54}Sn_{0.46}$Te (111) as a function of screening length λ varying from 10 to 100Å, while the surface potential of $V_0 = +0.3$ eV and $T = 200$ K was kept constant. The solid lines correspond to the surface states and the shaded regions to the bulk bands.*

It has been checked that further increase of the range influences the obtained densities only negligibly. The results have been compared with experiment. The most accurate agreement was achieved for $\lambda = 25$ Å. To illustrate the dependence of the spectral density on the screening length λ we show in Fig. 5.13 the results obtained for four different λ values and fixed $V_0 = +0.3$ eV. It can be seen that with increasing width λ of the depletion layer underneath the surface the position of the Kramers point shifts upwards and the number of localized bands increases. At $\lambda = 50$ Å the Kramers point of the surface state is shifted into the bulk conduction band and a second subband appears in the VB. At $\lambda = 100$ Å even a third subband appears. Since we do not see such additional subbands in the ARPES measurements, we conclude that the Thomas-Fermi screening length must be well below 50 Å in our samples.

In Fig. 5.14 we present the temperature dependence of the TB calculations for the anion terminated (111) surface of $Pb_{0.54}Sn_{0.46}$Te with applied surface potential $V_0 = +0.2$ eV and $\lambda = 25$ Å. Comparing Fig. 5.14 with Fig. 5.4 we have seen that in both cases the gap closes at 110 K. Below 110 K the band gap opens up and the electronic band structure is inverted. Together with reopening of the band gap also a gap in the Kramers point opens. The band above the Kramers point becomes now the lower part of the Dirac cone and the band below the Kramers point forms the upper band of the new Rashba pair. The lower part of Figs. 5.14 (e–h) shows the in-plane spin polarization of the bands where the green and red colors indicate opposite spin directions. Upon band inversion the spin chirality of the Rashba pair is opposite to the one in the trivial case. The Dirac cone is highly deformed by the Thomas-Fermi potential, which shifts the Dirac point to the position, where it appears to hybridize with the conduction band.
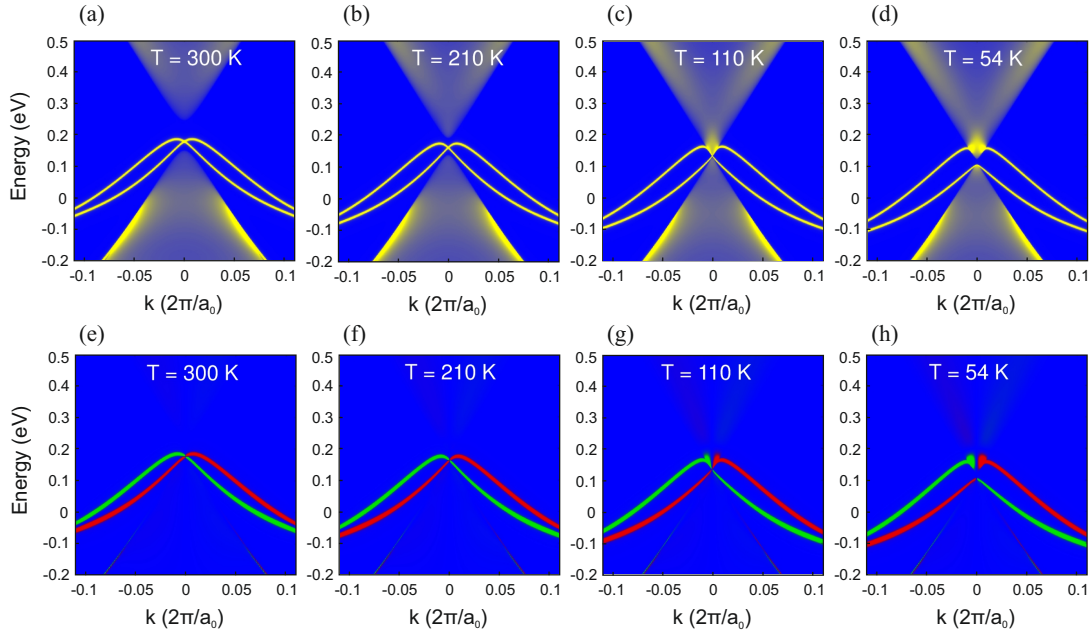
Figure 5.14: *Tight binding surface spectral density (top) and in-plane spin polarization (bottom) of the spectral density of states in (111) $Pb_{0.54}Sn_{0.46}Te$ as a function of temperature with surface potential $V_0 = +0.2\ eV$ and $\lambda = 25\ Å$. The solid lines correspond to the surface states and the shaded regions to the bulk bands and the red and green color to opposite in-plane spin polarization direction*

Summary

In this chapter we have shown temperature and Sn concentration dependent band inversion in $Pb_{1-x}Sn_xTe$. We have also shown that Bi- and Sb-doped topological crystalline insulator $Pb_{1-x}Sn_xTe$ (111) films represent a giant Rashba system that features a Rashba parameter as high as the record values reported in the literature. Contrary to most other systems, the strength of the Rashba effect is effectively controlled by the bulk doping. A detailed analysis using tight binding calculations reveals that it originates from a large upward band bending at the surface due to electron surface traps, whose occupancy is controlled by the bulk Fermi level. Since the Fermi level can be also tuned by electrostatic gates, this opens up a pathway for spintronic field effect device applications. Doping also allows compensating the intrinsic p-type character of TCI materials, resulting in high carrier mobilities that enable optical and topological quantum transport investigations otherwise screened by the bulk contribution. The magnitude of spin splitting seems already sufficient for certain room temperature device operation, where one may still need $\Delta k_R > 0.1$ Å^{-1} and $E_R > 200$ meV for downsized channel lengths of a few nanometers, but the observed trend implies that it can be even further enhanced by higher doping levels. Thus, our findings open up new

avenues for exploring exotic electrical and optical phenomena in topological systems as well as novel spintronic devices driven by the Rashba effect.

Chapter 6

Gapped Surface State in Mn-induced Bi$_2$Te$_3$ Heterostructures

The $\mathbb{Z}_2$ topological insulator doped with ferromagnetic materials enables the observation of the quantum anomalous Hall effect (QAHE), which provides quantized edge states for dissipationless charge transport applications [52, 53, 191–198]. We have qualitatively discussed the fundamentals of QAHE in chapter 2.5. The existence of quantized edge states, which are hosted by a magnetic energy gap at the Dirac point of topological surface states have not yet been successfully observed by any direct experimental measurement [192]. The crucial point here is the size of this gap which is considered to be the clue to overcome the present limitations of the QAHE due to its influence on realizing high temperature QAHE. So far this occurs only at temperatures one to two orders of magnitude below its fundamental limit set by the ferromagnetic Curie temperature T_{C} [197, 198]. The limitation for such low temperature QAHE is that when the temperature increases it smears out the transport properties of the edge state due to the thermally activated dissipative channels from the surface state and the bulk bands [199]. For our current research we employ our 1^3 ARPES setup equipped with low temperature measurement down to 1 K to determine the magnetic gap of Mn-doped Bi$_2$Te$_3$ films which opens only below T_{C} . Surprisingly, our analysis reveals large gap sizes of up to $\sim$ 90 meV, which not only exceeds $k_{\mathrm{B}}T$ at room temperature but is also 5 times larger than predicted by density functional theory [200]. It turns out such enhancement of the energy gap is due to the remarkable structure modification induced by Mn doping. Instead of a disordered impurity system, it forms an alternating sequence of septuple and quintuple layer blocks, where Mn is predominantly incorporated in the center of the septuple layers. A recent prediction shows that this self-organized hetero-structure substantially enhances the wave-function overlap between the Mn 3d states and the topolog-

ical surface state (TSS). This increases with the size of the magnetic gap at the Dirac point of the TSS [201]. Mn-doped Bi_2Se_3 forms a similar heterostructure, however, in this case only a large, albeit nonmagnetic gap is formed. We explain both differences based on the higher spin-orbit interaction in Bi_2Te_3 with the most important consequence of a magnetic anisotropy perpendicular to the films, whereas for Bi_2Se_3 the spin-orbit interaction it is too weak to overcome the dipole-dipole interaction which originates from the long range Coulomb interaction. The dipole-dipole interaction gives rise to the in-plane magnetic anisotropy of Mn doped Bi_2Se_3. Our findings which was already published in the Journal Nature [1] [202] provide crucial insights for pushing the lossless transport properties of topological insulators towards room-temperature applications. In the current context of the thesis we have only included the ARPES measurements for both Mn-doped Bi_2Te_3 and Bi_2Se_3 system. We will discuss these measurements and the relevant magnetic and non-magnetic gaps for the systems respectively. Readers are further encouraged to consult reference [202] for magnetic properties and structural characterization by EXAFS, XANES, and TEM.

6.1   Magnetic or Non-Magnetic Band Gap?

As we have discussed already in the introductory chapter 2, the quantum anomalous Hall effect (QAHE) is characterized by a quantized Hall resistance $\rho_{xy} = h/(\nu e^2)$ where ν is an integer number of gapless 1D edge states and which does not require the presence of an external magnetic field [191, 192]. Magnetically doped 3D topological insulators of the tetradymite family [192] have led to the first demonstration of the QAHE in Cr-doped (Bi, Sb)$_2$Te$_3$ [53, 193–196]. Initially the quantization was only approximately measured and also the longitudinal resistance did not vanish. Later on, the replacement of Cr by V as magnetic dopant delivered the first precise quantized values for ρ_{xy} as well as a vanishing ρ_{xx} at zero magnetic field [197, 198], which is the key signature for loss-less charge transport through edge channel devices [203]. A crucial issue which would help to understand and develop the QAHE further towards applications has, however, remained fundamentally open – the existence and quantification of the magnetic gap at the Dirac point [192].

In the present context of this chapter, we will elaborate the concept of observing QAHE in a magnetic topological insulator which occurs in the following way [192]: Firstly, in a thin-film geometry, the topological surface states of top and bottom surface interact, resulting in a hybridization gap. This gap has been found to be inverted in an oscillatory way with the

thickness for Bi_2Se_3 and Bi_2Te_3 [204]. Secondly, the exchange splitting can modify the band inversion of one spin subband. In the case that the bands are inverted, it can release the inversion, if they are not inverted, a sufficiently large exchange interaction will invert one of the spin subbands [192]. While the hybridization gap has impressively been demonstrated by angle-resolved photoemission (ARPES) [205–207], the exchange splitting is still outstanding. The exchange splitting manifests itself as a quantized Hall conductance e^2/h with topological invariant characterized by finite Chern number for 2D material. However, for 3D material it gives rise to a magnetic gap at the Dirac point of the topological surface state. This gap is therefore a crucial parameter for the temperature at which the QAHE can be observed. This temperature is at present very low, about 50 mK [198] with one work reporting 1 to 2 K for Cr-doped $(Bi, Sb)_2Te_3$ [208] and thus one or two orders of magnitude lower than the ferromagnetic $T_C \sim 30$ K of the systems. First principles calculations have recently suggested that the magnetic gap can be enhanced in topological insulator heterostructures [201].

Angle resolved photoemission spectroscopy (ARPES) is the method of choice for the direct observation of the magnetic gap and the verification of these predictions. Nevertheless, the experimental situation appears confusing: Large gaps at the Dirac point of the order of 0.05–0.2 eV of Bi_2Se_3 doped with Mn [103, 180, 209] were explicitly shown to be *not* of magnetic origin [180]. On the contrary, no gaps are observed for Bi_2Se_3 when magnetic impurities are deposited directly on its surface [180, 210–212]. Also, no gap appears when Mn is doped in the bulk of Bi_2Te_3 where the Dirac cone was found to remain intact down to temperatures of 12 K [213]. For V-doped Sb_2Te_3 a mobility gap of 32 meV was inferred from scanning tunneling Landau level spectroscopy at 1.3 K in comparison to pure Sb_2Te_3 [214], but due to the strong overlap with magnetic impurity states, no gap could be observed in the local density of states and no correlation to magnetism was reported. For Cr-doped $(Bi, Sb)_2Te_3$ an average gap of 56 meV was found by tunneling spectroscopy [215], but again its origin remained elusive because no temperature dependence was found. On the other hand, a gap as large as $\sim$75 meV was found for Bi_2Se_3 with 4% Cr by ARPES *even at room temperature* [216]. This clearly suggests a non-magnetic origin of the effect because the ferromagnetic T_C is well below 50 K in all of these systems.

Interestingly, the nature of the magnetic doping is remained under debate also. For isovalent doping, it was predicted that Bi_2Se_3, Bi_2Te_3 and Sb_2Te_3 will form a QAHE state. Thus, this should occur for doping with Cr or Fe and as well as for Ti or V, however, for later the systems it was predicted to become metallic and not suitable for the QAHE [192]. The fact that so far, V-doped $(Sb,Bi)_2Te_3$ displays the highest QAHE temperatures shows that the situation is more complex. In particular, non-isovalent magnetic dopants turn out to surprisingly little affect the Fermi level and carrier concentration. For example, Mn-doped Bi_2Se_3 and Bi_2Te_3 always remain n-type [180, 213] despite the fact that divalent Mn

replacing trivalent Bi should act as a strong acceptor. These puzzling issues are related to the comparatively complex tetradymite lattice structure consisting of quintuple layers separated by van der Waals gaps that allows a distribution of the dopants over a large number of electrically and magnetically inequivalent incorporation sites within the huge tetradymite unit cell consisting of thirty individual atoms [202]. Hence, the actual magnetic dopant distribution is a key for understanding their impact on magnetism and band topology of the system.

To resolve these issues, we present here a comprehensive study of Mn-doped Bi_2Te_3 and Bi_2Se_3 films grown under essentially identical conditions. Our data unequivocally reveals a pronounced magnetic exchange splitting at the Dirac point in Bi_2Te_3, by far exceeding previous theoretical calculations [200]. It vanishes above the ferromagnetic Curie temperature and it displays a ferromagnetic out-of-plane spin texture being clear cut evidence for its magnetic origin [202]. On the other hand, no increase in the gap size could be identified for the related system Mn-doped Bi_2Se_3 down to 1 K, far below T_C.

6.1.1   ARPES on Bi_2Te_3

Mn-doped Bi_2Te_3 and Bi_2Se_3 layers were grown by molecular beam epitaxy on $BaF_2(111)$ substrates using a Riber 1000 and a Varian GEN II MBE system by our collaborators at JKU, Linz. Compound Bi_2Te_3 and Bi_2Se_3, as well as elemental sources for Mn, Te and Se were employed for control of stoichiometry and composition. Deposition was carried out at a growth temperature of 330°C for Bi_2Te_3 and 360°C for Bi_2Se_3 to obtain perfect 2D growth independent of dopant concentrations. Details on the growth procedures were previously reported [180, 213]. The samples were immediately capped in situ after growth with amorphous Se and Te capping layers at room temperature to protect the surface against oxidation. This cap was removed just before the ARPES experiments by *in situ* sputtering and annealing procedure.

The ARPES experiments were performed at the ARPES-1[3] end station at the UE112-PGM2b undulator beam line. The lowest measurements temperature in this setup is 1 K. The experimental geometry has the following characteristics: With the central axis of the analyzer lens and the polar rotation axis of the sample defined as the x and z axes of a spherical coordinate system, the photons arrive from the direction with $\phi = 45°$ azimuthal, and 84° polar angles. The light polarization is horizontal (along x). The entrance slit of the hemispherical analyzer is placed parallel to the z-axis. The measurements at $h\nu = 50$ eV were performed with 10 meV energy resolution.

Mn-doped Bi_2Te_3 ARPES dispersions of the Dirac cone were measured above and below the ferromagnetic phase transition of $T_C = 10$ K and shown in Fig. 6.1. There is almost no difference between 20 K (a) and 1 K (b). However a fit of the upper Dirac cone in Fig.
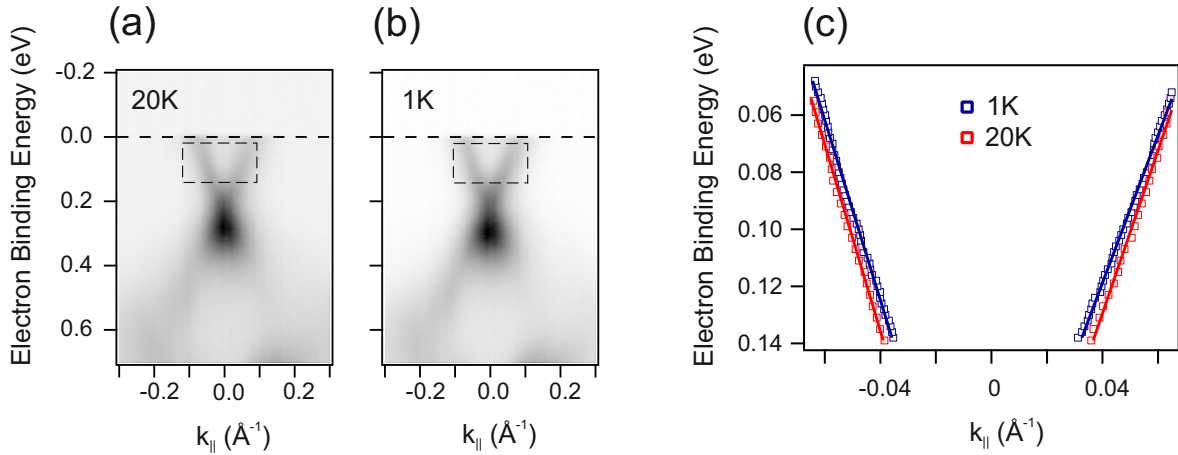
Figure 6.1: Magnetic gap of Mn-doped Bi$_2$Te$_3$ derived by ARPES. *(a,b) Measurements for Bi$_2$Te$_3$ with 6% Mn performed above and below the Curie temperature $T_C \sim 10$ K. (c) Momentum distribution fitting of the upper Dirac cone shows the shrink along $k_\parallel$ at 1K represents the signature of gap opening.*

6.1 (c) reveals the shrinking of the Dirac cone in the momentum space as a signature of an energy gap. The photoemission spectrum from the center of the surface Brillouin zone in Fig. 6.2 shows an intensity maximum at ~ 0.3 eV due to bulk transitions (50 eV photon energy), while the Dirac point (E_D) of the surface state contributes a smaller peak at ~ 0.2 eV binding energy. Upon cooling of the sample from 20 K through T_C down to 1 K, the low-binding energy flank of the peak develops a pronounced shoulder. This is consistent with the shrinking of the upper Dirac cone in the momentum space in Fig 6.1(c). The widening of the Dirac point forms a plateau around 0.2 eV, as can be seen in Fig. 6.2(c). The temperature-dependent leading edge shifts in Fig. 6.2 and Fig. 6.3 are obtained by approximating the photoemission intensity in the indicated ranges with a line. The slope of this line is constrained to be identical for the low and high temperature spectra within the same section. The obtained shifts (S1 ~ 21 meV, S2 ~ 12 meV) give a lower limit for the splitting at 1 K of ~ 33 meV. Assuming that a single component for the topological surface state at 20 K becomes split into two equally intense components at 1 K shown in Fig. 6.2(d), we arrive at a gap Δ which is $2.5 - 3$ times larger or 90 ± 10 meV at low temperature. Because the ferromagnetic T_C amounts to ~ 10 K in this sample, this proves the magnetic origin of this gap. This is the central result of this work.

It is confirmed when the Mn content is increased to 10% in a second sample as shown in Fig. 6.3. The lower limit of the magnetic splitting remains 33 meV, and also the energy of the Dirac point remains the same. However, the spectrum changes markedly, especially the strong intensity enhancement near the Fermi energy is indication of the direct interaction of Mn 3d states without magnetic splitting. (Note that the exchange splitting of the Mn 3d states is roughly 1 eV per Bohr magneton and therefore much larger than the figure range.)

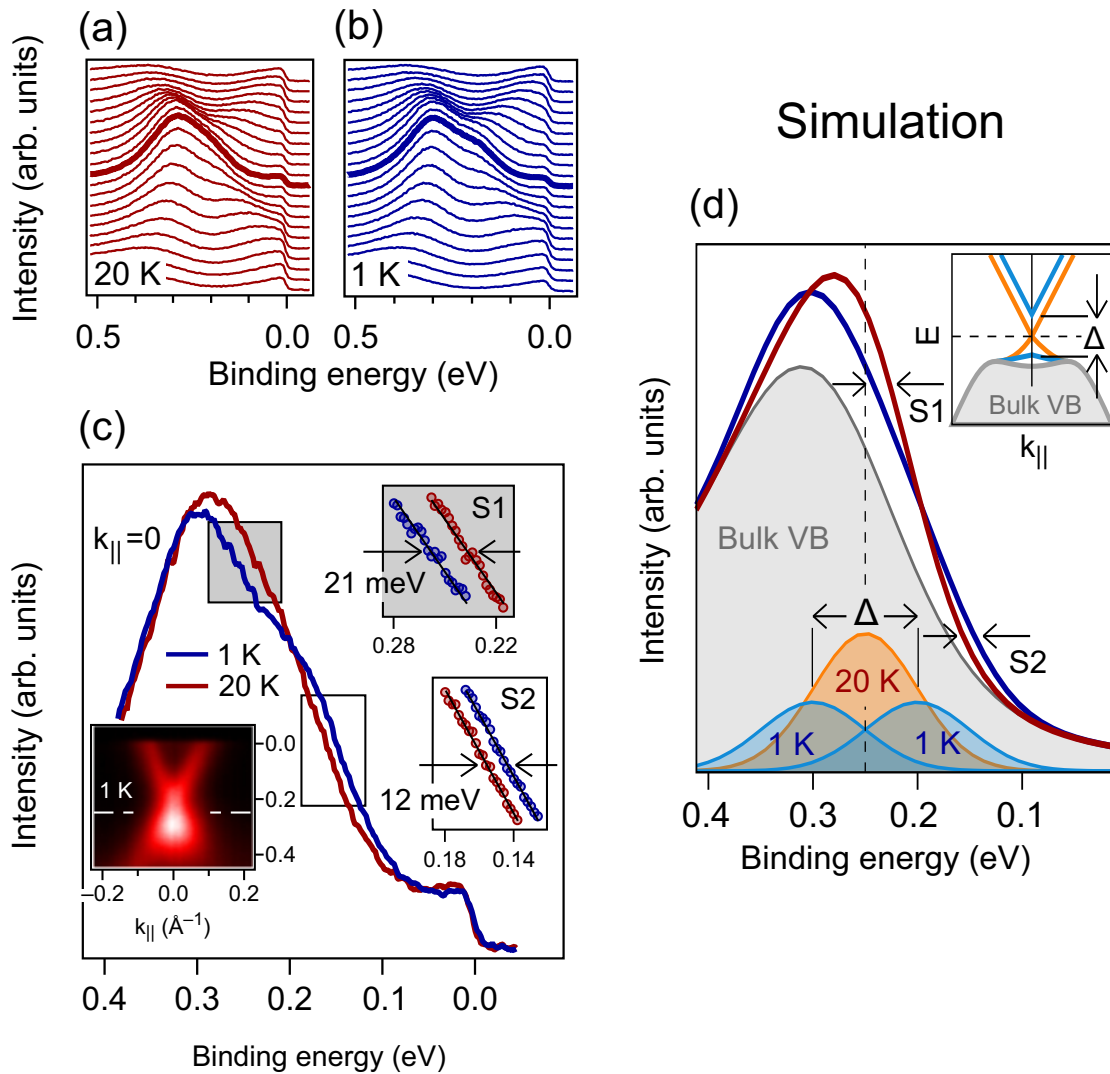**Figure 6.2:** *(a,b) EDCs derived from the ARPES data in Fig. 6.1. Thick lines correspond to the EDC at the center of the surface Brillouin zone, i. e., electron wave vector component $k_{\parallel} = 0$ Å^{-1}. Line fits to the regions S1 and S3 indicated in (c) yield a splitting of at least 33 eV between 20 K and 1 K. (d) Simulation showing that this corresponds to a magnetic gap $\Delta = 90 \pm 10$ meV.*
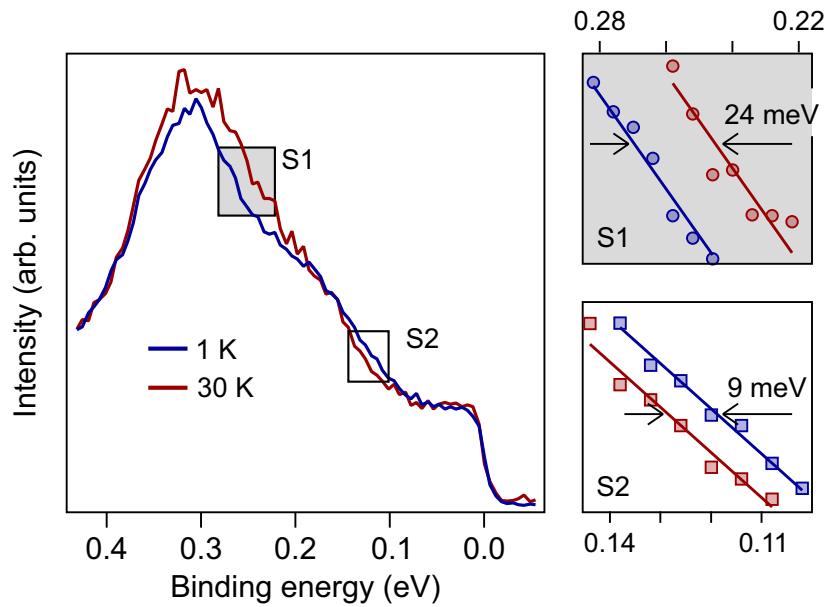
Figure 6.3: *ARPES for a 10% Mn doped Bi$_2$Te$_3$ thin film. The normal emission spectra displayed on the left hand side recorded at 1 and 30 K show a significant redistribution of spectral weight around the binding energy of $\sim$ 180 meV when crossing the ferromagnetic transition at T_C = 12 K. The shifts in the regions marked **S1** and **S2** displayed on the right hand side on a magnified scale are of similar magnitude as seen for the 6% Mn-doped case presented in Figure 6.2, and are compatible with a $\sim$ 100 meV gap opening at the Dirac point. ARPES was measured with p-polarized light and $h\nu$ = 50 eV.*

Because the ARPES samples are prepared by a decapping procedure, it cannot be excluded that this is due to Mn clustering at the surface.

The localized magnetic moments of the Mn are ferromagnetically coupled through p-electrons of the host material Bi_2Te_3. The present experiment probes the magnetism of these p-electrons, and we can compare it to another experiment where ARPES has been successful in probing the ferromagnetic interaction of localized moments on a larger energy scale: In Gd metal, ferromagnetic exchange is mediated through the Gd $5d$ electrons. In ARPES, the Gd $5d$ band splits by 0.85 eV when the temperature is lowered from 1.02 T_C to 0.27 T_C ($T_C = 293$ K for bulk Gd) [217]. In the present experiment, we probe the split Dirac point well below the Curie temperature at 0.1 T_C. As we can assume intuitively, the unordered magnetic moments in the bulk do not open a gap at the surface. The gap at the Dirac point is expected to be proportional to the exchange coupling J and magnetization M in the z-direction [218].

6.1.2   ARPES on Bi_2Se_3

Here we will discuss the ARPES measurements of Mn-doped Bi_2Se_3 with similar concentration of 6% for 20 K and 1 K. In contrast to Mn-doped Bi_2Te_3, the Mn-doped Bi_2Se_3 shows a large band gap at the Dirac point. Fig. 6.4(a,b) shows the ARPES measurement at 20 K and 1 K respectively and corresponding momentum distribution curves (MDCs) are shown in Fig. 6.4(c,d). Parabolic fitting of the upper and lower Dirac cone of gapped surface states is shown in Fig. 6.4(e). The large gap of Mn-doped Bi_2Se_3 does not increase further when cooling below T_C (~ 6 K in contrast to $T_C \sim 10$–12 K for Mn-doped Bi_2Te_3) shown in Fig. (f), and corresponding estimated gap size at the Dirac point is ~ 200 meV. The energy band gap remains unchanged already in the range between 300 and 12 K which has been extensively shown by Sánchez-Barriga et al. in Ref. [180]. This excludes a potential magnetic contribution to the large gap at the Dirac point in Mn-doped Bi_2Se_3.

6.2   Ferromagnetic Origin of the Gapped Surface State

Several DFT calculations of the electronic structure of transition metal impurities at the surface and in the bulk of Bi_2Te_3 and Bi_2Se_3 have been published, focusing on various aspects. A $\sim$10 meV magnetic band gap has at first been predicted for Co-doped Bi_2Se_3 [219] and 16 meV were found for Mn-doped Bi_2Te_3 [200]. We mentioned above that by the splitting of the Dirac point we probe the exchange interaction at the Te. This has also been confirmed by DFT, where the spectral density of the split Dirac point is by nine times more strongly localized at the Te than at the other sites [200]. The calculation of 16 meV by Henk et al. [200], which assumes magnetization perpendicular to the surface, corresponds to a Mn concentration of $x= 10\%$ in our present notation $(Bi_{1-x}Mn_x)_2Te_3$. However, the
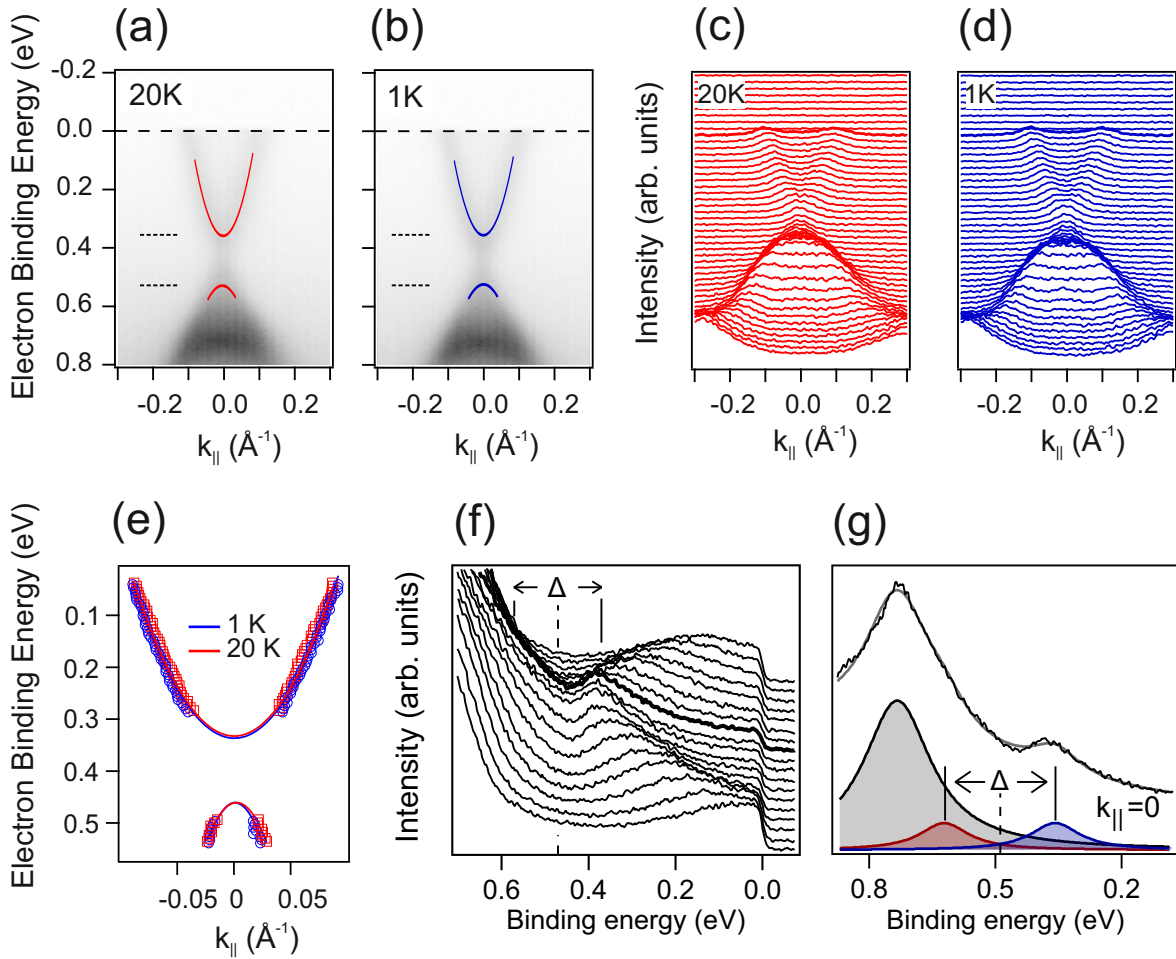
Figure 6.4: *Temperature dependence ARPES measurements for Mn-doped Bi$_2$Se$_3$ with ~ 6 % Mn measured with 50 eV photon energy reveals only a temperature independent nonmagnetic gap Δ that is not correlated with the magnetization. **(a),(b)** ARPES spectra measured at 20 K and 1 K, above and below of the ferromagnetic Curie temperature respectively. **(c),(d)** Corresponding MDCs derived from the ARPES spectra. **(e)** Comparison of the MDC fit of the upper cone and lower cone at 20 K and 1 K showing the exact same energy gap, which signifies its non-magnetic origin. **(f),(g)** EDC plot of the ARPES spectra measured at 1 K and corresponding fit of the EDC at normal emission.*

calculated gap is substantially smaller that the magnetic gap of up to 90 meV revealed by our experiments.

Now we turn to the case of Mn in Bi_2Se_3. A nonmagnetic band gap of the measured size ($\sim$ 200 meV) does not appear in any DFT calculation. At least, the calculations reveal principally that, depending on orbital symmetry, gaps in the Dirac cone open due to hybridization with transition metal impurity states. For example, a hybridization gap of ~ 4 meV opens at the Dirac point of substitutional Mn in Bi_2Se_3 for in-plane (not out of plane!) magnetization [220]. The only prediction of a nonmagnetic gap of the measured order of magnitude is from model calculations assuming an on-site Coulomb interaction U at the impurity site [221, 222].

Further structural studies quite clarify this question of the nonmagnetic gap: Mn-doped Bi_2Te_3 (Bi_2Se_3)creates a novel structure composed of septuple and quintuple layers instead of the expected periodic sequence of Te-Bi-Te-Bi-Te quintuple layers. The septuple layers consist of the sequence Te-Bi-Te-Mn-Te-Bi-Te, where the Mn atoms occupy the center of the septuple. Apparently, the Mn forms more impurity sites in Bi_2Se_3 than in Bi_2Te_3 where more Mn is incorporated into the septuple layers [202].

Mn in the impurity site will lead to larger Coulomb U than in the central Mn monolayer where Mn $3d$ levels can delocalize in the plane. We could experimentally demonstrate recently that U, termed previously the impurity strength [221, 222], influences the size of the nonmagnetic gap strongly. The efficiency of gap opening is strongly enhanced by In impurities [100]. Comparing Mn with In doping it was found that to reach in Bi_2Se_3 the same gap size as 8% Mn (~ 200 meV), only 2% In are required [180, 223]. However, there is another important factor: It was recently shown that the effect of impurities on the nonmagnetic gap reduces with higher spin-orbit interaction of the host material [223]. Therefore the Bi_2Te_3 is principally less susceptible to the opening of a nonmagnetic gap than Bi_2Se_3, regardless of the structural differences induced by the Mn.

Otrokov et al. very recently studied hypothetical structures that are very similar to the ones studies in the present work [201]. In their DFT calculations, the Mn-induced septuple layer with $MnBi_2Te_4$ stoichiometry has been combined with Bi_2Te_3 quintuple layers in several different heterostructures. The magnetic anisotropy is in all these cases predicted to be perpendicular to the layers. It is well known that the higher spin-orbit interaction in Bi_2Te_3 leads to warping effects in the Dirac cone which turn the spin out of the plane [224]. One question left open from Otrokov et al.'s work is whether these effects explain the difference between Mn-doped Bi_2Te_3 and Bi_2Se_3. Collaborators from theory compared directly Bi_2Te_3 to Bi_2Se_3 for a periodic structure with 1 septuple layer Bi_2MnX_4 and 1 quintuple layer Bi_2Se_3(X=Te, Se) [202]. It was found that the dipole-dipole interaction which tends to align the magnetic moments in the plane is very similar for the two systems. However, the magnetocrystalline anisotropy is 3.5 times larger in the telluride. Including the shape

anisotropy from dipole-dipole interaction, the telluride has an order of magnitude larger anisotropy than the selenide which almost changes sign towards in-plane magnetization. To explain why the expt. shows the in-plane magnetization it is assumed that it may be triggered by the substantial fraction of Mn at substitutional impurity sites which, according to Abdalla et al., support in-plane anisotropy [220]. Most important to note is that the higher spin-orbit interaction in the telluride is able to overcome the dipole-dipole interaction in the heterostructure, and this enables the formation of the magnetic gap at the Dirac point.

We mentioned above that the measured size of the magnetic gap, 90 meV, is five times as large as predicted by Henk et al., 16 meV, at comparable Mn concentration (5% in Henk et al., 4% and 6% in the present experiment). Otrokov et al. pointed out that their ficticious full Mn monolayer at the center of $MnBi_2Te_4/Bi_2Te_3$ would enhance the wave function overlap strongly [201]. Magnetic gaps between 38 and 77 meV are predicted for various combinations of $MnBi_2Te_4$ and Bi_2Te_3, i. e., the system discovered in the present work. Moreover, Otrokov et al. have confirmed that these heterostructures do not alter the nontrivial topology of the Bi_2Te_3. One indication for this is the persistence of the Dirac cone surface state. This is clearly displayed by ARPES. Moreover, it is confirmed by a calculation of the Chern number where $C = -1$ was obtained for the sandwich system consisting of $MnBi_2Te_4$/(2 quintuple layers Bi_2Te_3)/$MnBi_2Te_4$ [201]

Summary

In conclusion, we have demonstrated the opening of a magnetic gap in a topological insulator below the ferromagnetic phase transition and its closure for $T > T_C$. The magnetic gap in Mn-doped Bi_2Te_3 is remarkably large (90±10 meV) as a result of the formation of a natural heterostructure in which Mn is incorporated within septuple layers instead of simple substitutional incorporation. Our results thus support recent theoretical predictions that magnetic gaps in topological insulators can be significantly enhanced in multi-layered systems [201]. No magnetic gap is detected for Mn-doped Bi_2Se_3 within the experimental resolution but instead, a very large non-magnetic gap that does not increase even when cooling down to 1 K, well below T_C, and thus does not have a magnetic contribution. We correlate this with the difference in magnetic anisotropy due to the much larger spin-orbit interaction in Bi_2Te_3 and offer a unifed picture for both observations.

Summary

This thesis is focused on studying the surface band gap in newly discovered topological states of matter. Opening an energy gap of magnetic or non-magnetic origin could provide crucial fundamental knowledge as well as exciting future technological applications. We employ angle resolved photoemission spectroscopy technique to study the electronic band structure of topological crystalline insulators and $\mathbb{Z}_2$ topological insulators in different temperature range.

The first part of this thesis introduces the theoretical concept of topological insulators. It starts from the classification of metal and insulator within the band theory picture which essentially proved to be insufficient to explain the quantum Hall effect. This led condensed matter physicist to discover the concept of the topological invariant to classify solid state materials. It is explained how the strong spin-orbit coupling without external magnetic field can drive a system into a topologically non-trivial phase giving rise to the quantum spin Hall effect in a two dimensional system protected by the time reversal symmetry. This concept can be extended to 3D material, which is called $\mathbb{Z}_2$ topological insulators (TI), and $Bi_{1-x}Sb_x$ alloys as an example of the first experimental realization are discussed. Extending the search for topological insulators beyond time reversal symmetry gives rise to the discovery of topological crystalline insulators (TCI) protected by crystal mirror symmetry. the theoretical description of the quantum anomalous Hall effect by spontaneous breaking of the time reversal symmetry is also discussed in the second part of the chapter 2 followed by the discussion of the Rashba effect by spontaneous breaking of the structural inversion symmetry at the crystal surface.

In the following chapter 3, we introduce the methodological background of the angle resolved photoemission spectroscopy (ARPES) technique which turns out to be an excellent tool to probe the topological surface state in great detail. In the context of this thesis we discuss the corresponding experimental setup equipped with excellent energy resolution and angular resolution to distinguish between the bulk and the surface states as well as determining the energy gap at the Dirac point of the topological surface state. The importance of the synchrotron radiation facility BESSY-II as a brilliant light source is also mentioned in this chapter.

The results part starts with chapter 4 which focuses on studying the topological phase

transition in the $Pb_{1-x}Sn_xSe$ System. The epitaxial growth of $Pb_{1-x}Sn_xSe$ (111) samples with different Sn concentration is presented. Subsequent temperature dependent ARPES measurements systematically probe the transition with temperature from trivial to topological crystalline insulator phase in this system. Choosing Bi as an electron donor compensates the intrinsic hole doping in this IV-VI semiconductor system. This tunes the Fermi level into the conduction band and is required to study the properties of the surface states. This thesis shows the first experimental observation of a new type of phase transition from TCI to $\mathbb{Z}_2$ topological insulator in the $Pb_{1-x}Sn_xSe$ system with $x_{Sn}= 28\%$ doped with 2.2% Bi. The phase transition attributes are the even number of band inversions in the Brillouin zone of TCI and the odd number of band inversions of the $\mathbb{Z}_2$ TI. We address the role of Bi doping as the decisive ingredient for the unconventional phase transition. Higher covalency of Bi contributes to the structural symmetry breaking with a sublattice shift which is responsible for ferroelectricity. The sublattice shift typically also leads to a rhombohedral distortion which triggers the TCI –to – $\mathbb{Z}_2$ topological phase transition.

In chapter 5, we show systematic studies of the TCI phase transition in the $Pb_{1-x}Sn_xTe$ system with temperature and Sn concentration. Contrary to the Bi doping in $Pb_{1-x}Sn_xSe$, this chapter reveals that $Pb_{1-x}Sn_xTe$:Bi shows a giant Rashba effect featuring a Rashba parameter as high as the record values reported in the literature. Similar behavior is observed in $Pb_{1-x}Sn_xTe$ (111) films doped with Sb, as group V n-type dopant. The observed Rashba effect can only be effectively controlled by bulk doping of the system. Tight binding calculations reveal that the respective Rashba effect originates from a large upward band bending at the surface due to electron surface traps, whose occupancy is controlled by the bulk Fermi level. These findings hopefully open up new avenues for exploring exotic electrical and optical phenomena in topological systems as well as novel spintronic devices driven by the Rashba effect.

Chapter 6 of this thesis discusses the experimental observation of the quantum anomalous Hall effect by spontaneous breaking of the time reversal symmetry. For the first time the opening of an energy gap of magnetic origin is demonstrated in a topological insulator. The magnetic gap in Mn-doped Bi_2Te_3 is remarkably large (90±10 meV) which is due to the formation of a natural heterostructure. Here the decisive factor is the Mn doping which is incorporated within septuple layers instead of a simple substitutional incorporation. In the same spirit it is shown that the Mn-doped Bi_2Se_3 system shows no magnetic gap but instead, a very large non-magnetic gap appears at the Dirac point of the topological surface state. The nonmagnetic origin of the gap in Mn doped Bi_2Se_3 is revealed by the unchanged nature of the gap when the system is cooled down to 1 K, well below the T_C. This correlates with the difference in magnetic anisotropy due to the much larger spin-orbit interaction in Bi_2Te_3 compared to Bi_2Se_3.

Kurzfassung

In der vorliegenden Studie verwenden wir die Methode der winkelaufgelösten Photoemissionsspektroskopie (ARPES) zur Untersuchung der elektronischen Struktur von topologischen Zuständen der Materie. Insbesondere die sogenannten topologischen kristallinen Isolatoren (TCI) $Pb_{1-x}Sn_xSe$ und $Pb_{1-x}Sn_xTe$ sowie die Mn-dotierten $\mathbb{Z}_2$ topologischen Isolatoren (TI) Bi_2Te_3 und Bi_2Se_3. Die $\mathbb{Z}_2$-Klasse der starken topologischen Isolatoren ist durch Zeitumkehrsymmetrie geschützt und durch eine ungerade Anzahl metallischer Dirac-Oberflächenzustände in der Oberflächenbrillouinzone gekennzeichnet. Die topologischen kristallinen Isolatoren hingegen sind durch einzelne Kristallsymmetrien geschützt und weisen eine gerade Anzahl von Dirac-Kegeln auf. Die topologischen Eigenschaften von Blei-Zinn-Chalkogenid-TCI lassen sich durch Temperatur sowie chemische Zusammensetzung einstellen. Hier wird gezeigt, dass Bi-Dotierung von eptiaktischen $Pb_{1-x}Sn_xSe(111)$-Schichten einen Quantenphasenübergang von einem topologischen kristallinen Isolator zu einem $\mathbb{Z}_2$-topologischen Isolator hervorruft. Dies geschieht, weil die Dotierung mit Bi die vierfache Valley-Entartung im Volumen aufhebt. Als Konsequenz entsteht eine Lücke bei $\overline{\Gamma}$, während die drei Dirac-Kegel an den $\overline{M}$-Punkten der Oberflächenbrillouinzone intakt bleiben. Wir interpretieren diesen neuen Phasenübergang als durch eine Gitterverzerrung verursacht. Unsere Ergebnisse erweitern das topologische Phasendiagramm enorm und machen starke topologische Isolatoren durch Verzerrungen oder elektrische Felder schaltbar. Im Gegensatz dazu induziert eine Bi-Dotierung im Volumen von epitaktischen $Pb_{1-x}Sn_xTe(111)$-Schichten eine riesige Rashba-Aufspaltung an der Oberfläche, die durch das Ausmaβ der Dotierung eingestellt werden kann. Tight-Binding-Berechnungen identifizieren ihren Ursprung in einem Fermi-Niveau-Pinning durch Trap-Zustände an der Oberfläche. Magnetisch dotierte topologische Isolatoren ermöglichen den quantisierten anomalen Hall-Effekt (QAHE), der quantisierte Kantenzustände liefert, die für verlustfreien Ladungstransport eingesetzt werden können. Die Kantenzustände treten in einer magnetischen Energielücke am Dirac-Punkt auf, die bisher noch nicht experimentell beobachtet wurde. Unsere Tieftemperatur-ARPES-Untersuchungen weisen die magnetische Energielücke in Mn dotiertem Bi_2Te_3 eindeutig nach. Unsere Analyse zeigt unterhalb von T_C eine viermal gröβere Energielücke als theoretisch vorhergesagt. Wir führen diese Erhöhung auf eine bemerkenswerte Strukturmodifikation durch die Mn-Dotierung zurück.

Statt eines Systems mit ungeordneten Mn Verunreinigungen entsteht eine selbstorganisierte alternierende Sequenz von $MnBi_2Te_4$-Septupel- und Bi_2Te_3-Quintupel-Schichten. Das erhöht den Überlapp der Wellenfunktionen und führt zu der groβen magnetischen Energielücke. Mn-dotiertes Bi_2Se_3 bildet ähnliche Heterostrukturen aus, jedoch wird in diesem System nur eine nichtmagnetische Energielücke beobachtet. Dies korreliert mit der unterschiedlichen magnetischen Anisotropie aufgrund der viel gröβeren Spin-Bahn-Wechselwirkung im Bi_2Te_3 im Vergleich zu Bi_2Se_3. Diese Resultate liefern entscheidende Erkenntnisse, um verlustfreien Transport in topologischen Isolatoren für Anwendungen bei Raumtemperatur weiterzuentwickeln.

Appendix A

$\mathbf{Pb}_{1-x}\mathbf{Sn}_x\mathbf{Se}$

The influence of Bi-doping on the structural properties of the epilayers was evaluated by high-resolution x-ray diffraction as shown by Figs. A.1. For Bi-concentrations as high as 2.2% (doping concentration of 3.5×10^{20} cm^{-3}) we do not find any indication of phase separation or secondary phase formation and no broadening of the diffraction peaks occurs shown in Fig. A.1(b). For further analysis of possible lattice deformations, reciprocal space maps were recorded around the (222) and (513) reciprocal lattice points as shown in Fig. 3 for two Pb$_0$.72Sn$_0$.28Se epilayers with high (2.2%) and low (<0.5%) Bi-doping. From the fit of the peak positions, the in-plane and out-of-plane lattice constants, as well as unit cell corner angle α (rhombohedral distortion) was derived using the relation:

$$\sin(\alpha/2) = a_{||}\sqrt{3}(2a_{\perp}^2 + 4a_{||}^2)^{-1/2} \qquad (A.1)$$

For low Bi-concentration the layers exhibit a cubic lattice structure with a corner angle $\alpha = 90°$ The experimental error in α is of $\pm 0.01°$, as derived from the error in the lattice parameter determination (± 0.001 $\mathring{A}$). For the high-Bi doped layers, however, a rhombohedral lattice distortion is found with $\alpha \sim 89.94°$ for n$_{Bi}$ = 2.2% as shown by Fig. 3d. This indicates that Bi-doping modifies the lattice structure and thus impacts the topological surface state in the presence of a rhombohedral distortion.

The doping action of Bi and the resulting electrical properties of the films were evaluated by Hall measurements of a large series of samples as shown in appendix Fig. A.3. For Bi-doped PbSe the measured electron concentration n$_H$ corrected for the background hole concentration p$_0$ increases linearly with Bi flux and therefore changes exponentially with Bi$_2$Se$_3$ effusion cell temperature (cf. Fig. A.3(a), ■), indicating a unity doping efficiency in agreement with the results for Bi-doped PbTe films [122]. This therefore provides a reliable calibration of Bi concentrations within a relative error of 10%. For Pb$_{1-x}$Sn$_x$Se films, the electron concentration n$_H$ – p$_0$ (Fig. A.3(b),♦) is generally found to be lower for the same
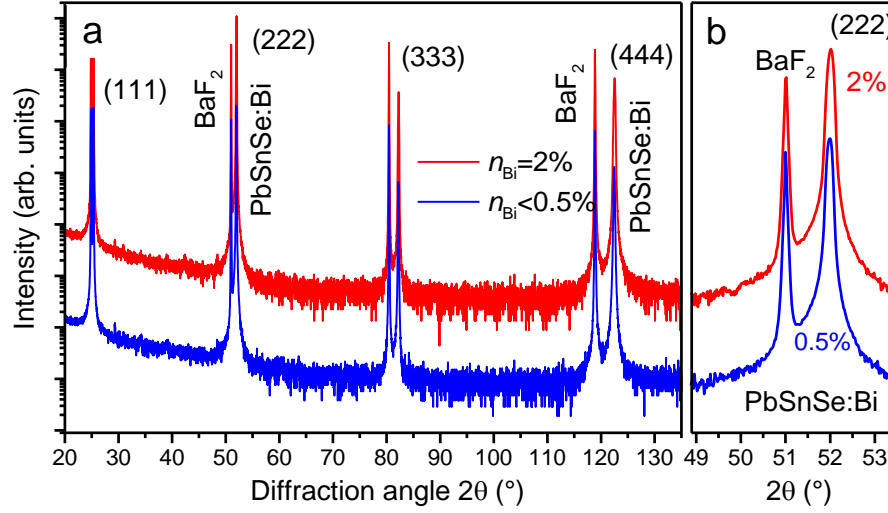
Figure A.1: Structural effect of Bi-doping of $Pb_{1-x}Sn_xSe$. *(a) X-ray diffraction spectra of two $Pb_{0.72}Sn_{0.28}Se$ layers with high and low Bi dopant concentration (blue: $n_{Bi} < 0.5\%$, red: $n_{Bi} = 2.2\%$), evidencing a single phase structure without any traces of secondary phases. (b) Zoom-in on the diffraction curves around the (222) Bragg reflection, evidencing no structural degradation due to Bi incorporation.*
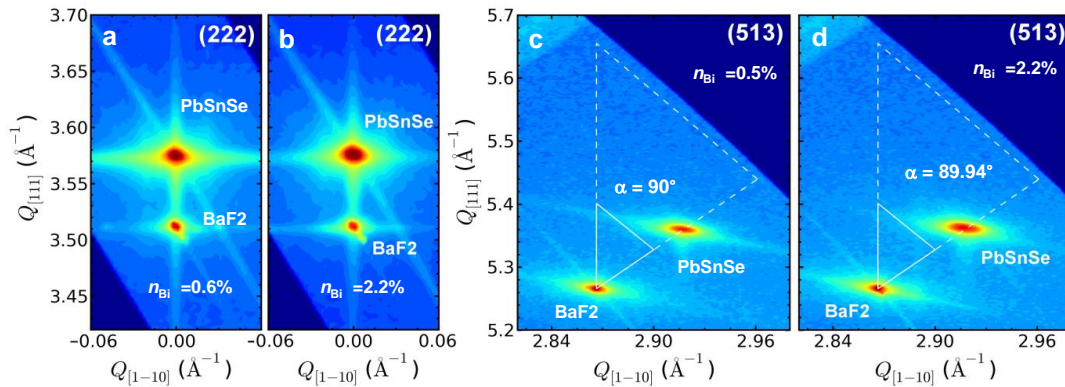

Figure A.2: X-ray diffraction reciprocal space maps: *two $Pb_{0.72}Sn_{0.28}Se:Bi$ samples doped with $n_{Bi} \sim 0.6\%$ (a, c) and nBi = 2.2% of bismuth (b, d), indicating a small rhombohedral lattice distortion for the latter with the distortion angle $\alpha = 89.94°$. The reciprocal space maps were recorded around the symmetric (222) and asymmetric (513) reciprocal lattice points at room temperature*

growth conditions. This indicates a reduced doping efficiency of Bi in PbSnSe compared to that in PbSe, in particular at higher doping concentrations. As shown in Fig. A.3(b), for small electron densities in the 10^{17} cm^{-3} range, the mobility of the epilayers at 77K is as high as μ 77K = 32000 cm^2/Vs for PbSe and 10.500 cm^2/Vs for Pb$_{0.72}$Sn$_{0.28}$Se . Due to the increased scattering the mobility rapidly decreases with increasing Bi-content in particular above the 10^{18} cm^{-3} level, as we have also previously reported for PbTe [122].
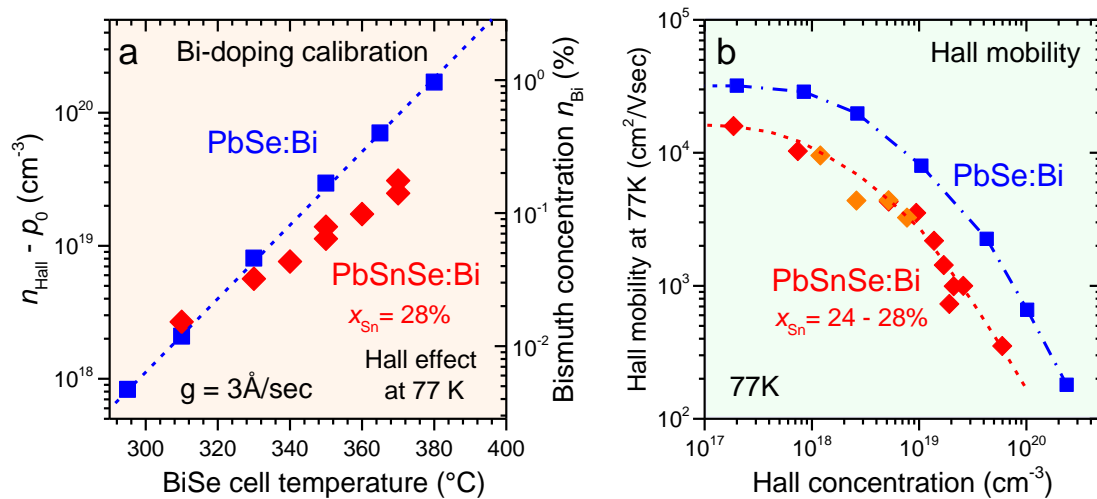

Figure A.3: Bi doping characterization and Hall effect transport measurements *at 77 K for PbSe:Bi (■) and PbSnSe:Bi with x_{Sn} = 28% (♦). (a) Effective electron concentration (n_{Hall}-p_0) versus Bi$_2$Se$_3$ effusion cell temperature used during MBE growth for a constant film deposition rate of 3Å/s. The background carrier concentration of undoped p-type reference layers due to cation vacancies was p_0=+2×10^{17} for PbSe and +8×10^{17} cm^{-3} for Pb$_{0.72}$Sn$_{0.28}$Se. The dashed line represents the values expected for unity doping efficiency. The lower carrier concentration observed for Pb$_{0.72}$Sn$_{0.28}$Se indicates a reduction of the doping efficiency with increasing Bi content, contrary to the behavior of PbSe. (b) Hall mobility of the epilayers versus carrier concentration. For low carrier concentrations, a saturation mobility of μ_{77K} = 32000 and 10500 cm^2/Vs is obtained for PbSe and Pb$_{0.72}$Sn$_{0.28}$Se, respectively.*

Appendix B

$\mathbf{Pb_{1-x}Sn_xTe}$

Structural characterization by high resolution X-ray reciprocal space mapping as shown in Figs. B.1, demonstrates that the layers with $1-2$ μm thickness are fully relaxed. Accordingly, their Bragg peaks lie exactly along the line connecting the bulk PbTe ($a_{PbTe}=$ 6.462) and SnTe ($a_{SnTe}=$ 6.336) reciprocal lattice points, as indicated by the dashed and solid lines, respectively. Systematic evaluation of the lattice parameters as a function of composition shows that it precisely follows Vegard's law [186]. In particular, for all samples the Sn content derived by X-ray diffraction perfectly agrees with the nominal growth values. Moreover, no traces of any secondary phases were detected.
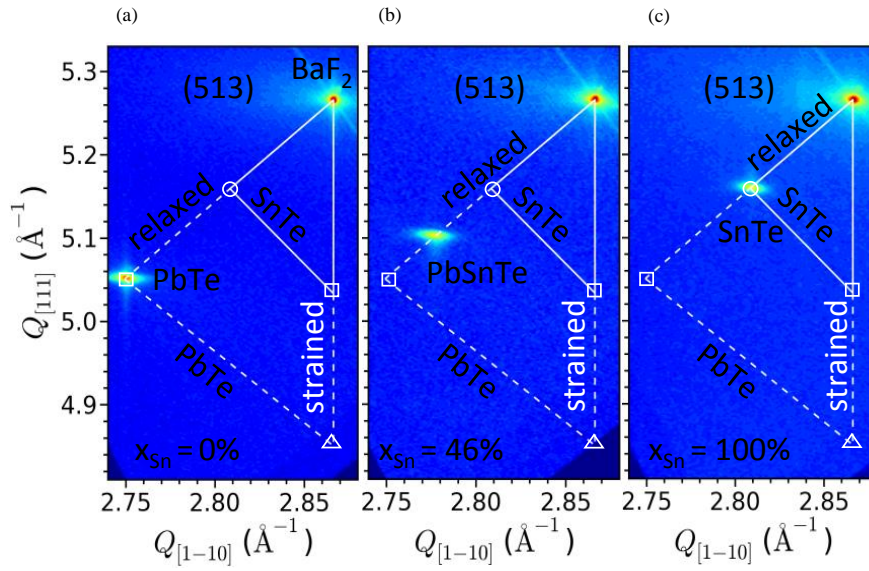
Figure B.1: *X-ray diffraction reciprocal space maps around the (513) Bragg reflection for three epilayers with $x_{Sn} = 0$, 0.46, and 1. As indicated, the layer peaks lie exactly on the line connecting the peak positions of bulk PbTe ($\Diamond$) and SnTe ($\circ$), evidencing that all films are fully relaxed without residual lattice distortion. The expected peak positions of fully strained epilayers are indicated by (Δ,$\Box$)*

List of Publication

Refereed Papers

1. Rienks, E. D. L.; Wimmer, S.; Sánchez-Barriga, J.; Caha, O.; Mandal, P. S.; Ruzicka, J.; Ney, A.; Steiner, H.; Volobuev, V. V. ; Groiss, H.; Albu, M.; Kothleitner, G.; Michalicka, J.; Khan, S. A. ; Minár, J.; Ebert, H.; Bauer, G.; Freyse, F.; Varykhalov, A.; Rader, O. ; Springholz G.: Large magnetic gap at the Dirac point in $Bi_2Te_3/MnBi_2Te_4$ heterostructures. *Nature*, volume **576** (2019)DOI: 10.1038/s41586-019-1826-7.

2. Mandal, P.S.; Springholz, G.; Volobuev, V.; Bauer, G.; Golias, E.; Varykhalov, A.; Rader, O.; Sánchez-Barriga, J.: Topological quantum phase transition from mirror to time reversal symmetry protected topological insulator. *Nature Communications*, volume **8**, Article number: 968 (2017).

3. Assaf, B.A.; Phuphachong, T.; Kampert, E.; Volobuev, V.V.; Mandal, P. S.; Sánchez-Barriga, J.; Rader, O.; Bauer, G.; Springholz, G.; de Vaulchier, L.A.; Guldner Y.: Negative longitudinal magnetoresistance from anomalous N=0 Landau level in topological materials. *Physical Review Letters* **119**(10). DOI: 10.1103/PhysRevLett.119.106602.

4. Volobuev, V. V.; Mandal, P. S.; Galicka, M.; Caha, O.; Sánchez-Barriga, J.; Di Sante, D.; Varykhalov, A.; Khiar, A.; Picozzi, S.; Bauer, G.; Kacman, P.; Buczko, R.; Rader, O.; Springholz, G.: Giant Rashba Splitting in $Pb_{1-x}Sn_xTe(111)$ Topological Crystalline Insulator Films Controlled by Bi Doping in the Bulk. Adv. Mater.(2016), doi:10.1002/adma.201604185.

5. Wu, H.-C.; Chaika, A.N.; Huang, T.-W.; Syrlybekov, A.; Abid, M.; Aristov, V.Yu.; Molodtsova, O.V.; Babenkov, S.V.; Marchenko, D.; Sánchez-Barriga, J.; Mandal, P.S.; Varykhalov, A.Yu.; Niu, Y.; Murphy, B.E.; Krasnikov, S..A.; Luebben, O.; Wang, J.J.; Liu, H.; Yang, L.; Zhang, H.; Abid, M.; Janabi, Y.T.; Molotkov, S.N.; Chang, C.-R.; Shvets, I.: Transport Gap Opening and High On-Off Current Ratio in Trilayer Graphene with Self-Aligned Nanodomain Boundaries. ACS Nano 9 (2015), p. 8967-8975

6. Varykhalov, A.; Sanchez-Barriga, J.; Marchenko, D.; Hlawenka, P.; Mandal, P.S.;

Rader, O.: Tunable Fermi level and hedgehog spin texture in gapped graphene. Nature Communications 6 (2015), p. 7610/1-6

7. Bendt, G.; Zastrow, S.; Nielsch, K.; Mandal, P.S.; Sńchez-Barriga, J.; Rader, O.; Schulz, S.: Deposition of topological insulator Sb2Te3 films by an MOCVD process. Journal of Materials Chemistry A (2014), p. 8215-8222

8. Sharma, S.K.; Dutta, S.; Som, S.; Mandal, P. S.: $CaMoO_4$:Dy^{3+},K^+ near White Light Emitting Phosphor: Structural, Optical and Dielectric Properties. Journal of Materials Science and Technology 29 (2013), DOI:10.1016/j.jmst.2013.03.014, p. 633

9. Biswas, D. N.; Mandal, P. S.; Varier, S. R.; Sahadev, N.; Maiti, K. : Evidence of Unusual Spin Polarization of the Surface States of W(110) Surface. AIP conference proceedings 02/2013; 1512(1):816-817., DOI:10.1063/1.4791288

10. Varier, S. R.; Mandal, P. S.; Sahadev, Biswas, D. N. N.; Maiti, K.: Study Of The Surface Electronic Structure Of Si(111) Surface Using Spin And Angle Resolved Photoemission Spectroscopy. AIP conference proceedings 02/2013; 1512(1):818-819., DOI:10.1063/1.4791289

Conference Posters

1. Mandal, P.S.; Springholz, G.; Volobuev, V.; Bauer, G.; Varykhalov, A.; Rader, O.; Sánchez-Barriga, J.: Temperature dependent phase transition of the crystalline topological insulator, New Trends in Topological Insulators (NTTI), Berlin, Germany (2014)

2. Mandal, P.S.; Springholz, G.; Volobuev, V.; Bauer, G.; Varykhalov, A.; Rader, O.; Sánchez-Barriga, J.:Observation of Gapped Dirac cone despite protection by crystal and time-reversal symmetries on Pb-Sn-Se (111) epitaxial films. New Trends in Topological Insulators (NTTI), San Sebastian, Spain (2015)

3. Mandal, P.S.; Springholz, G.; Volobuev, V.; Bauer, G.; Golias, E.; Varykhalov, A.; Rader, O.; Sánchez-Barriga, J.: Quantum Phase Transition from Mirror to Time Reversal Symmetry Protected Topological Insulator. SPP1666 Kickoff meeting, Frankfurt (2016)

Conference Talks

1. Mandal, P.S.; Springholz, G.; Volobuev, V.; Bauer, G.; Varykhalov, A.; Rader, O.; Sánchez-Barriga, J.: Temperature driven topological phase transition of Pb-Sn-Se(111) surface. DPG Frühjahrstagung, Dresden, Germany (2014)

2. Mandal, P.S.; Springholz, G.; Volobuev, V.; Bauer, G.; Varykhalov, A.; Rader, O.; Sánchez-Barriga, J.: Temperature driven topological phase transition of Pb-Sn-Se(111)

surface. Summer School on Ultraviolet and X-ray Spectroscopies of Correlated-Electron Systems, (SUCCESS), Les Houches, France (2014)

3. Mandal, P.S.: Epitaxial Lead Tin Chalcogenide Topological Crystalline Insulators, Helmholtz Virtual Institute New States of Matter and their Excitation (HVINSM), Annual Student Meeting, Munich (2015)

4. Mandal, P.S.; Springholz, G.; Volobuev, V.; Bauer, G.; Golias, E.; Varykhalov, A.; Rader, O.; Sánchez-Barriga, J.: Observation of gapped surface states in the topological regime of the quantum-phase transition in Bi-doped Pb-Sn-Se (111) epitaxial films. DPG Frühjahrstagung, Regensburg, Germany (2016)

Acknowledgements

"Let us be grateful to the people who makes us happy; they are the charming gardeners who make our souls blossom"

— Marcel Proust; French novelist

I think it is not possible to go through a Ph.D. without involving others in the journey. Although it is hard to find the right words to show my gratitude, my only hope is that I was able to show my appreciation whenever we have met on this journey.

First and foremost, I would like to acknowledge my utmost gratitude to my thesis supervisor *Dr. Oliver Rader* for his enormous support and encouragement throughout the journey. Without his proper guidance, this thesis would remain a distant dream for me. I learned a lot not only about physics but also the qualities of being a good scientist. I would also like to acknowledge *Dr. Emil Rienks* for his tremendous support during the one-cube beamtime and also helping me with those fancy IGOR routines for data analysis. I also would like to thank *Dr. Jaime Sánchez-Barriga* for his enormous enthusiasm for science and continuous encouragement during extensive beamtime. A significant part of the data used in this thesis has been collected and analyzed with his support. I am also very much thankful to *Dr. Andrei Varykhalov* for his utmost patience while explaining the technical details of the ARPES measurements. I am also thankful to *Dr. Peter Hlawenka* for his help during those initial days when I first moved to Berlin for my Ph.D. It is not easy to get settled in a foreign country without speaking the local language; however, your help made it a lot easier for me in that respect. I would also like to thank *Dr. Evangelos Golias* for all the scientific and non-scientific discussions we had during lunchtime.

I am also very grateful for all the scientific collaborators who have contributed enormously to this thesis. Especially *Prof. Gunther Springholz* for providing with the excellent quality thin film samples and sharing your knowledge about MBE techniques. Your utmost sincerity with good quality samples and your enthusiasm to participate during the beamtime have always encouraged me throughout the journey. I would also like to acknowledge *Prof. Günther Bauer* for all the fruitful scientific discussion. I am also thankful to *Dr. Valentyn Volobuev* for sharing his expertise on sample growth. We had a good time at NTTI in San Sebastian. I would also like to thank *Dr. Ondrej Caha* for sharing his knowledge in X-ray diffraction

Bibliography

[1] *Nobel Prize.org- https://www.nobelprize.org/prizes/physics/2016/summary/* (2016)

[2] F. Bloch, *Zeitschrift für Physik* **52**, 555 (1929)

[3] T. Ando and Y. Uemura, *Journal of the Physical Society of Japan* **36**, 959 (1974)

[4] J. Weis and K. von Klitzing, *Philosophical Transactions of the Royal Society A: Mathematical, Physical and Engineering Sciences* **369**, 3954 (2011)

[5] K. v. Klitzing, G. Dorda, and M. Pepper, *Phys. Rev. Lett.* **45**, 494 (1980)

[6] B. I. Halperin, *Phys. Rev. B* **25**, 2185 (1982)

[7] C. Kane and J. Moore, *Physics World* **24**, 32 (2011)

[8] D. J. Thouless, M. Kohmoto, M. P. Nightingale, and M. den Nijs, *Phys. Rev. Lett.* **49**, 405 (1982)

[9] R. B. Laughlin, *Phys. Rev. B* **23**, 5632 (1981)

[10] M. V. Berry, *Proceedings of the Royal Society of London. A. Mathematical and Physical Sciences* **392**, 45 (1984)

[11] F. D. M. Haldane, *Phys. Rev. Lett.* **61**, 2015 (1988)

[12] W. P. Su, J. R. Schrieffer, and A. J. Heeger, *Phys. Rev. B* **22**, 2099 (1980)

[13] A. H. Castro Neto, F. Guinea, N. M. R. Peres, K. S. Novoselov, and A. K. Geim, *Rev. Mod. Phys.* **81**, 109 (2009)

[14] T. Das, *Phys. Rev. B* **88**, 035444 (2013)

[15] C. L. Kane and E. J. Mele, *Physical Review Letters* **95**, 1 (2005)

[16] C. L. Kane and E. J. Mele, *Phys. Rev. Lett.* **95**, 146802 (2005)

[17] B. A. Bernevig, T. L. Hughes, and S.-C. Zhang, *Science* **314**, 1757 (2006)

[18] M. König, S. Wiedmann, C. Brüne, A. Roth, H. Buhmann, L. W. Molenkamp, X.-L. Qi, and S.-C. Zhang, *Science* **318**, 766 (2007)

[19] L. Fu and C. L. Kane, *Phys. Rev. B* **76**, 045302 (2007)

[20] L. Fu and C. L. Kane, *Phys. Rev. B* **74**, 195312 (2006)

[21] J. E. Moore and L. Balents, *Phys. Rev. B* **75**, 121306 (2007)

[22] L. Fu, C. L. Kane, and E. J. Mele, *Phys. Rev. Lett.* **98**, 106803 (2007)

[23] R. Roy, *Phys. Rev. B* **79**, 195322 (2009)

[24] D. Hsieh, Y. Xia, D. Qian, L. Wray, J. H. Dil, F. Meier, J. Osterwalder, L. Patthey, J. G. Checkelsky, N. P. Ong, A. V. Fedorov, H. Lin, A. Bansil, D. Grauer, Y. S. Hor, R. J. Cava, and M. Z. Hasan, *Nature* **460**, 1101 (2009)

[25] Y. Xia, D. Qian, D. Hsieh, L. Wray, A. Pal, H. Lin, A. Bansil, D. Grauer, Y. S. Hor, R. J. Cava, and M. Z. Hasan, *Nature Physics* **5**, 398 (2009)

[26] Y. S. Hor, A. Richardella, P. Roushan, Y. Xia, J. G. Checkelsky, A. Yazdani, M. Z. Hasan, N. P. Ong, and R. J. Cava, *Phys. Rev. B* **79**, 195208 (2009)

[27] Y. L. Chen, J. G. Analytis, J.-H. Chu, Z. K. Liu, S.-K. Mo, X. L. Qi, H. J. Zhang, D. H. Lu, X. Dai, Z. Fang, S. C. Zhang, I. R. Fisher, Z. Hussain, and Z.-X. Shen, *Science* **325**, 178 (2009)

[28] D. Hsieh, Y. Xia, D. Qian, L. Wray, F. Meier, J. H. Dil, J. Osterwalder, L. Patthey, A. V. Fedorov, H. Lin, A. Bansil, D. Grauer, Y. S. Hor, R. J. Cava, and M. Z. Hasan, *Phys. Rev. Lett.* **103**, 146401 (2009)

[29] D. Hsieh, Y. Xia, L. Wray, D. Qian, A. Pal, J. H. Dil, J. Osterwalder, F. Meier, G. Bihlmayer, C. L. Kane, Y. S. Hor, R. J. Cava, and M. Z. Hasan, *Science* **323**, 919 (2009)

[30] S. Souma, K. Kosaka, T. Sato, M. Komatsu, A. Takayama, T. Takahashi, M. Kriener, K. Segawa, and Y. Ando, *Phys. Rev. Lett.* **106**, 216803 (2011)

[31] Z.-H. Pan, E. Vescovo, A. V. Fedorov, D. Gardner, Y. S. Lee, S. Chu, G. D. Gu, and T. Valla, *Phys. Rev. Lett.* **106**, 257004 (2011)

[32] C. Jozwiak, Y. L. Chen, A. V. Fedorov, J. G. Analytis, C. R. Rotundu, A. K. Schmid, J. D. Denlinger, Y.-D. Chuang, D.-H. Lee, I. R. Fisher, R. J. Birgeneau, Z.-X. Shen, Z. Hussain, and A. Lanzara, *Phys. Rev. B* **84**, 165113 (2011)

[33] K. Miyamoto, A. Kimura, T. Okuda, H. Miyahara, K. Kuroda, H. Namatame, M. Taniguchi, S. V. Eremeev, T. V. Menshchikova, E. V. Chulkov, K. A. Kokh, and O. E. Tereshchenko, *Phys. Rev. Lett.* **109**, 166802 (2012)

[34] D. Hsieh, D. Qian, L. Wray, Y. Xia, Y. S. Hor, R. J. Cava, and M. Z. Hasan, *Nature* **452**, 970 (2008)

[35] X.-L. Qi, T. L. Hughes, S. Raghu, and S.-C. Zhang, *Phys. Rev. Lett.* **102**, 187001 (2009)

[36] X.-L. Qi and S.-C. Zhang, *Rev. Mod. Phys.* **83**, 1057 (2011)

[37] L. Fu, *Phys. Rev. Lett.* **106**, 106802 (2011)

[38] A. M. Essin, J. E. Moore, and D. Vanderbilt, *Phys. Rev. Lett.* **102**, 146805 (2009)

[39] X. Wan, A. Vishwanath, and S. Y. Savrasov, *Phys. Rev. Lett.* **108**, 146601 (2012)

[40] C. W. Groth, M. Wimmer, A. R. Akhmerov, J. Tworzydło, and C. W. J. Beenakker, *Phys. Rev. Lett.* **103**, 196805 (2009)

[41] J. Li, R.-L. Chu, J. K. Jain, and S.-Q. Shen, *Phys. Rev. Lett.* **102**, 136806 (2009)

[42] M. Dzero, K. Sun, V. Galitski, and P. Coleman, *Phys. Rev. Lett.* **104**, 106408 (2010)

[43] S. Raghu, X.-L. Qi, C. Honerkamp, and S.-C. Zhang, *Phys. Rev. Lett.* **100**, 156401 (2008)

[44] Y. Ando and L. Fu, *Annual Review of Condensed Matter Physics* **6**, 150126111446001 (2014)

[45] T. H. Hsieh, H. Lin, J. Liu, W. Duan, A. Bansil, and L. Fu, *Nature Communications* **3**, 982 (2012)

[46] T. H. Hsieh, H. Lin, J. Liu, W. Duan, A. Bansi, and L. Fu, *Nature Communications* **3**, 982 (2012)

[47] E. H. Hall, *The London, Edinburgh, and Dublin Philosophical Magazine and Journal of Science* **12**, 157 (1881)

[48] C.-X. Liu, S.-C. Zhang, and X.-L. Qi, *Annual Review of Condensed Matter Physics* **7**, 301 (2016)

[49] C.-X. Liu, X.-L. Qi, X. Dai, Z. Fang, and S.-C. Zhang, *Phys. Rev. Lett.* **101**, 146802 (2008)

[50] X. Kou, Y. Fan, M. Lang, P. Upadhyaya, and K. L. Wang, *Solid State Communications* **215-216**, 34 (2015)

[51] C.-Z. Chang and M. Li, *Journal of Physics: Condensed Matter* **28**, 123002 (2016)

[52] Y. Tokura, K. Yasuda, and A. Tsukazaki, *Nature Reviews Physics* **1**, 126 (2019)

[53] C.-Z. Chang, J. Zhang, X. Feng, J. Shen, Z. Zhang, M. Guo, K. Li, Y. Ou, P. Wei, L.-L. Wang, Z.-Q. Ji, Y. Feng, S. Ji, X. Chen, J. Jia, X. Dai, Z. Fang, S.-C. Zhang, K. He, Y. Wang, L. Lu, X.-C. Ma, and Q.-K. Xue, *Science* **340**, 167 (2013)

[54] R. Yu, W. Zhang, H.-J. Zhang, S.-C. Zhang, X. Dai, and Z. Fang, *Science* **329**, 61 (2010)

[55] J. Wang, B. Lian, and S.-C. Zhang, *Physica Scripta* **T164**, 014003 (2015)

[56] S. LaShell, B. A. McDougall, and E. Jensen, *Phys. Rev. Lett.* **77**, 3419 (1996)

[57] E. Rotenberg, J. W. Chung, and S. D. Kevan, *Phys. Rev. Lett.* **82**, 4066 (1999)

[58] M. Hochstrasser, J. G. Tobin, E. Rotenberg, and S. D. Kevan, *Phys. Rev. Lett.* **89**, 216802 (2002)

[59] T. Hirahara, K. Miyamoto, I. Matsuda, T. Kadono, A. Kimura, T. Nagao, G. Bihlmayer, E. V. Chulkov, S. Qiao, K. Shimada, H. Namatame, M. Taniguchi, and S. Hasegawa, *Phys. Rev. B* **76**, 153305 (2007)

[60] O. Krupin, G. Bihlmayer, K. Starke, S. Gorovikov, J. E. Prieto, K. Döbrich, S. Blügel, and G. Kaindl, *Phys. Rev. B* **71**, 201403 (2005)

[61] F. Reinert, G. Nicolay, S. Schmidt, D. Ehm, and S. Hüfner, *Phys. Rev. B* **63**, 115415 (2001)

[62] H. Lin, T. Das, Y. Okada, M. C. Boyer, W. D. Wise, M. Tomasik, B. Zhen, E. W. Hudson, W. Zhou, V. Madhavan, C.-Y. Ren, H. Ikuta, and A. Bansil, *Nano Letters* **13**, 1915 (2013), pMID: 23614400

[63] H. Lin, T. Das, L. A. Wray, S.-Y. Xu, M. Z. Hasan, and A. Bansil, *New Journal of Physics* **13**, 095005 (2011)

[64] A. Bansil, H. Lin, and T. Das, *Rev. Mod. Phys.* **88**, 021004 (2016)

[65] M. Z. Hasan and C. L. Kane, *Rev. Mod. Phys.* **82**, 3045 (2010)

[66] H. Zhang and S.-C. Zhang, *physica status solidi (RRL)- Rapid Research Letters* **7**, 72 (2013)

[67] X.-L. Qi, T. L. Hughes, and S.-C. Zhang, *Phys. Rev. B* **78**, 195424 (2008)

[68] Y. Ando, *Journal of the Physical Society of Japan* **82**, 102001 (2013)

[69] J. Maciejko, T. L. Hughes, and S.-C. Zhang, *Annual Review of Condensed Matter Physics* **2**, 31 (2011)

[70] N. Nagaosa, J. Sinova, S. Onoda, A. H. MacDonald, and N. P. Ong, *Rev. Mod. Phys.* **82**, 1539 (2010)

[71] B. A. Bernevig and T. L. Hughes, *Topological Insulators and Topological Superconductors*, chap. 3 (Princeton University Press, Princeton, 2013)

[72] S. Q. Shen, *Topological Insulators, Springer Series in Solid-State Sciences*, chap. - (Springer Berlin, 2017)

[73] H. Hertz, *Annalen der Physik* **267**, 983 (1887)

[74] A. Einstein, *Annalen der Physik* **322**, 132 (1905)

[75] A. Einstein, *Annalen der Physik* **325**, 199 (1906)

[76] K. Siegbahn, *ESCA applied to free molecules* (North-Holland Pub. Co., 1970)

[77] S. Hüfner, *Photoelectron Spectroscopy: Principles and Applications*, Advanced Texts in Physics (Springer, 2003)

[78] M. Cardona and L. Ley, *Photoemission in solids: General principles*, Topics in applied physics (Springer-Verlag, 1978)

[79] *Reports on Progress in Physics* **60**, 1217 (1997)

[80] W. Kuch and C. M. Schneider, *Reports on Progress in Physics* **64**, 147 (2001)

[81] M. P. Seah and W. A. Dench, *Surface and Interface Analysis* **1**, 2 (1979)

[82] M. P. Seah and W. A. Dench, *Surf. Interface Anal.* **1**, 2 (1979)

[83] E. W. Plummer, *Photoemission and field emission spectroscopy*, 143–223 (Springer Berlin Heidelberg, Berlin, Heidelberg, 1975)

[84] A. Damascelli, Z. Hussain, and Z.-X. Shen, *Rev. Mod. Phys.* **75**, 473 (2003)

[85] J. W. Gadzuk and M. **S**unjić, *Phys. Rev. B* **12**, 524 (1975)

[86] K. Shimada, *in High-resolution Photoemission Spectroscopy of Solids Using Synchrotron Radiation*, 85–112 (Springer Berlin Heidelberg, Berlin, Heidelberg, 2007)

[87] W. Eberhardt and F. J. Himpsel, *Phys. Rev. B* **21**, 5572 (1980)

[88] J. Hermanson, *Solid State Communications* **22**, 9 (1977)

[89] W. Shockley, *Phys. Rev.* **56**, 317 (1939)

[90] I. E. Tamm, *Phys. Z. Soviet Union* **1**, 733 (1932)

[91] N. W. Ashcroft and N. D. Mermin, *Solid State Physics* (1976)

[92] A. Varykhalov, *Journal of large-scale research facilities* **4** (2018)

[93] *Helmholtz-Zentrum Berlin: https://www.helmholtz-berlin.de/forschung/oe/em/m-dynamik/instrumente.html* (2019)

[94] D. Attwood, *Soft X-Rays and Extreme Ultraviolet Radiation: Principles and Applications* (Cambridge University Press, 2007)

[95] B. Buras, R. Fourme, and M. Koch, *in Handbook on Synchrotron Radiation (2nd ed.)* (1983)

[96] H. Baumgärtel, *Berichte der Bunsengesellschaft für physikalische Chemie* **92**, 657A (1988)

[97] L. Fu and C. L. Kane, *Phys. Rev. B* **76**, 45302 (2007)

[98] L. Fu, C. L. Kane, and E. J. Mele, *Phys. Rev. Lett.* **98**, 106803 (2007)

[99] M. Brahlek, N. Bansal, N. Koirala, S.-Y. Xu, M. Neupane, C. Liu, M. Z. Hasan, and S. Oh, *Phys. Rev. Lett.* **109**, 186403 (2012)

[100] L. Wu, M. Brahlek, R. Valdés Aguilar, A. V. Stier, C. M. Morris, Y. Lubashevsky, L. S. Bilbro, N. Bansal, S. Oh, and N. P. Armitage, *Nature Physics* **9**, 410 (2013)

[101] S.-Y. Xu, Y. Xia, L. A. Wray, S. Jia, F. Meier, J. H. Dil, J. Osterwalder, B. Slomski, A. Bansil, H. Lin, R. J. Cava, and M. Z. Hasan, *Science* **332**, 560 (2011)

[102] Y. Tanaka, Z. Ren, T. Sato, K. Nakayama, S. Souma, T. Takahashi, K. Segawa, and Y. Ando, *Nat Phys* **8**, 800 (2012)

[103] S.-Y. Xu, C. Liu, N. Alidoust, M. Neupane, D. Qian, I. Belopolski, J. D. Denlinger, Y. J. Wang, H. Lin, L. A. Wray, G. Landolt, B. Slomski, J. H. Dil, A. Marcinkova, E. Morosan, Q. Gibson, R. Sankar, F. C. Chou, R. J. Cava, A. Bansil, and M. Z. Hasan, *Nature Communications* **3**, 1192 (2012)

[104] P. Dziawa, B. J. Kowalski, K. Dybko, R. Buczko, A. Szczerbakow, M. Szot, E. Łusakowska, T. Balasubramanian, B. M. Wojek, M. H. Berntsen, O. Tjernberg, and T. Story, *Nat Mater* **11**, 1023 (2012)

[105] S. Safaei, P. Kacman, and R. Buczko, *Phys. Rev. B* **88**, 045305 (2013)

[106] M. Wuttig and N. Yamada, *Nature Materials* **6**, 824 (2007)

[107] F. J. Schmitte, *Physics of Non-Tetrahedrally Bonded Binary Compounds II (ed. Madelung, O.) Landolt-Börnstein, New Series III/17F* (Springer, Berlin, 1983)

[108] T. Chattopadhyay, J. X. Boucherle, and H. G. vonSchnering, *Journal of Physics C: Solid State Physics* **20**, 1431 (1987)

[109] D. Di Sante, P. Barone, R. Bertacco, and S. Picozzi, *Advanced Materials* **25**, 509 (2013)

[110] Y. Okada, M. Serbyn, H. Lin, D. Walkup, W. Zhou, C. Dhital, M. Neupane, S. Xu, Y. J. Wang, R. Sankar, F. Chou, A. Bansil, M. Z. Hasan, S. D. Wilson, L. Fu, and V. Madhavan, *Science (New York, N.Y.)* **341**, 1496 (2013)

[111] I. Zeljkovic, Y. Okada, M. Serbyn, R. Sankar, D. Walkup, W. Zhou, J. Liu, G. Chang, Y. J. Wang, M. Z. Hasan, F. Chou, H. Lin, A. Bansil, L. Fu, and V. Madhavan, *Nat Mater* **14**, 318 (2015)

[112] B. M. Wojek, M. H. Berntsen, V. Jonsson, A. Szczerbakow, P. Dziawa, B. J. Kowalski, T. Story, and O. Tjernberg, *Nature Communications* **6**, 8463 (2015)

[113] C. Niu, P. M. Buhl, G. Bihlmayer, D. Wortmann, S. Blügel, and Y. Mokrousov, *Nano Letters* **15**, 6071 (2015)

[114] E. Plekhanov, P. Barone, D. Di Sante, and S. Picozzi, *Phys. Rev. B* **90**, 161108 (2014)

[115] S. Safaei, M. Galicka, P. Kacman, and R. Buczko, *New Journal of Physics* **17**, 063041 (2015)

[116] P. S. Mandal, G. Springholz, V. V. Volobuev, O. Caha, A. Varykhalov, E. Golias, G. Bauer, O. Rader, and J. Sánchez-Barriga, *Nature Communications* **8**, 968 (2017)

[117] G. Springholz, A. Y. Ueta, N. Frank, and G. Bauer, *Applied Physics Letters* **69**, 2822 (1996)

[118] M. Neupane, S.-Y. Xu, R. Sankar, Q. Gibson, Y. J. Wang, I. Belopolski, N. Alidoust, G. Bian, P. P. Shibayev, D. S. Sanchez, Y. Ohtsubo, A. Taleb-Ibrahimi, S. Basak, W.-F. Tsai, H. Lin, T. Durakiewicz, R. J. Cava, A. Bansil, F. C. Chou, and M. Z. Hasan, *Phys. Rev. B* **92**, 075131 (2015)

[119] C. M. Polley, P. Dziawa, A. Reszka, A. Szczerbakow, R. Minikayev, J. Z. Domagala, S. Safaei, P. Kacman, R. Buczko, J. Adell, M. H. Berntsen, B. M. Wojek, O. Tjernberg, B. J. Kowalski, T. Story, and T. Balasubramanian, *Phys. Rev. B* **89**, 075317 (2014)

[120] I. Gierz, J. Henk, H. Höchst, C. R. Ast, and K. Kern, *Phys. Rev. B* **83**, 121408 (2011)

[121] A. J. Strauss, *Physical Review* **157**, 1 (1967)

[122] A. Ueta, G. Springholz, F. Schinagl, G. Marschner, and G. Bauer, *Thin Solid Films* **306**, 320 (1997)

[123] V. A. Zykov, T. A. Gavrikova, V. I. Il'in, S. A. Nemov, and P. V. Savintsev, *Semiconductors* **35**, 1254 (2001)

[124] D. A. Shirley, *Phys. Rev. B* **5**, 4709 (1972)

[125] B. M. Wojek, R. Buczko, S. Safaei, P. Dziawa, B. J. Kowalski, M. H. Berntsen, T. Balasubramanian, M. Leandersson, A. Szczerbakow, P. Kacman, T. Story, and O. Tjernberg, *Phys. Rev. B* **87**, 115106 (2013)

[126] S.-Y. Xu, M. Neupane, I. Belopolski, C. Liu, N. Alidoust, G. Bian, S. Jia, G. Landolt, B. Slomski, J. H. Dil, P. P. Shibayev, S. Basak, T.-R. Chang, H.-T. Jeng, R. J. Cava, H. Lin, A. Bansil, and M. Z. Hasan, *Nature Communications* **6**, 6870 (2015)

[127] J. Yeh and I. Lindau, *Atomic Data and Nuclear Data Tables* **32**, 1 (1985)

[128] P. B. Littlewood, *Journal of Physics C: Solid State Physics* **13**, 4855 (1980)

[129] P. B. Littlewood, *Journal of Physics C: Solid State Physics* **13**, 4875 (1980)

[130] P. B. Littlewood, *Critical Reviews in Solid State and Materials Sciences* **11**, 229 (1983)

[131] G. Nimtz and B. Schlicht, *Narrow-gap lead salts*, 1–117 (Springer Berlin Heidelberg, Berlin, Heidelberg, 1983)

[132] W. Jantsch, A. Bussmann-Holder, H. Bilz, and P. Vogel, *Dynamical properties of IV-VI compounds in Springer Tracts in Modern Physics 1-98, Vol. 99*, chap. - (Springer, Berlin, 1983)

[133] E. Bangert, G. Bauer, E. J. Fantner, and H. Pascher, *Phys. Rev. B* **31**, 7958 (1985)

[134] A. I. Lebedev and I. A. Sluchinskaya, *Ferroelectrics* **169**, 293 (1995)

[135] K. Chang, J. Liu, H. Lin, N. Wang, K. Zhao, A. Zhang, F. Jin, Y. Zhong, X. Hu, W. Duan, Q. Zhang, L. Fu, Q.-K. Xue, X. Chen, and S.-H. Ji, *Science* **353**, 274 (2016)

[136] P. B. Littlewood, *Journal of Physics C: Solid State Physics* **13**, 4875 (1980)

[137] P. B. Littlewood, *Journal of Physics C: Solid State Physics* **13**, 4855 (1980)

[138] S. Sugai, K. Murase, S. Katayama, S. Takaoka, S. Nishi, and H. Kawamura, *Solid State Communications* **24**, 407 (1977)

[139] B. J. Kooi and B. Noheda, *Science* **353**, 221 (2016)

[140] D. P. Mathur, *Optical Engineering* **14**, 351 (1975)

[141] G. A. Antcliffe and J. S. Wrobel, *Appl. Opt.* **11**, 1548 (1972)

[142] P. W. Zhu, L. X. Chen, X. Jia, H. A. Ma, G. Z. Ren, W. L. Guo, W. Zhang, and G. T. Zou, *Journal of Physics: Condensed Matter* **14**, 11185 (2002)

[143] J. O. Dimmock and G. B. Wright, *Phys. Rev.* **135**, A821 (1964)

[144] J. O. Dimmock, I. Melngailis, and A. J. Strauss, *Phys. Rev. Lett.* **16**, 1193 (1966)

[145] B. A. Volkov and O. A. Pankratov, *JETP Lett.* **42**, 178 (1985)

[146] E. Fradkin, E. Dagotto, and D. Boyanovsky, *Phys. Rev. Lett.* **57**, 2967 (1986)

[147] V. V. Volobuev, P. S. Mandal, M. Galicka, O. Caha, J. Sánchez-Barriga, D. Di Sante, A. Varykhalov, A. Khiar, S. Picozzi, G. Bauer, P. Kacman, R. Buczko, O. Rader, and G. Springholz, *Advanced Materials* **29**, 1604185 (2017)

[148] J. Liu, W. Duan, and L. Fu, *Physical Review B - Condensed Matter and Materials Physics* **88**, 1 (2013)

[149] G. E. Volovik, *The Universe in a Helium Droplet* (Oxford, UK: Oxford Univ. Press, 2003)

[150] L. Fu and C. L. Kane, *Phys. Rev. B* **76**, 045302 (2007)

[151] J. O. Dimmock, I. Melngailis, and A. J. Strauss, *Phys. Rev. Lett.* **16**, 1193 (1966)

[152] H. Preier, *Applied physics* **20**, 189 (1979)

[153] C. Yan, J. Liu, Y. Zang, J. Wang, Z. Wang, P. Wang, Z.-D. Zhang, L. Wang, X. Ma, S. Ji, K. He, L. Fu, W. Duan, Q.-K. Xue, and X. Chen, *Phys. Rev. Lett.* **112**, 186801 (2014)

[154] R. Zhong, X. He, J. A. Schneeloch, C. Zhang, T. Liu, I. Pletikosić, T. Yilmaz, B. Sinkovic, Q. Li, W. Ku, T. Valla, J. M. Tranquada, and G. Gu, *Phys. Rev. B* **91**, 195321 (2015)

[155] Y. Tanaka, T. Sato, K. Nakayama, S. Souma, T. Takahashi, Z. Ren, M. Novak, K. Segawa, and Y. Ando, *Phys. Rev. B* **87**, 155105 (2013)

[156] E. Tang and L. Fu, *Nat Phys* **10**, 964 (2014)

[157] M. Serbyn and L. Fu, *Phys. Rev. B* **90**, 035402 (2014)

[158] J. Liu, T. H. Hsieh, P. Wei, W. Duan, J. Moodera, and L. Fu, *Nat Mater* **13**, 178 (2014)

[159] B. A. Assaf, F. Katmis, P. Wei, C.-Z. Chang, B. Satpati, J. S. Moodera, and D. Heiman, *Phys. Rev. B* **91**, 195310 (2015)

[160] I. Zeljkovic, K. L. Scipioni, D. Walkup, Y. Okada, W. Zhou, R. Sankar, G. Chang, Y. J. Wang, H. Lin, A. Bansil, F. Chou, Z. Wang, and V. Madhavan, *Nature Communications* **6**, 6559 (2015)

[161] C. Niu, Y. Dai, Y. Ma, L. Yu, and B. Huang, *Materials Express* **3**, 159 (2013)

[162] X. Qian, L. Fu, and J. Li, *Nano Research* **8**, 967 (2015)

[163] B. A. Assaf, T. Phuphachong, V. V. Volobuev, A. Inhofer, G. Bauer, G. Springholz, L. A. de Vaulchier, and Y. Guldner, *Scientific Reports* **6**, 20323 (2016)

[164] G. i. Springholz, *Lead Chalcogenides: Physics and Applications*, 123–207 (Taylor and Francis, New York, 2003)

[165] P. Rappl, H. Closs, S. Ferreira, E. Abramof, C. Boschetti, P. Motisuke, A. Ueta, and I. Bandeira, *Journal of Crystal Growth* **191**, 466 (1998)

[166] D. L. Partin, C. M. Thrush, S. J. Simko, and S. W. Gaarenstroom, *Journal of Applied Physics* **66**, 6115 (1989)

[167] T. Ikeda, M. B. Toussaint, K. Bergum, S. Iwanaga, and G. Jeffrey Snyder, *Journal of Materials Science* **46**, 3846 (2011)

[168] G. Springholz and G. Bauer, *Journal of Applied Physics* **77**, 540 (1995)

[169] A. Manchon, H. C. Koo, J. Nitta, S. M. Frolov, and R. A. Duine, *Nat Mater* **14**, 871 (2015)

[170] Y. Tanaka, T. Shoman, K. Nakayama, S. Souma, T. Sato, T. Takahashi, M. Novak, K. Segawa, and Y. Ando, *Phys. Rev. B* **88**, 235126 (2013)

[171] A. Crepaldi, L. Moreschini, G. Autès, C. Tournier-Colletta, S. Moser, N. Virk, H. Berger, P. Bugnon, Y. J. Chang, K. Kern, A. Bostwick, E. Rotenberg, O. V. Yazyev, and M. Grioni, *Phys. Rev. Lett.* **109**, 096803 (2012)

[172] K. Ishizaka, M. S. Bahramy, H. Murakawa, M. Sakano, T. Shimojima, T. Sonobe, K. Koizumi, S. Shin, H. Miyahara, A. Kimura, K. Miyamoto, T. Okuda, H. Namatame, M. Taniguchi, R. Arita, N. Nagaosa, K. Kobayashi, Y. Murakami, R. Kumai, Y. Kaneko, Y. Onose, and Y. Tokura, *Nat Mater* **10**, 521 (2011)

[173] M. Sakano, M. S. Bahramy, A. Katayama, T. Shimojima, H. Murakawa, Y. Kaneko, W. Malaeb, S. Shin, K. Ono, H. Kumigashira, R. Arita, N. Nagaosa, H. Y. Hwang, Y. Tokura, and K. Ishizaka, *Phys. Rev. Lett.* **110**, 107204 (2013)

[174] Z.-H. Zhu, G. Levy, B. Ludbrook, C. N. Veenstra, J. A. Rosen, R. Comin, D. Wong, P. Dosanjh, A. Ubaldini, P. Syers, N. P. Butch, J. Paglione, I. S. Elfimov, and A. Damascelli, *Phys. Rev. Lett.* **107**, 186405 (2011)

[175] T. Valla, Z.-H. Pan, D. Gardner, Y. S. Lee, and S. Chu, *Phys. Rev. Lett.* **108**, 117601 (2012)

[176] L. A. Wray, S.-Y. Xu, Y. Xia, D. Hsieh, A. V. Fedorov, Y. S. Hor, R. J. Cava, A. Bansil, H. Lin, and M. Z. Hasan, *Nat Phys* **7**, 32 (2011)

[177] P. D. C. King, R. C. Hatch, M. Bianchi, R. Ovsyannikov, C. Lupulescu, G. Landolt, B. Slomski, J. H. Dil, D. Guan, J. L. Mi, E. D. L. Rienks, J. Fink, A. Lindblad, S. Svensson, S. Bao, G. Balakrishnan, B. B. Iversen, J. Osterwalder, W. Eberhardt, F. Baumberger, and P. Hofmann, *Phys. Rev. Lett.* **107**, 096802 (2011)

[178] H. M. Benia, C. Lin, K. Kern, and C. R. Ast, *Phys. Rev. Lett.* **107**, 177602 (2011)

[179] L. A. Wray, S.-Y. Xu, Y. Xia, Y. S. Hor, D. Qian, A. V. Fedorov, H. Lin, A. Bansil, R. J. Cava, and M. Z. Hasan, *Nat Phys* **6**, 855 (2010)

[180] J. Sánchez-Barriga, A. Varykhalov, G. Springholz, H. Steiner, R. Kirchschlager, G. Bauer, O. Caha, E. Schierle, E. Weschke, A. A. Ünal, S. Valencia, M. Dunst, J. Braun, H. Ebert, J. Minár, E. Golias, L. V. Yashina, A. Ney, V. Holý, and O. Rader, *Nature Communications* **7**, 10559 (2016)

[181] T. Arakane, T. Sato, S. Souma, K. Kosaka, K. Nakayama, M. Komatsu, T. Takahashi, Z. Ren, K. Segawa, and Y. Ando, *Nature Communications* **3**, 636 (2012)

[182] D. Hsieh, Y. Xia, D. Qian, L. Wray, J. H. Dil, F. Meier, J. Osterwalder, L. Patthey, J. G. Checkelsky, N. P. Ong, A. V. Fedorov, H. Lin, A. Bansil, D. Grauer, Y. S. Hor, R. J. Cava, and M. Z. Hasan, *Nature* **460**, 1101 (2009)

[183] S. Picozzi, *Frontiers in Physics* **2**, 10 (2014)

[184] M. Liebmann, C. Rinaldi, D. Di Sante, J. Kellner, C. Pauly, R. N. Wang, J. E. Boschker, A. Giussani, S. Bertoli, M. Cantoni, L. Baldrati, M. Asa, I. Vobornik, G. Panaccione, D. Marchenko, J. Sánchez-Barriga, O. Rader, R. Calarco, S. Picozzi, R. Bertacco, and M. Morgenstern, *Advanced Materials* **28**, 560 (2016)

[185] J. Krempaský, H. Volfová, S. Muff, N. Pilet, G. Landolt, M. Radović, M. Shi, D. Kriegner, V. Holý, J. Braun, H. Ebert, F. Bisti, V. A. Rogalev, V. N. Strocov, G. Springholz, J. Minár, and J. H. Dil, *Phys. Rev. B* **94**, 205111 (2016)

[186] P. J. McCann, J. Fuchs, Z. Feit, and C. G. Fonstad, *Journal of Applied Physics* **62**, 2994 (1987)

[187] C. R. Ast, J. Henk, A. Ernst, L. Moreschini, M. C. Falub, D. Pacilé, P. Bruno, K. Kern, and M. Grioni, *Phys. Rev. Lett.* **98**, 186807 (2007)

[188] I. Gierz, F. Meier, J. H. Dil, K. Kern, and C. R. Ast, *Phys. Rev. B* **83**, 195122 (2011)

[189] V. L. Deringer and R. Dronskowski, *ChemPhysChem* **14**, 3108 (2013)

[190] M. P. L. Sancho, J. M. L. Sancho, J. M. L. Sancho, and J. Rubio, *Journal of Physics F: Metal Physics* **15**, 851 (1985)

[191] M. Onoda and N. Nagaosa, *Phys. Rev. Lett.* **90**, 206601 (2003)

[192] R. Yu, W. Zhang, H.-J. Zhang, S.-C. Zhang, X. Dai, and Z. Fang, *Science* **329**, 61 (2010)

[193] J. G. Checkelsky, R. Yoshimi, A. Tsukazaki, K. S. Takahashi, Y. Kozuka, J. Falson, M. Kawasaki, and Y. Tokura, *Nat Phys* **10**, 731 (2014)

[194] X. Kou, S.-T. Guo, Y. Fan, L. Pan, M. Lang, Y. Jiang, Q. Shao, T. Nie, K. Murata, J. Tang, Y. Wang, L. He, T.-K. Lee, W.-L. Lee, and K. L. Wang, *Phys. Rev. Lett.* **113**, 137201 (2014)

[195] A. J. Bestwick, E. J. Fox, X. Kou, L. Pan, K. L. Wang, and D. Goldhaber-Gordon, *Phys. Rev. Lett.* **114**, 187201 (2015)

[196] A. Kandala, A. Richardella, S. Kempinger, C.-X. Liu, and N. Samarth, *Nature Communications* **6**, 7434 (2015)

[197] C.-Z. Chang, W. Zhao, D. Y. Kim, H. Zhang, B. A. Assaf, D. Heiman, S.-C. Zhang, C. Liu, M. H. W. Chan, and J. S. Moodera, *Nat Mater* **14**, 473 (2015)

[198] S. Grauer, S. Schreyeck, M. Winnerlein, K. Brunner, C. Gould, and L. W. Molenkamp, *Phys. Rev. B* **92**, 201304 (2015)

[199] S. Qi, H. Yang, J. Chen, X. Zhang, Y. Yang, and X. Xu, *Scientific Reports* **6**, 29161 (2016)

[200] J. Henk, M. Flieger, I. V. Maznichenko, I. Mertig, A. Ernst, S. V. Eremeev, and E. V. Chulkov, *Phys. Rev. Lett.* **109**, 076801 (2012)

[201] M. M. Otrokov, T. V. Menshchikova, M. G. Vergniory, I. P. Rusinov, A. Y. Vyazovskaya, Y. M. Koroteev, G. Bihlmayer, A. Ernst, P. M. Echenique, A. Arnau, and E. V. Chulkov, *2D Materials* **4**, 025082 (2017)

[202] E. D. L. Rienks, S. Wimmer, J. Sánchez-Barriga, O. Caha, P. S. Mandal, J. Ruzicka, A. Ney, H. Steiner, V. V. Volobuev, H. Groiss, M. Albu, G. Kothleitner, J. Michalicka, S. A. Khan, Minár, H. J. Ebert, G. Bauer, F. Freyse, A. Varykhalov, O. Rader, and G. Springholz, *Nature* **576** (2019)

[203] X. Zhang and S.-C. Zhang **8373**, 71 (2012)

[204] C.-X. Liu, H. Zhang, B. Yan, X.-L. Qi, T. Frauenheim, X. Dai, Z. Fang, and S.-C. Zhang, *Phys. Rev. B* **81**, 041307 (2010)

[205] Y. Zhang, K. He, C.-Z. Chang, C.-L. Song, L.-L. Wang, X. Chen, J.-F. Jia, Z. Fang, X. Dai, W.-Y. Shan, S.-Q. Shen, Q. Niu, X.-L. Qi, S.-C. Zhang, X.-C. Ma, and Q.-K. Xue, *Nature Physics* **6**, 584 (2010)

[206] Y. Sakamoto, T. Hirahara, H. Miyazaki, S.-i. Kimura, and S. Hasegawa, *Phys. Rev. B* **81**, 165432 (2010)

[207] M. Neupane, A. Richardella, J. Sánchez-Barriga, S. Xu, N. Alidoust, I. Belopolski, C. Liu, G. Bian, D. Zhang, D. Marchenko, A. Varykhalov, O. Rader, M. Leandersson, T. Balasubramanian, T.-R. Chang, H.-T. Jeng, S. Basak, H. Lin, A. Bansil, N. Samarth, and M. Z. Hasan, *Nature Communications* **5**, 3841 (2014)

[208] M. Mogi, R. Yoshimi, A. Tsukazaki, K. Yasuda, Y. Kozuka, K. S. Takahashi, M. Kawasaki, and Y. Tokura, *Applied Physics Letters* **107**, 182401 (2015)

[209] D. Zhang, A. Richardella, D. W. Rench, S.-Y. Xu, A. Kandala, T. C. Flanagan, H. Beidenkopf, A. L. Yeats, B. B. Buckley, P. V. Klimov, D. D. Awschalom, A. Yazdani, P. Schiffer, M. Z. Hasan, and N. Samarth, *Phys. Rev. B* **86**, 205127 (2012)

[210] T. Valla, Z.-H. Pan, D. Gardner, Y. S. Lee, and S. Chu, *Phys. Rev. Lett.* **108**, 117601 (2012)

[211] M. R. Scholz, J. Sánchez-Barriga, D. Marchenko, A. Varykhalov, A. Volykhov, L. V. Yashina, and O. Rader, *Phys. Rev. Lett.* **108**, 256810 (2012)

[212] M. Ye, S. V. Eremeev, K. Kuroda, E. E. Krasovskii, E. V. Chulkov, Y. Takeda, Y. Saitoh, K. Okamoto, S. Y. Zhu, K. Miyamoto, M. Arita, M. Nakatake, T. Okuda, Y. Ueda, K. Shimada, H. Namatame, M. Taniguchi, and A. Kimura, *Phys. Rev. B* **85**, 205317 (2012)

[213] J. Ruzicka, O. Caha, V. Holý, H. Steiner, V. Volobuiev, A. Ney, G. Bauer, T. Duchon, K. Veltruská, I. Khalakhan, V. Matolín, E. F. Schwier, H. Iwasawa, K. Shimada, and G. Springholz, *New Journal of Physics* **17**, 013028 (2015)

[214] P. Sessi, R. R. Biswas, T. Bathon, O. Storz, S. Wilfert, A. Barla, K. A. Kokh, O. E. Tereshchenko, K. Fauth, M. Bode, and A. V. Balatsky, *Nature Communications* **7**, 12027 (2016)

[215] I. Lee, C. K. Kim, J. Lee, S. J. L. Billinge, R. Zhong, J. A. Schneeloch, T. Liu, T. Valla, J. M. Tranquada, G. Gu, and J. C. S. Davis, *Proceedings of the National Academy of Sciences* **112**, 1316 (2015)

[216] C.-Z. Chang, P. Tang, Y.-L. Wang, X. Feng, K. Li, Z. Zhang, Y. Wang, L.-L. Wang, X. Chen, C. Liu, W. Duan, K. He, X.-C. Ma, and Q.-K. Xue, *Phys. Rev. Lett.* **112**, 056801 (2014)

[217] B. Kim, A. B. Andrews, J. L. Erskine, K. J. Kim, and B. N. Harmon, *Phys. Rev. Lett.* **68**, 1931 (1992)

[218] G. Rosenberg and M. Franz, *Phys. Rev. B* **85**, 195119 (2012)

[219] T. M. Schmidt, R. H. Miwa, and A. Fazzio, *Phys. Rev. B* **84**, 245418 (2011)

[220] L. B. Abdalla, L. Seixas, T. M. Schmidt, R. H. Miwa, and A. Fazzio, *Phys. Rev. B* **88**, 045312 (2013)

[221] A. M. Black-Schaffer and A. V. Balatsky, *Phys. Rev. B* **85**, 121103 (2012)

[222] A. M. Black-Schaffer and A. V. Balatsky, *Phys. Rev. B* **86**, 115433 (2012)

[223] J. Sánchez-Barriga, I. Aguilera, L. V. Yashina, D. Y. Tsukanova, F. Freyse, A. N. Chaika, C. Callaert, A. M. Abakumov, J. Hadermann, A. Varykhalov, E. D. L. Rienks, G. Bihlmayer, S. Blügel, and O. Rader, *Phys. Rev. B* **98**, 235110 (2018)

[224] L. Fu, *Phys. Rev. Lett.* **103**, 266801 (2009)